Supplement of Atmos. Chem. Phys., 19, 7789–7816, 2019
https://doi.org/10.5194/acp-19-7789-2019-supplement

Atmospheric Chemistry and Physics
Open Access
EGU

Supplement of

An atmospheric inversion over the city of Cape Town: sensitivity analyses

Alecia Nickless et al.

Correspondence to: Alecia Nickless (alecia.nickless@bristol.ac.uk)

1 Supplementary Material

The supplementary material presents statistics for each inversion for the purpose of comparison between inversions. The degrees of freedom of the signal are presented in Section 1.1. Section 1.2 considers the aggregated fluxes. In Section 1.2.1, fluxes are aggregated over the spatial domain and over the full study period. In Section 1.2.2, fluxes are aggregated monthly over the spatial domain. In Section 1.2.3 fluxes are aggregated weekly and presented as a time series. In Section 1.3 the observed and modelled concentrations are presented as a time series at each site. In Section 1.4 the modelled concentrations are split into the contributions from fossil fuel emissions and from biogenic emissions. Section 1.4 presents the same observed and modelled concentrations as an average diurnal cycle over the full study period. Section 1.6 presents the spatial distribution of the prior and posterior fluxes, together with the uncertainty reduction for May 2012 and for September 2012 for each inversion. Finally, in section 1.7 a toy inversion in presented to demonstrate the dependency of the posterior uncertainty on the prior uncertainty.

1.1 Degrees of Freedom of the Signal (DFS)

Degrees of freedom for the signal (DFS) were calculated for the first week of March. The DFS were calculated in order to show how the assumptions made for each sensitivity test case affected the number of independent pieces of information for a particular week. The DFS were calculated as:

$$DFS = tr((\mathbf{H}^T\mathbf{C_c}^{-1}\mathbf{H} + \mathbf{C}_{\boldsymbol{s}_0}^{-1})^{-1}\mathbf{H}^T\mathbf{C_c}^{-1}\mathbf{H})(Rodgers,\ 2000). \quad (1)$$

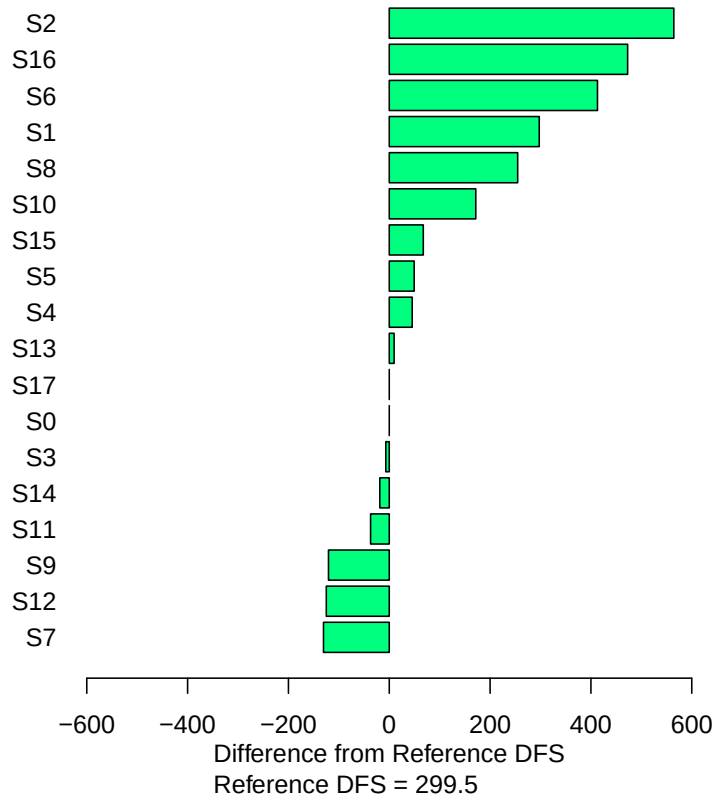

Figure S1. Difference between the reference and sensitivity test in the DFS calculated for the first week of March 2012. S0 = Reference Inversion; S1 = Carbon Assessment Inversion; S2 = ODIAC fossil fuel inversion; S3 = Correlation for NEE flux uncertainties only; S4 = Correlation for observation errors only; S5 = No correlation specified in prior covariance matrices; S6 = Correlation length for NEE flux uncertainties set at 7km; S7 = Double fossil fuel uncertainties; S8 = Half fossil fuel uncertainties; S9 = Double NEE uncertainties; S10 = Half NEE uncertainties; S11 = Domestic emission homogenised over the year; S12 = NEE fluxes averaged over the domain; S13 = Simple specification of observation error covariance matrix; S14 = Simple observation error covariance matrix with larger night-time error; S15 = Simple observation error covariance matrix with no correlation; S16 = Inversion solving for mean weekly fluxes over the month; S17 = Separate inversions for each week.

1.2 Aggregated Fluxes

1.2.1 Aggregated Fluxes over Study Period

Table S1. Prior and posterior total flux estimates of each inversion over the thirteen four-week periods for which observation data were available from March 2012 to June 2013, with uncertainties and the reduction in uncertainty with respect to the prior uncertainty. Total fluxes are expressed as $\mathrm{kt\ CO_2}$. The mean χ^2 statistic is provided over the thirteen inversion periods. NEE = Net Ecosystem Exchange, FF = Fossil Fuel

	S0	S1	S2	S3	S4	S5
Prior Flux (sd)	-1336 (254)	5181 (32)	7635 (256)	-1336 (254)	-1336 (63)	-1336 (63)
Posterior Flux (sd)	-317 (189)	4045 (28)	5787 (195)	-310 (189)	-1281 (59)	-1287 (59)
Uncertainty Reduction	25.6%	11.9%	23.6%	25.6%	7.5%	7.5%
Mean χ^2 Statistic	1.48 (0.55)	4.13 (1.24)	1.25 (0.49)	1.49 (0.54)	2.10 (0.78)	2.12 (0.79)
	S6	S7	S8	S9	S10	S11
Prior Flux (sd)	-1336 (254)	-1336 (255)	-1336 (254)	-1336 (508)	-1336 (128)	-1916 (254)
Posterior Flux (sd)	-497 (188)	-151 (190)	-423 (189)	-316 (365)	-337 (100)	-624 (189)
Uncertainty Reduction	26.0%	25.4%	25.7%	28.2%	21.9%	25.6%
Mean χ^2 Statistic	7.36 (6.23)	1.21 (0.50)	1.86 (0.63)	1.03 (0.47)	2.22 (0.69)	1.41 (0.49)
	S12	S13	S14	S15	S16	S17
Prior Flux (sd)	-1328 (126)	-1336 (254)	-1336 (254)	-1336 (254)	-1336 (126)	-1220 (251)
Posterior Flux (sd)	-1707 (106)	-325 (188)	-579 (192)	-338 (188)	662 (66)	-687 (186)
Uncertainty Reduction	15.8%	26.1%	24.4%	26.1%	47.2%	25.8%
Mean χ^2 Statistic	1.17 (0.47)	2.17 (1.04)	1.88 (0.92)	2.25 (1.13)	1.43 (0.55)	1.54 (0.56)

Prior and Posterior Flux refer to the total flux from the domain over the thirteen four-week periods. The sd of the fluxes refers to the uncertainty in the total flux estimate. The sd of the χ^2 statistic refers to the standard deviation between the χ^2 statistics of the thirteen four-week period χ^2 Statistics. S0 = Reference Inversion; S1 = Carbon Assessment Inversion; S2 = ODIAC fossil fuel inversion; S3 = Correlation for NEE flux uncertainties only; S4 = Correlation for observation errors only; S5 = No correlation specified in prior covariance matrices; S6 = Correlation length for NEE flux uncertainties set at $7\mathrm{km}$; S7 = Double fossil fuel uncertainties; S8 = Half fossil fuel uncertainties; S9 = Double NEE uncertainties; S10 = Half NEE uncertainties; S11 = Domestic emission homogenised over the year; S12 = NEE fluxes averaged over the domain; S13 = Simple specification of observation error covariance matrix; S14 = Simple observation error covariance matrix with larger night-time error; S15 = Simple observation error covariance matrix with no correlation; S16 = Inversion solving for mean weekly fluxes over the month; S17 = Separate inversions for each week.

1.2.2 Monthly Aggregated Fluxes

Table S2. Aggregated CO_2 flux estimates ($kt\ CO_2$) and their uncertainties expressed as standard deviations for each month over the four-week inversion period for the reference inversion, alternative prior product inversions, and the inversions removing spatial NEE correlation and temporal observation error correlation.

	S0			S1			S2		
Month	Prior Flux (sd)	Posterior Flux (sd)	Uncertainty Reduction (%)	Prior Flux (sd)	Posterior Flux (sd)	Uncertainty Reduction (%)	Prior Flux (sd)	Posterior Flux (sd)	Uncertainty Reduction (%)
Mar-12	323 (61)	434 (36)	39.9	557 (6)	499 (5)	18.5	892 (59)	847 (38)	35.7
Apr-12	-16 (76)	47 (51)	32.5	431 (10)	326 (9)	13.6	604 (76)	465 (53)	29.2
May-12	86 (58)	-44 (49)	16.7	401 (9)	289 (8)	7	706 (59)	388 (50)	15.8
Jun-12	302 (51)	204 (47)	8.7	433 (7)	377 (7)	5.3	992 (53)	753 (48)	8.8
Jul-12	94 (65)	24 (54)	16.1	405 (8)	340 (7)	5.7	754 (66)	560 (56)	14.8
Aug-12	-381 (80)	-245 (71)	11.9	317 (11)	276 (11)	5.4	315 (82)	332 (72)	11.6
Sep-12	-980 (96)	-363 (59)	39	108 (13)	37 (10)	18	-125 (97)	20 (61)	36.8
Nov-12	-1112 (96)	-897 (81)	15.6	274 (8)	212 (8)	8.7	-251 (96)	-283 (82)	14.4
Feb-13	119 (56)	264 (36)	36	436 (5)	393 (4)	16	1006 (57)	886 (40)	30.8
Mar-13	369 (57)	354 (35)	38.2	556 (6)	459 (5)	19	941 (57)	767 (38)	33.9
Apr-13	-9 (72)	7 (52)	27.2	430 (10)	307 (9)	14.1	614 (71)	408 (54)	24.4
May-13	1 (60)	30 (39)	35.3	400 (9)	259 (8)	14.5	625 (61)	387 (41)	32.7
Jun-13	-132 (69)	-131 (49)	28.4	433 (7)	272 (6)	12.9	561 (70)	257 (51)	26.5
	S3			S4			S5		
Month	Prior Flux (sd)	Posterior Flux (sd)	Uncertainty Reduction (%)	Prior Flux (sd)	Posterior Flux (sd)	Uncertainty Reduction (%)	Prior Flux (sd)	Posterior Flux (sd)	Uncertainty Reduction (%)
Mar-12	323 (61)	436 (36)	39.9	323 (15)	360 (14)	10.6	323 (15)	360 (14)	10.7
Apr-12	-16 (76)	40 (52)	32.3	-16 (19)	-17 (17)	8.6	-16 (19)	-18 (17)	8.6
May-12	86 (58)	-44 (49)	16.6	86 (15)	21 (14)	5.1	86 (15)	21 (14)	5
Jun-12	302 (51)	204 (47)	9	302 (13)	260 (13)	2.9	302 (13)	260 (13)	3
Jul-12	94 (65)	11 (55)	15.9	94 (16)	54 (16)	4.6	94 (16)	48 (16)	4.6
Aug-12	-381 (80)	-238 (71)	12	-381 (20)	-352 (19)	3.2	-381 (20)	-352 (19)	3.2
Sep-12	-980 (96)	-364 (59)	39	-980 (24)	-812 (21)	11.1	-980 (24)	-813 (21)	11.1
Nov-12	-1112 (96)	-896 (81)	15.6	-1112 (24)	-1058 (23)	5.1	-1112 (24)	-1058 (23)	5.1
Feb-2013	119 (56)	269 (36)	35.9	119 (14)	164 (13)	9.5	119 (14)	166 (13)	9.6
Mar-13	369 (57)	357 (35)	38	369 (14)	353 (13)	11.1	369 (14)	353 (13)	11.1
Apr-13	-9 (72)	13 (52)	27.1	-9 (18)	-33 (16)	7.8	-9 (18)	-32 (16)	7.8
May-13	1 (60)	29 (39)	35.2	1 (15)	-25 (14)	10.3	1 (15)	-27 (14)	10.3
Jun-13	-132 (69)	-126 (49)	28.5	-132 (17)	-194 (16)	8.7	-132 (17)	-194 (16)	8.8

Prior and Posterior Flux refer to the total flux from the domain over the thirteen four-week periods. The sd of the fluxes refers to the uncertainty in the total flux estimate. The sd of the χ^2 statistic refers to the standard deviation between the χ^2 statistics of the thirteen four-week period χ^2 Statistics. S0 = Reference Inversion; S1 = Carbon Assessment Inversion; S2 = ODIAC fossil fuel inversion; S3 = Correlation for NEE flux uncertainties only; S4 = Correlation for observation errors only; S5 = No correlation specified in prior covariance matrices; S6 = Correlation length for NEE flux uncertainties set at $7km$; S7 = Double fossil fuel uncertainties; S8 = Half fossil fuel uncertainties; S9 = Double NEE uncertainties; S10 = Half NEE uncertainties; S11 = Domestic emission homogenised over the year; S12 = NEE fluxes averaged over the domain; S13 = Simple specification of observation error covariance matrix; S14 = Simple observation error covariance matrix with larger night-time error; S15 = Simple observation error covariance matrix with no correlation; S16 = Inversion solving for mean weekly fluxes over the month; S17 = Separate inversions for each week.

Table S3. Aggregated CO_2 flux estimates ($kt\ CO_2$) and their uncertainties expressed as standard deviations for each month over the four-week inversion period for test cases considered different relative uncertainty in the fossil fuel and NEE fluxes, and inversion considered temporally homogenised prior domestic emissions and spatially homogenised prior NEE fluxes.

	S6			S7			S8		
Month	Prior Flux (sd)	Posterior Flux (sd)	Uncertainty Reduction (%)	Prior Flux (sd)	Posterior Flux (sd)	Uncertainty Reduction (%)	Prior Flux (sd)	Posterior Flux (sd)	Uncertainty Reduction (%)
Mar-12	323 (61)	460 (37)	39.1	323 (61)	408 (36)	40.3	323 (61)	445 (36)	40.4
Apr-12	-16 (76)	85 (52)	32	-16 (76)	21 (51)	32.7	-15(76)	39 (51)	33.5
May-12	86 (59)	-31 (49)	16.6	86 (58)	-48 (49)	16.8	86 (59)	-45 (48)	17.0
Jun-12	302 (51)	208 (47)	8.7	302 (51)	201 (47)	8.7	302 (51)	188 (46)	9.3
Jul-12	94 (65)	40 (55)	15.9	94 (65)	15 (54)	16.2	94 (65)	30 (54)	16.9
Aug-12	-381 (81)	-238 (71)	11.8	-381 (80)	-255 (71)	12	-381 (80)	-331 (71)	12.2
Sep-12	-980 (96)	-362 (59)	38.8	-980 (96)	-363 (59)	39.1	-980 (96)	-384 (58)	39.4
Nov-12	-1112 (97)	-890 (82)	15.5	-1112 (96)	-904 (81)	15.6	-1112 (96)	-892 (81)	15.6
Feb-13	119 (57)	270 (37)	35.5	119 (56)	261 (36)	36.1	119 (56)	236 (36)	36.4
Mar-13	369 (57)	371 (36)	37.6	369 (57)	341 (35)	38.5	369 (57)	360 (35)	38.6
Apr-13	-9 (72)	20 (52)	26.9	-9 (72)	3 (52)	27.3	-90 (72)	17 (52)	27.6
May-13	1 (61)	37 (39)	35.1	1 (60)	32 (39)	35.4	1 (60)	7 (39)	35.9
Jun-13	-132 (69)	-119 (50)	28.3	-132 (69)	-134 (49)	28.5	-132 (69)	-166 (49)	28.8

	S9			S10			S11		
Month	Prior Flux (sd)	Posterior Flux (sd)	Uncertainty Reduction (%)	Prior Flux (sd)	Posterior Flux (sd)	Uncertainty Reduction (%)	Prior Flux (sd)	Posterior Flux (sd)	Uncertainty Reduction (%)
Mar-12	323 (121)	402 (69)	43.3	323 (30)	447 (20)	34.8	240 (61)	379 (36)	40.0
Apr-12	-16 (152)	48 (97)	36.6	-16 (38)	49 (28)	26.8	-99 (76)	12 (51)	32.6
May-12	86 (117)	-62 (93)	19.9	86 (29)	-18 (26)	13	3 (58)	-79 (49)	16.7
Jun-12	302 (102)	190 (92)	10	302 (26)	221 (24)	6.9	219 (51)	143 (47)	8.7
Jul-12	94 (130)	37 (106)	18.5	94 (33)	34 (28)	12.8	11 (65)	-24 (54)	16.1
Aug-12	-381 (161)	-221 (139)	13.5	-381 (40)	-272 (36)	9.9	-464 (80)	-307 (71)	11.9
Sep-12	-980 (192)	-331 (111)	42.3	-980 (48)	-423 (32)	34	-897 (96)	-344 (59)	38.9
Nov-12	-1112 (193)	-893 (160)	16.8	-1112 (48)	-914 (42)	13.9	-1029 (96)	-849 (81)	15.6
Feb-13	119 (113)	261 (69)	38.8	119 (28)	269 (19)	31.5	202 (56)	309 (36)	35.9
Mar-13	369 (114)	338 (66)	42.2	369 (29)	371 (19)	32.8	286 (57)	308 (35)	38.2
Apr-13	-9 (143)	11 (100)	30.2	-9 (36)	7 (28)	23	-92 (72)	-25 (52)	27.2
May-13	1 (121)	36 (74)	39.1	1 (30)	36 (21)	30.1	-81 (60)	5 (39)	35.4
Jun-13	-132 (138)	-131 (95)	31.4	-132 (35)	-144 (26)	24.3	-215 (69)	-152 (49)	28.5

Prior and Posterior Flux refer to the total flux from the domain over the thirteen four-week periods. The sd of the fluxes refers to the uncertainty in the total flux estimate. The sd of the χ^2 statistic refers to the standard deviation between the χ^2 statistics of the thirteen four-week period χ^2 Statistics. S0 = Reference Inversion; S1 = Carbon Assessment Inversion; S2 = ODIAC fossil fuel inversion; S3 = Correlation for NEE flux uncertainties only; S4 = Correlation for observation errors only; S5 = No correlation specified in prior covariance matrices; S6 = Correlation length for NEE flux uncertainties set at 7km; S7 = Double fossil fuel uncertainties; S8 = Half fossil fuel uncertainties; S9 = Double NEE uncertainties; S10 = Half NEE uncertainties; S11 = Domestic emission homogenised over the year; S12 = NEE fluxes averaged over the domain; S13 = Simple specification of observation error covariance matrix; S14 = Simple observation error covariance matrix with larger night-time error; S15 = Simple observation error covariance matrix with no correlation; S16 = Inversion solving for mean weekly fluxes over the month; S17 = Separate inversions for each week.

Table S4. Aggregated CO_2 flux estimates ($kt\ CO_2$) and their uncertainties expressed as standard deviations for each month over the four-week inversion period for the simplified observation error test cases, and the alternative control vector inversions.

	S12			S13			S14		
Month	Prior Flux (sd)	Posterior Flux (sd)	Uncertainty Reduction (%)	Prior Flux (sd)	Posterior Flux (sd)	Uncertainty Reduction (%)	Prior Flux (sd)	Posterior Flux (sd)	Uncertainty Reduction (%)
Mar-12	323 (29)	196 (24)	16.1	323 (61)	433 (36)	40.4	323 (61)	417 (38)	38.1
Apr-12	-15 (37)	-79 (30)	17.8	-16 (76)	62 (51)	33.3	-16 (76)	6 (53)	30.2
May-12	86 (28)	12 (24)	15	86 (58)	-67 (48)	17.3	86 (58)	-74 (49)	15.8
Jun-12	303 (25)	224 (23)	6.8	302 (51)	202 (47)	8.9	302 (51)	199 (47)	8.2
Jul-12	95 (31)	7 (28)	9.9	94 (65)	27 (54)	16.6	94 (65)	-1 (55)	15.1
Aug-12	-380 (39)	-332 (37)	6.8	-381 (80)	-240 (70)	12.3	-381 (80)	-242 (71)	11.9
Sep-12	-978 (49)	-632 (36)	25.9	-980 (96)	-362 (58)	39.5	-980 (96)	-417 (60)	37.1
Nov-12	-1111 (52)	-1000 (46)	11.4	-1112 (96)	-892 (81)	15.8	-1112 (96)	-923 (83)	14.4
Feb-13	119 (29)	75 (24)	16.5	119 (56)	263 (36)	36.5	119 (56)	259 (37)	34.1
Mar-13	368 (28)	200 (23)	19.1	369 (57)	359 (35)	38.8	369 (57)	338 (36)	36.5
Apr-13	-9 (34)	-68 (29)	17	-9 (72)	12 (52)	28	-9 (72)	7 (53)	26.2
May-13	2 (30)	-97 (24)	19.3	1 (60)	17 (39)	36.1	1 (60)	12 (40)	34
Jun-13	-131 (34)	-214 (27)	21.4	-132 (69)	-139 (49)	28.9	-132 (69)	-159 (50)	27.5
	S15			S16			S17		
Mar-12	323 (61)	435 (36)	40.4	323 (30)	428 (12)	59.5	323 (59)	406 (36)	38.8
Apr-12	-16 (76)	55 (51)	33.1	-16 (37)	64 (16)	56.9	-53 (76)	-26 (47)	38
May-12	86 (58)	-66 (48)	17.2	86 (29)	47 (16)	44.2	86 (58)	-5 (48)	15.8
Jun-12	302 (51)	197 (46)	9.2	302 (25)	98 (18)	29.4	380 (51)	151 (42)	16.9
Jul-12	94 (65)	1 (54)	16.4	94 (32)	1 (21)	35	17 (70)	-100 (54)	23.3
Aug-12	-381 (80)	-229 (70)	12.4	-381 (40)	-54 (28)	30.8	-381 (80)	-265 (71)	12.1
Sep-12	-980 (96)	-365 (58)	39.5	-980 (48)	-66 (18)	63.4	-980 (96)	-435 (62)	35.2
Nov-12	-1112 (96)	-892 (81)	15.8	-1112 (48)	-609 (29)	38.5	-956 (89)	-779 (74)	16.8
Feb-13	119 (56)	268 (36)	36.4	119 (28)	271 (13)	54.1	116 (55)	193 (35)	37
Mar-13	369 (57)	361 (35)	38.6	369 (28)	237 (12)	58.8	369 (56)	354 (37)	33.7
Apr-13	-9 (72)	17 (52)	27.9	-9 (35)	75 (18)	49	-9 (70)	-27 (53)	24.4
May-13	1 (60)	15 (39)	36	1 (30)	72 (12)	60.1	1 (60)	18 (40)	32.2
Jun-13	-132 (69)	-135 (49)	28.9	-132 (34)	98 (17)	50	-132 (68)	-173 (53)	23.2

Prior and Posterior Flux refer to the total flux from the domain over the thirteen four-week periods. The sd of the fluxes refers to the uncertainty in the total flux estimate. The sd of the χ^2 statistic refers to the standard deviation between the χ^2 statistics of the thirteen four-week period χ^2 Statistics. S0 = Reference Inversion; S1 = Carbon Assessment Inversion; S2 = ODIAC fossil fuel inversion; S3 = Correlation for NEE flux uncertainties only; S4 = Correlation for observation errors only; S5 = No correlation specified in prior covariance matrices; S6 = Correlation length for NEE flux uncertainties set at $7km$; S7 = Double fossil fuel uncertainties; S8 = Half fossil fuel uncertainties; S9 = Double NEE uncertainties; S10 = Half NEE uncertainties; S11 = Domestic emission homogenised over the year; S12 = NEE fluxes averaged over the domain; S13 = Simple specification of observation error covariance matrix; S14 = Simple observation error covariance matrix with larger night-time error; S15 = Simple observation error covariance matrix with no correlation; S16 = Inversion solving for mean weekly fluxes over the month; S17 = Separate inversions for each week.

1.2.3 Weekly Aggregated Fluxes

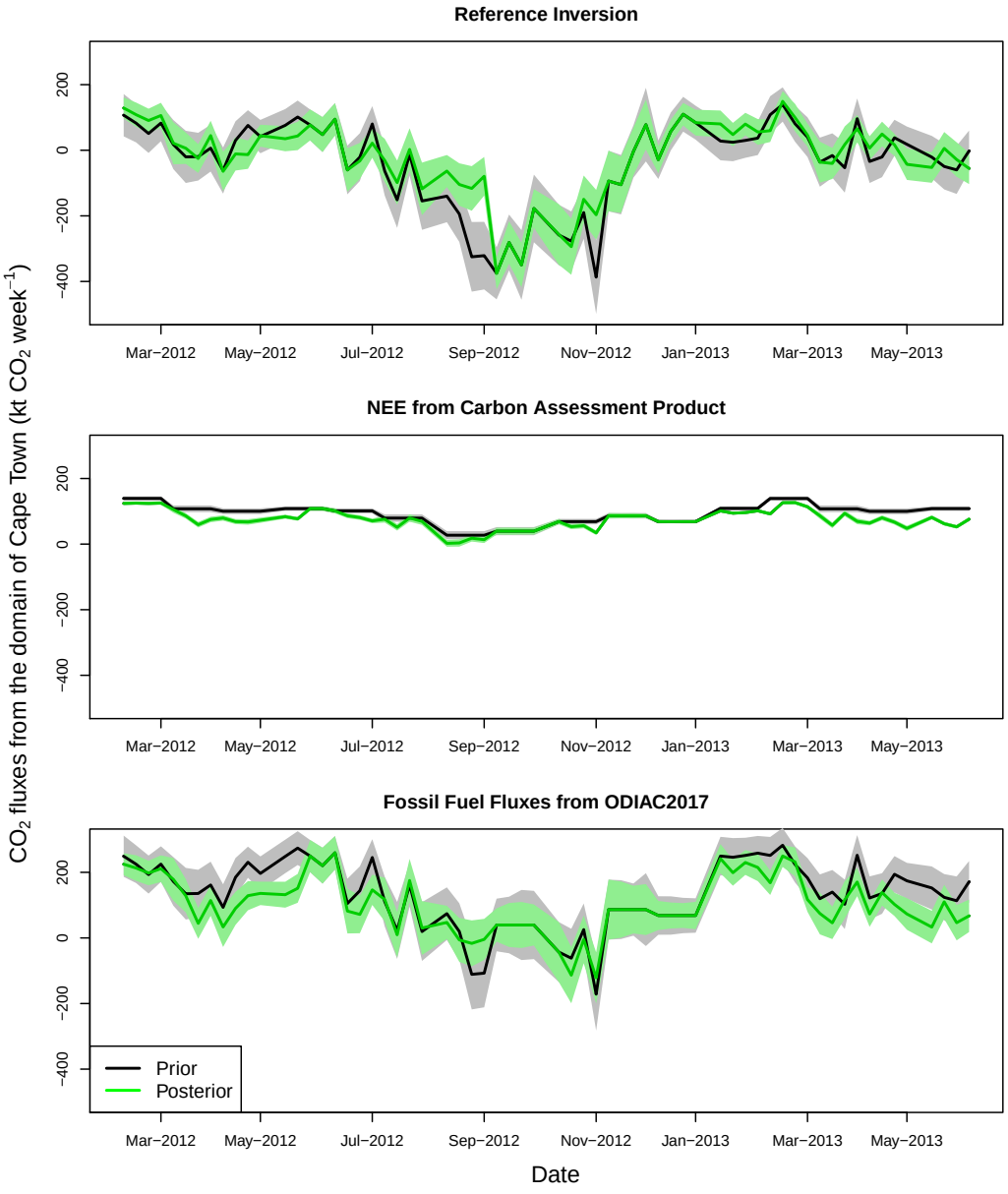

Figure S2. Prior and posterior aggregated weekly fluxes over the inversion domain from March 2012 to June 2013 for the reference inversion S0 (top) and the inversions making use of the carbon assessment product for the prior NEE fluxes S1 (middle) and the inversion using the ODIAC fossil fuel product for prior fossil fuel fluxes S2 (bottom).

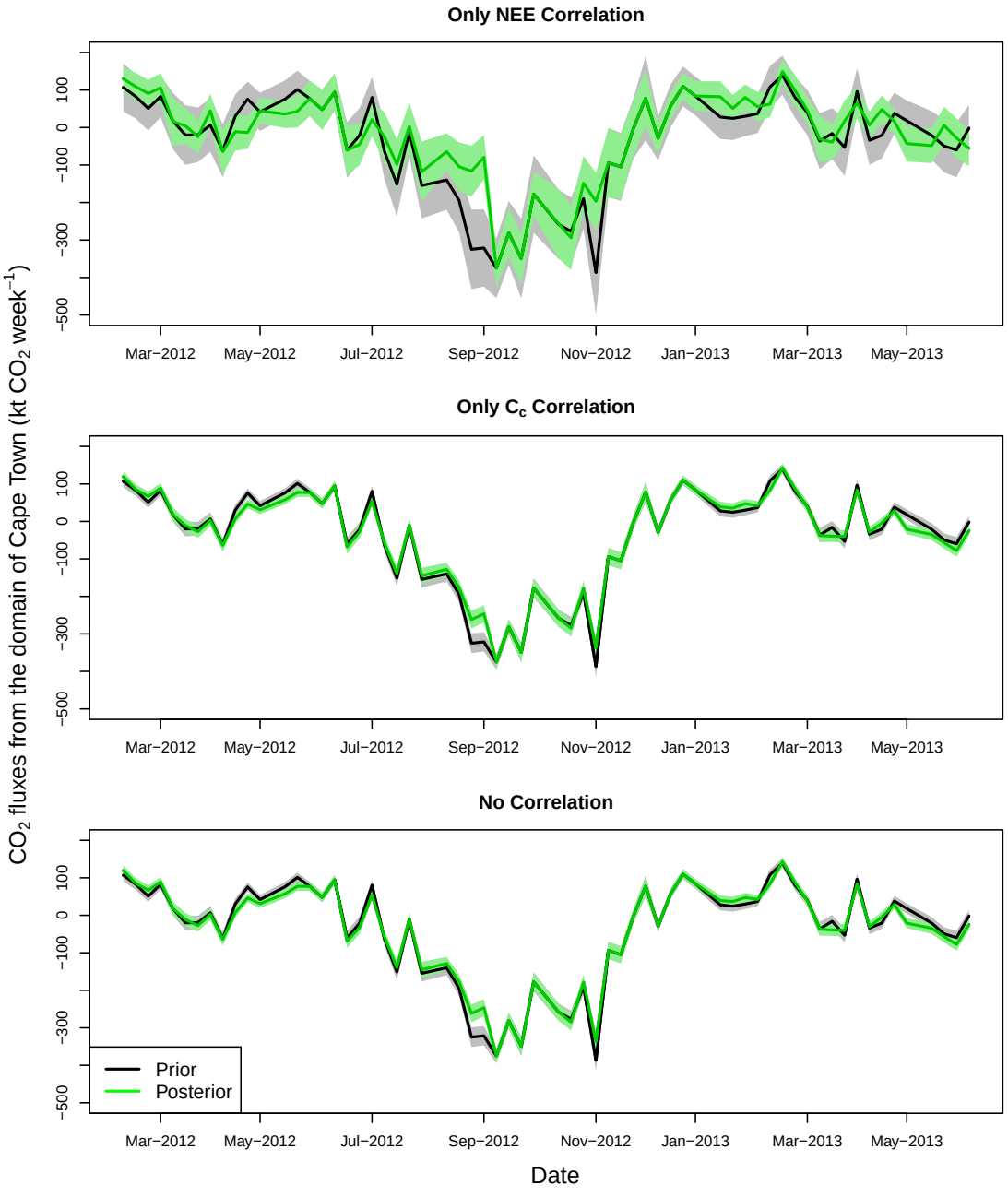

Figure S3. Prior and posterior aggregated weekly fluxes over the inversion domain from March 2012 to June 2013 for the inversion accounting for only correlation between NEE flux uncertainties S3 (top) the inversion accounting for only correlation between the observation errors S4 (middle) and the inversion with no correlation in the prior uncertainty covariance matrices S5 (bottom).

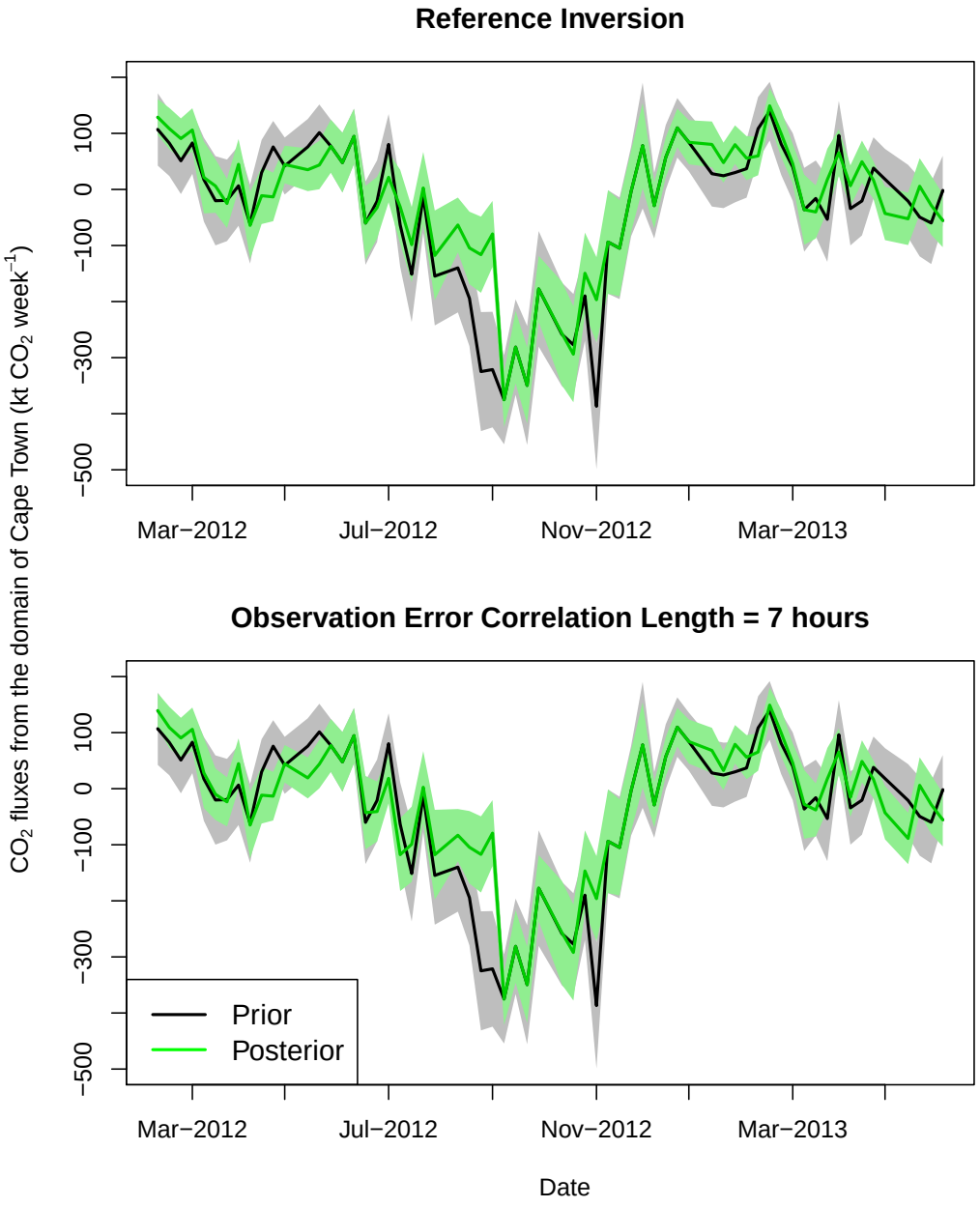

Figure S4. Prior and posterior aggregated weekly fluxes over the inversion domain from March 2012 to June 2013 for the reference inversion S0 (top) and the inversion with seven hour observation error correlation length S6 (bottom).

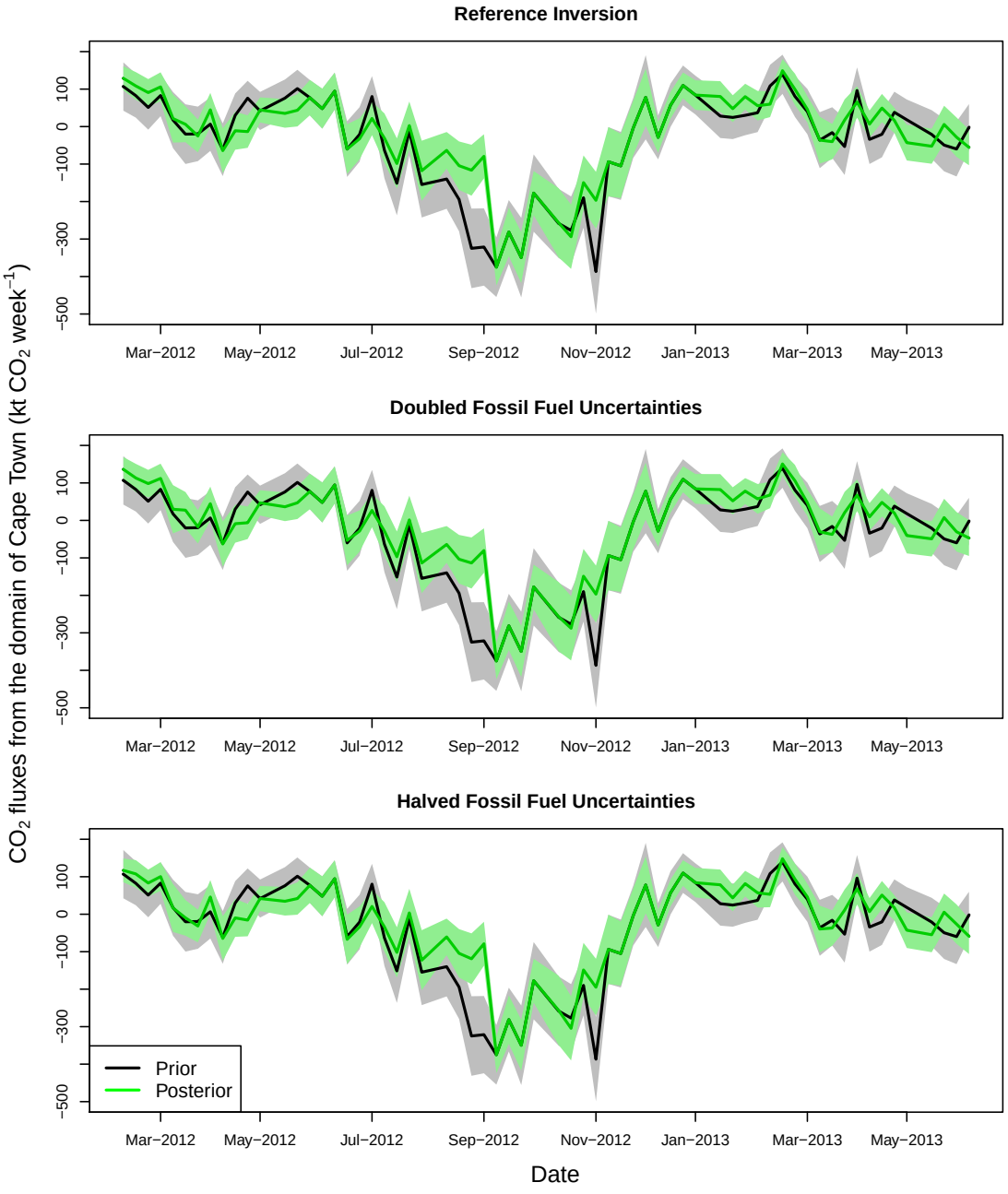

Figure S5. Prior and posterior aggregated weekly fluxes over the inversion domain from March 2012 to June 2013 for the reference inversion S0 (top) and the inversions doubling S7 (middle) and halving S8 (bottom) the uncertainty in the fossil fuel fluxes.

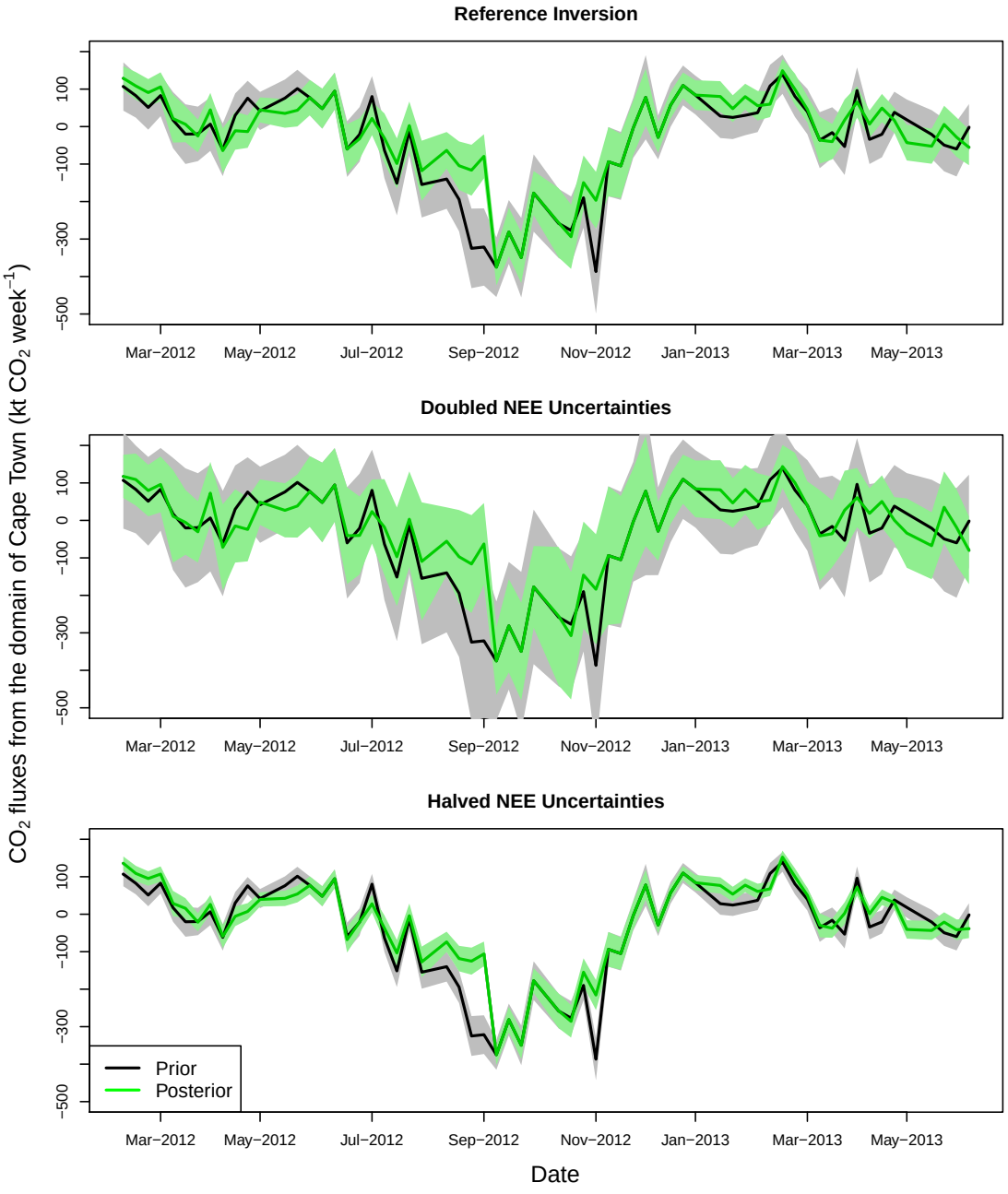

Figure S6. Prior and posterior aggregated weekly fluxes over the inversion domain from March 2012 to June 2013 for the reference inversion S0 (top) and the inversions doubling S9 (middle) and halving S10 (bottom) the uncertainty in the NEE fluxes.

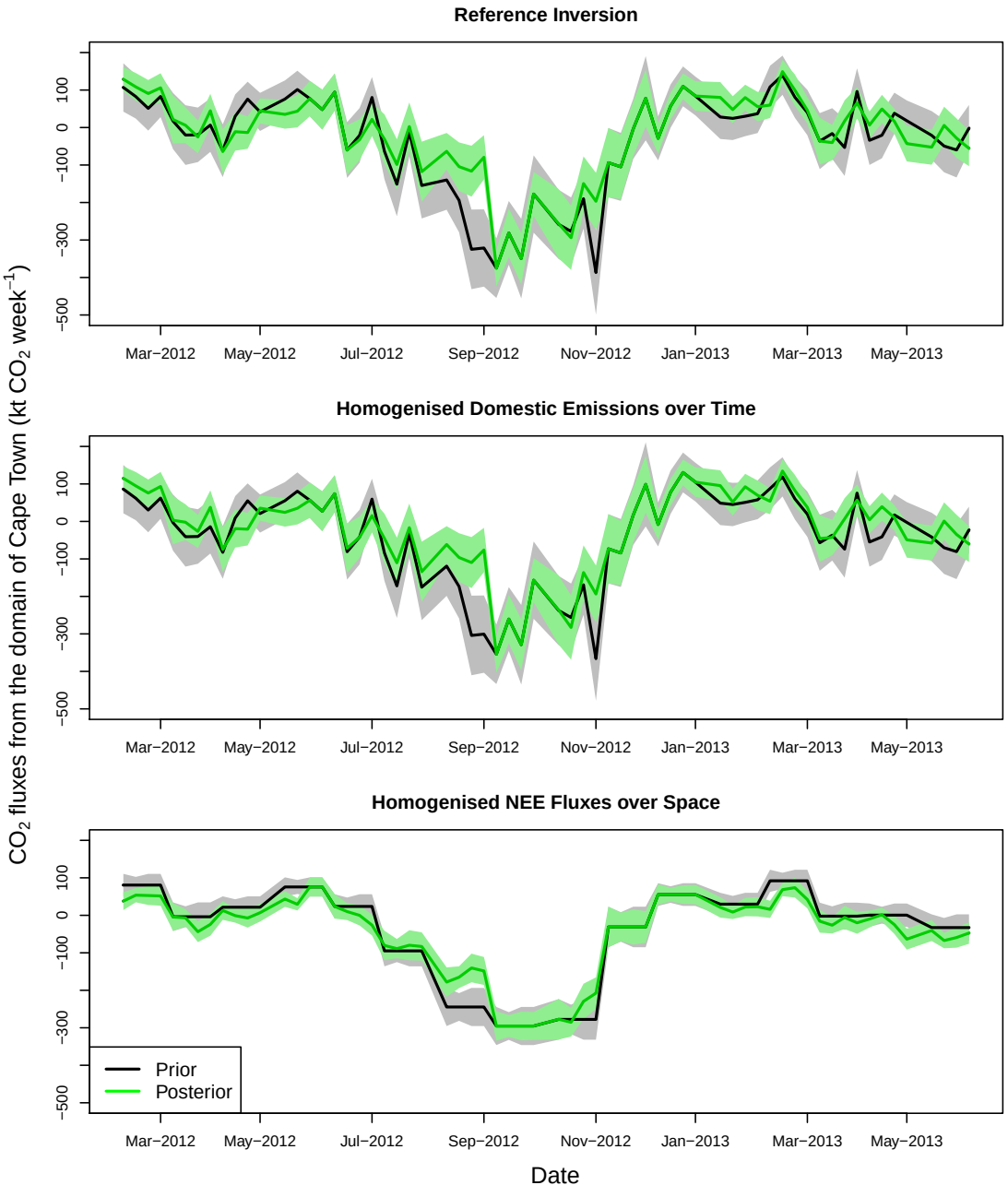

Figure S7. Prior and posterior aggregated weekly fluxes over the inversion domain from March 2012 to June 2013 for the reference inversion S0 (top) and the inversions making use of the temporally homogenised domestic fossil fuel prior S11 (middle) and spatially homogenised NEE flux prior S12 (bottom).

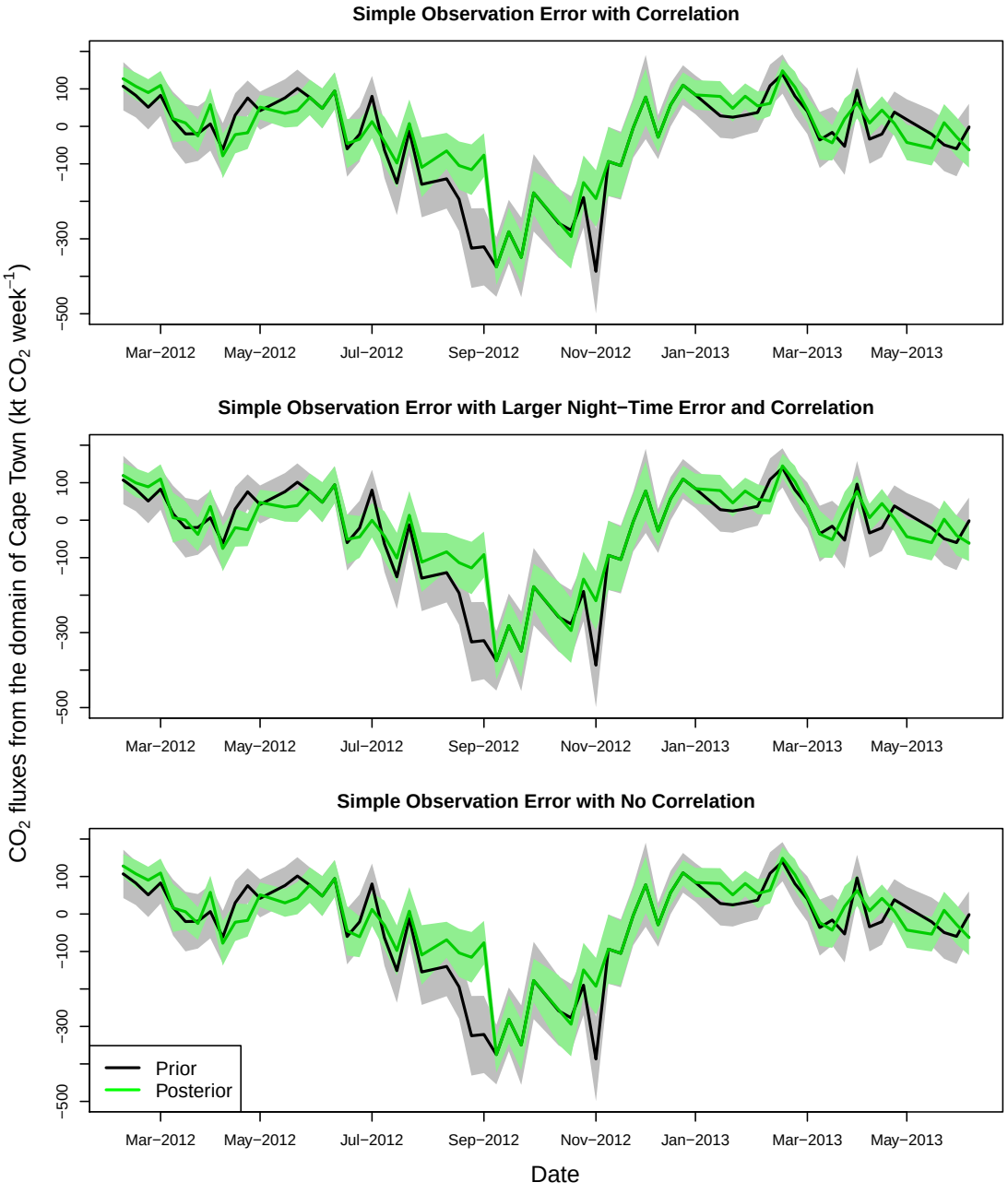

Figure S8. Prior and posterior aggregated weekly fluxes over the inversion domain from March 2012 to June 2013 for the inversion specifying uncertainties of 2 ppm and 4 ppm for the day and night-time observation errors S13 (top), the inversion specifying uncertainties of 2 ppm and 10 ppm for the day and night-time observation errors S14 (middle), and the inversion specifying uncertainties of 2 ppm and 4 ppm for the day and night-time observation errors with no correlation between observation errors S15 (bottom).

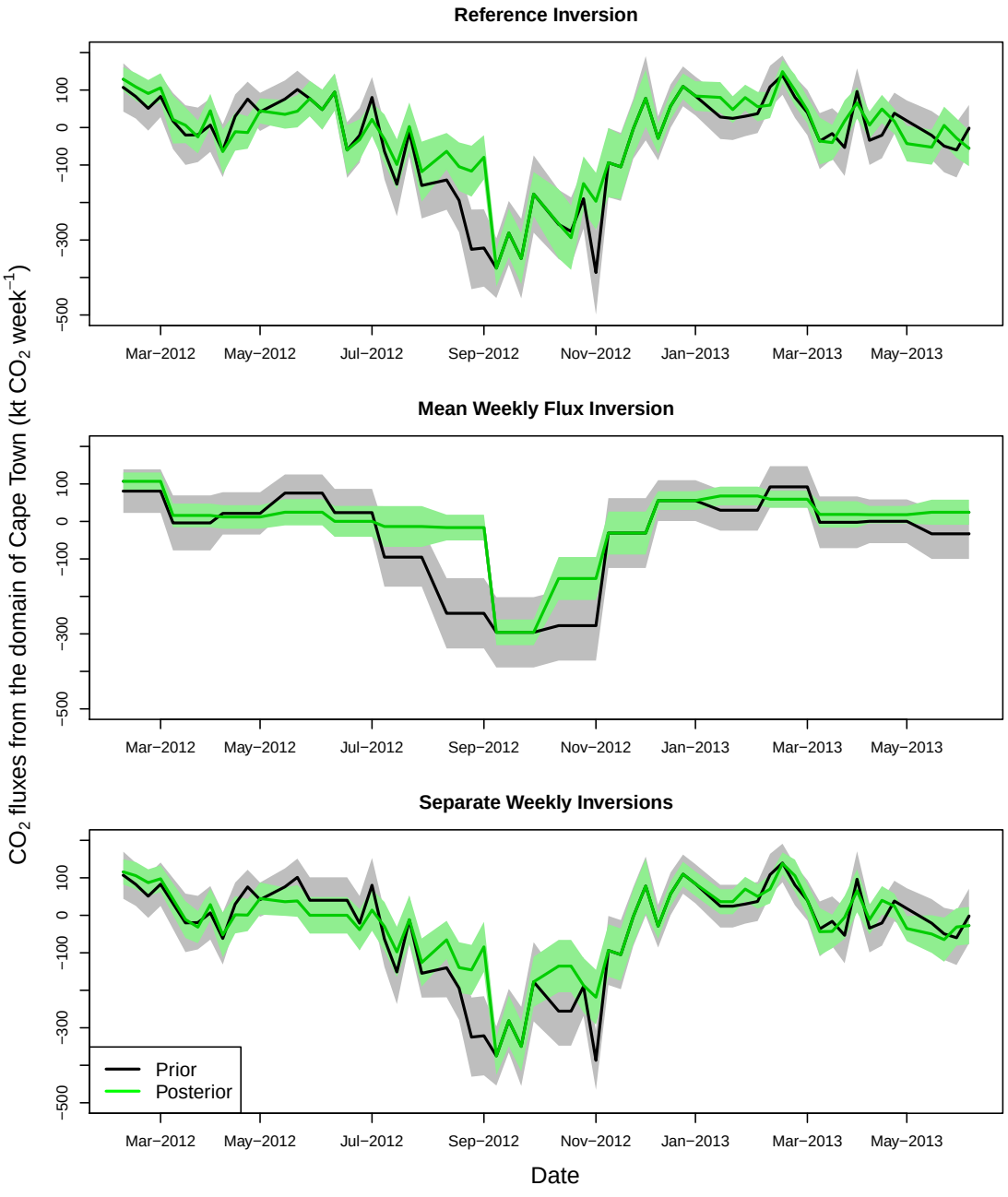

Figure S9. Prior and posterior aggregated weekly fluxes over the inversion domain from March 2012 to June 2013 for the reference inversion, which was a monthly inversion solving for separate weekly fluxes S0 (top), the inversion solving for the mean weekly fluxes S16 (middle), and the separate weekly inversions S17 (bottom).

1.3 Observed versus Modelled Concentrations

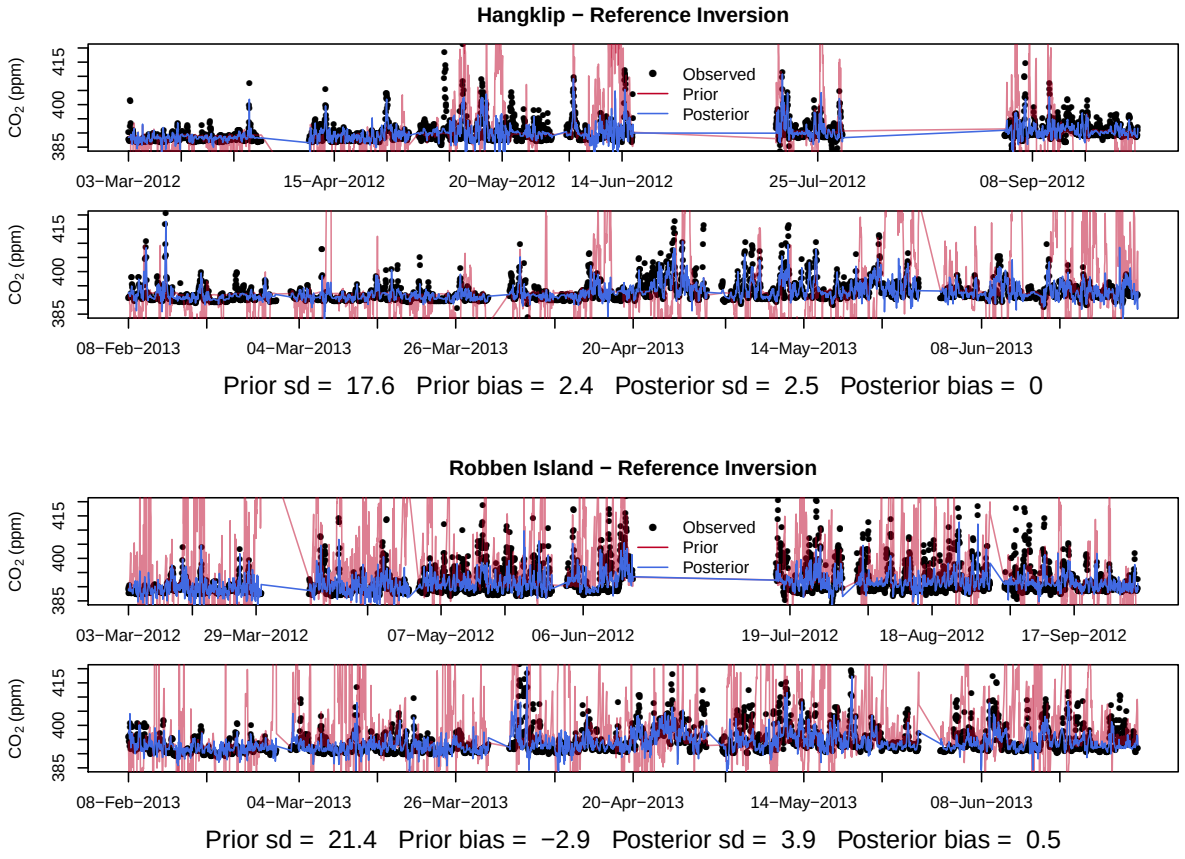

Figure S10. Prior and posterior modelled concentrations at Hangklip and Robben Island sites under the reference inversion S0 over the full inversion period from March 2012 until June 2013.

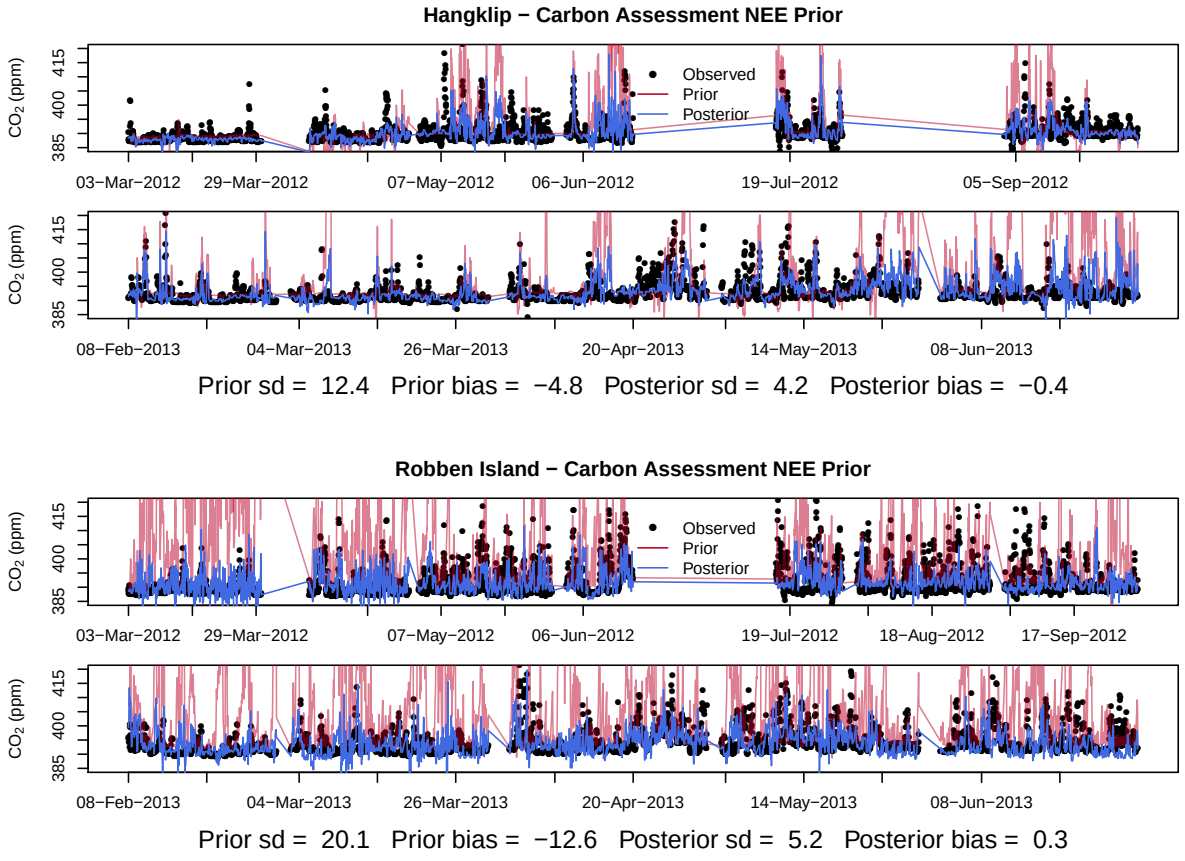

Figure S11. Prior and posterior modelled concentrations at Hangklip and Robben Island sites under the inversion using the carbon assessment product for the NEE prior S1 over the full inversion period from March 2012 until June 2013.

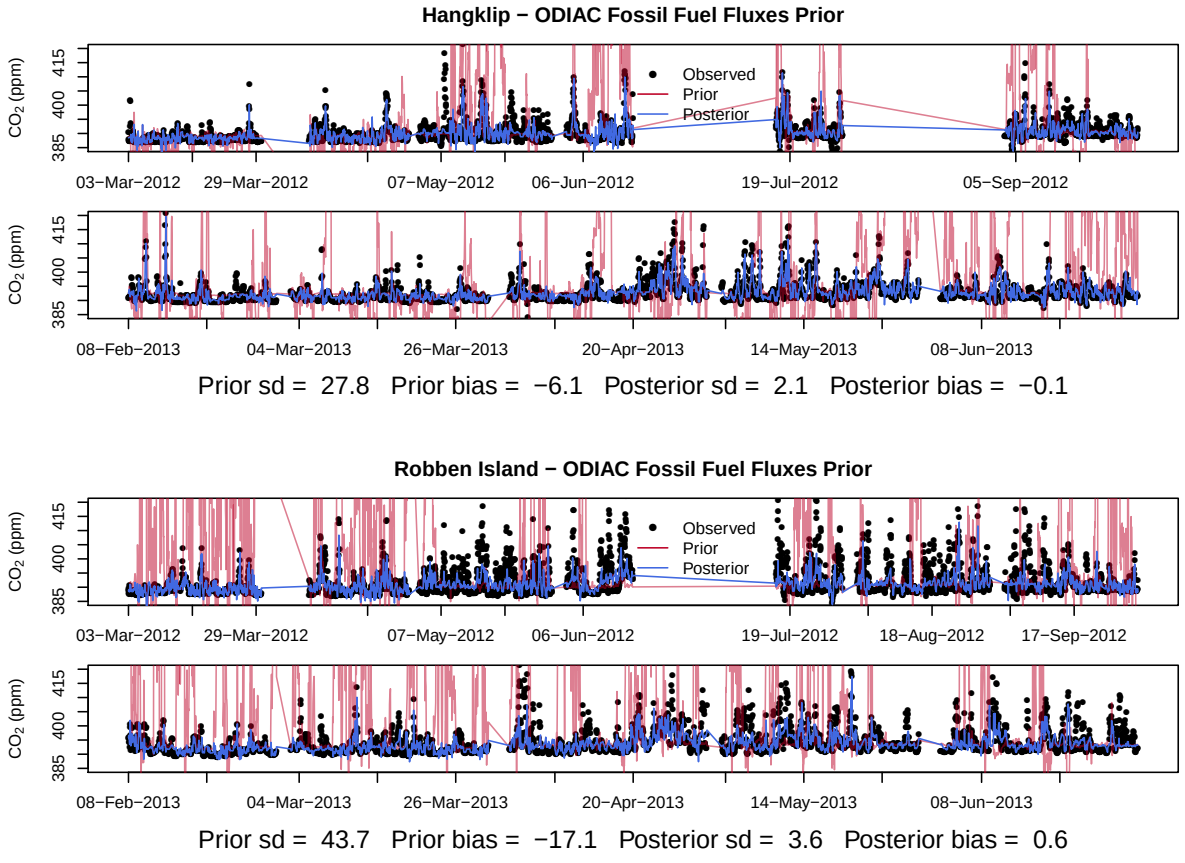

Figure S12. Prior and posterior modelled concentrations at Hangklip and Robben Island sites under the inversion using the ODIAC fossil fuel emission product for the fossil fuel flux prior S2 over the full inversion period from March 2012 until June 2013.

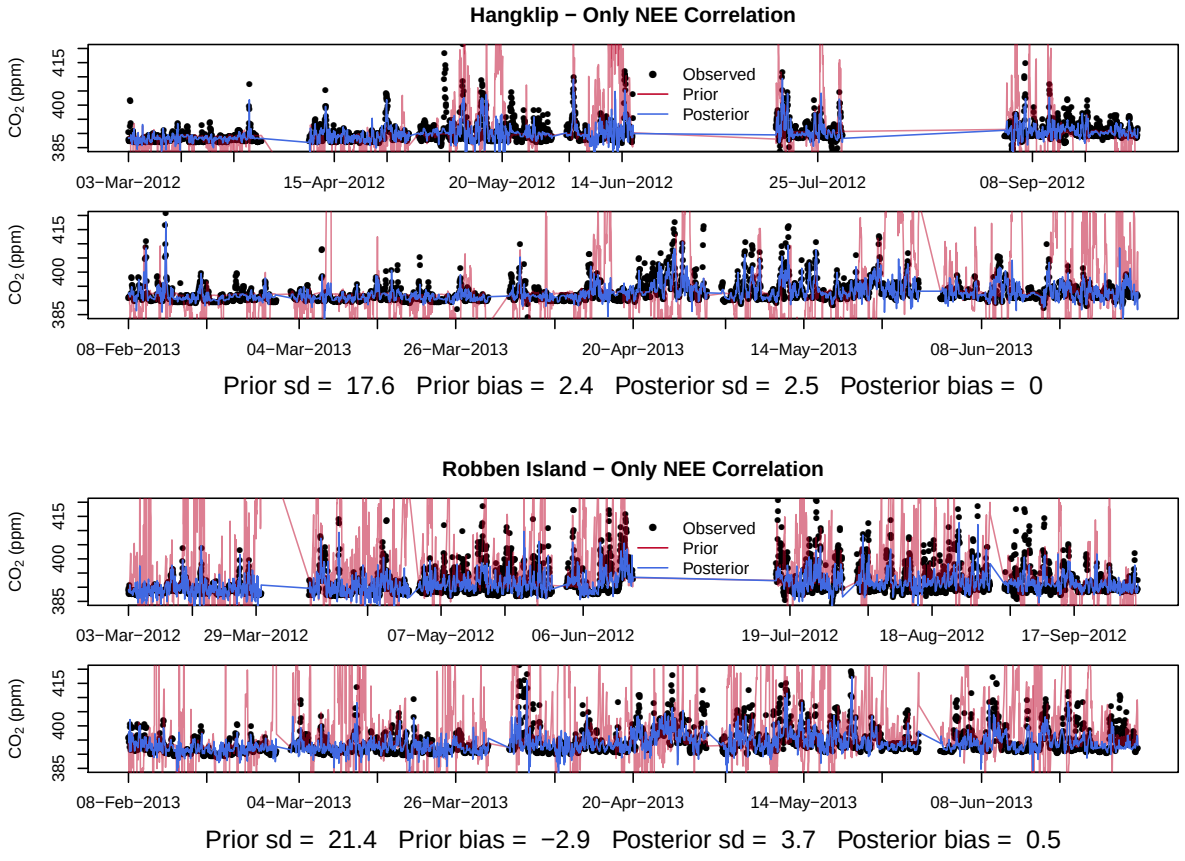

Figure S13. Prior and posterior modelled concentrations at Hangklip and Robben Island sites under the inversion with only correlation accounted for between the uncertainties in the NEE fluxes S3 over the full inversion period from March 2012 until June 2013.

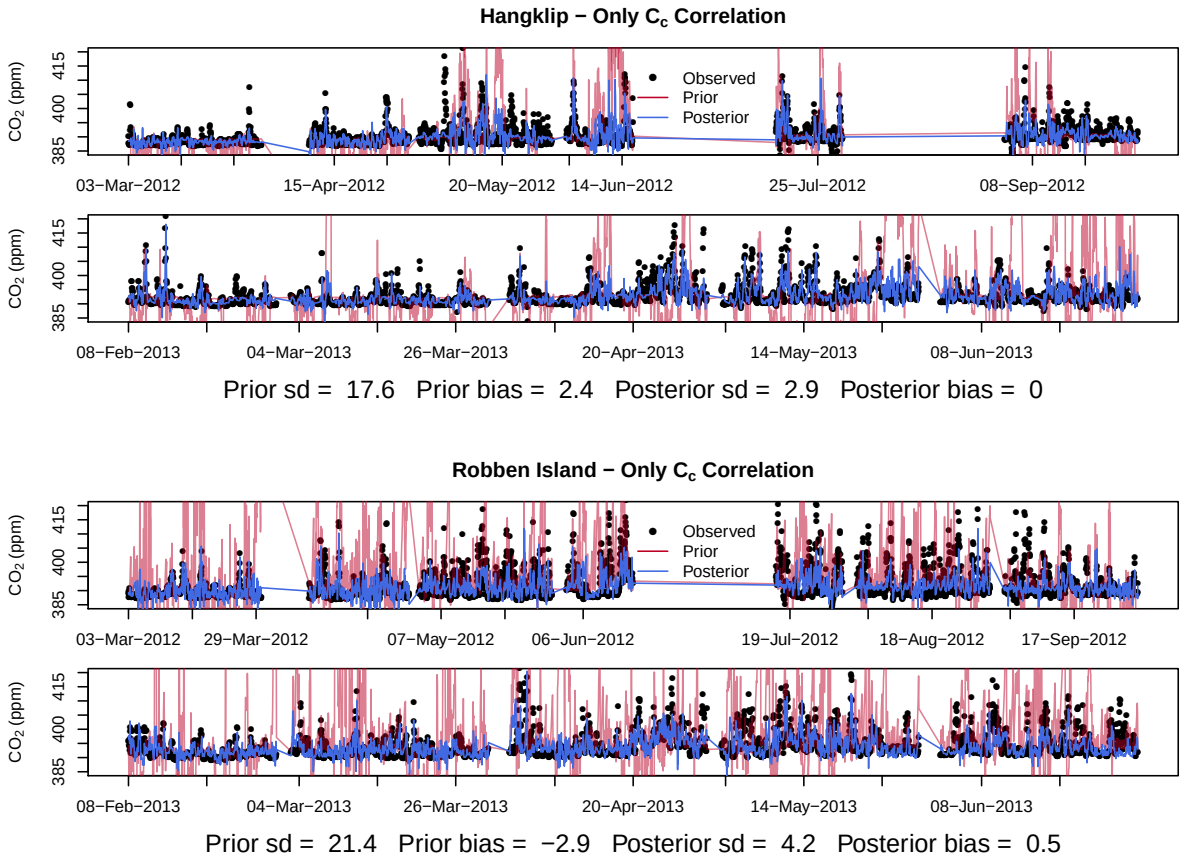

Figure S14. Prior and posterior modelled concentrations at Hangklip and Robben Island sites under the inversion with only correlation accounted between the observation errors and ignoring correlations between the uncertainties in the NEE fluxes S4 over the full inversion period from March 2012 until June 2013.

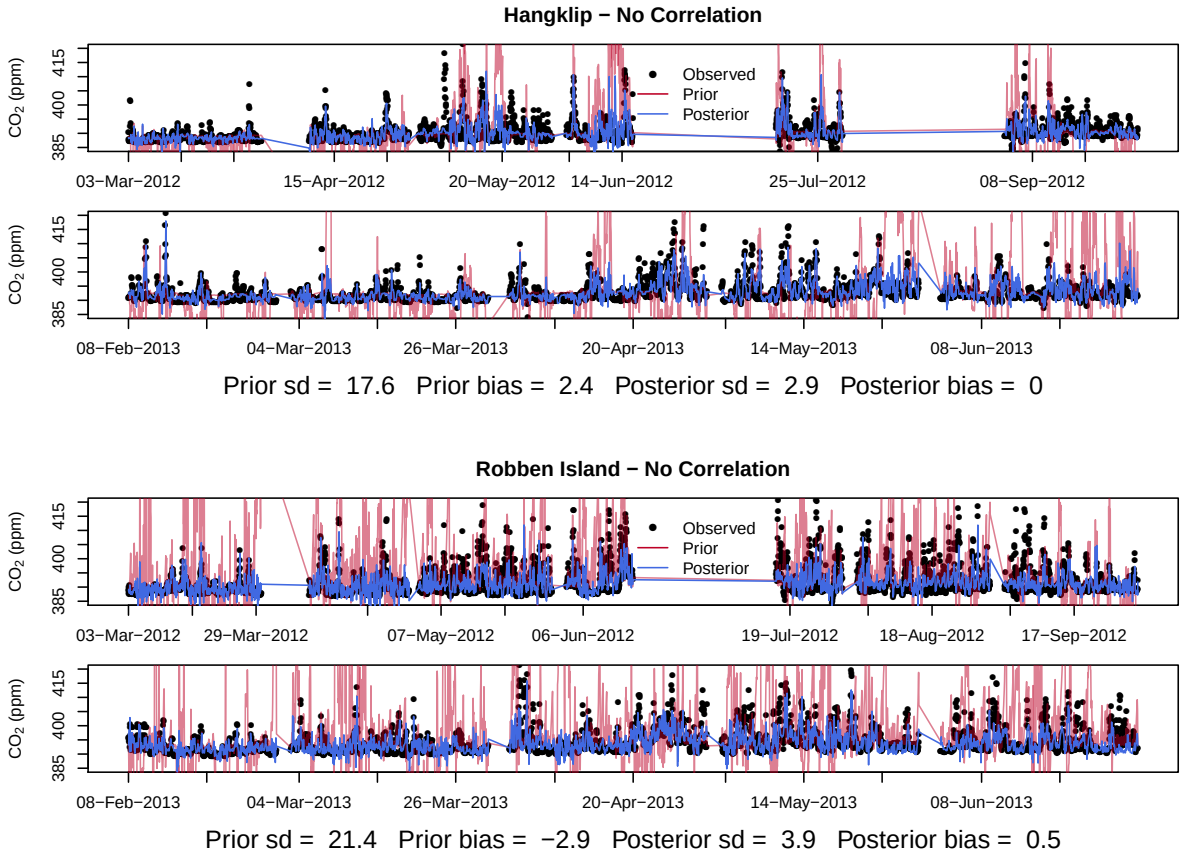

Figure S15. Prior and posterior modelled concentrations at Hangklip and Robben Island sites under the inversion which ignored correlations between the observation errors and correlations between the uncertainties in the NEE fluxes S5 over the full inversion period from March 2012 until June 2013.

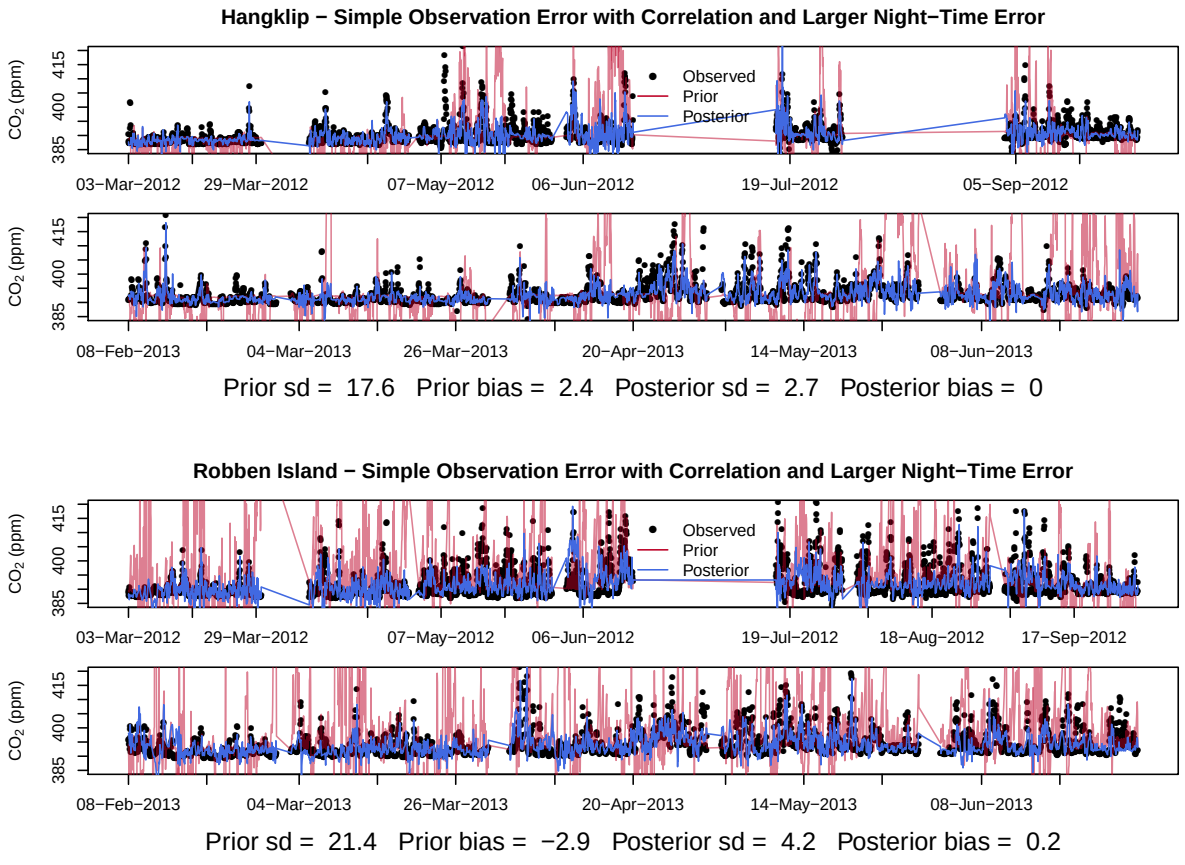

Figure S16. Prior and posterior modelled concentrations at Hangklip and Robben Island sites under the inversion which allocated an observation error correlation length of seven hours S6 over the full inversion period from March 2012 until June 2013.

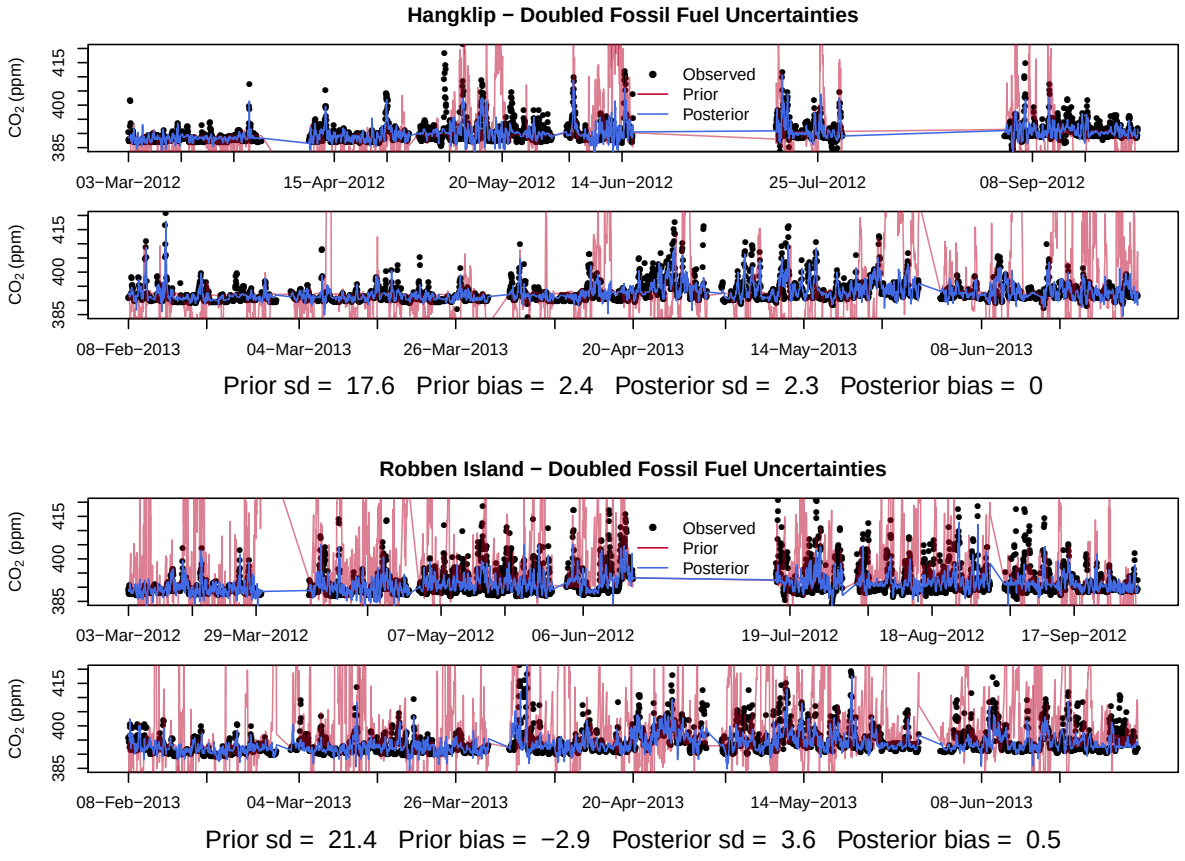

Figure S17. Prior and posterior modelled concentrations at Hangklip and Robben Island sites under the inversion where uncertainties in the fossil fuel fluxes were doubled S7 over the full inversion period from March 2012 until June 2013.

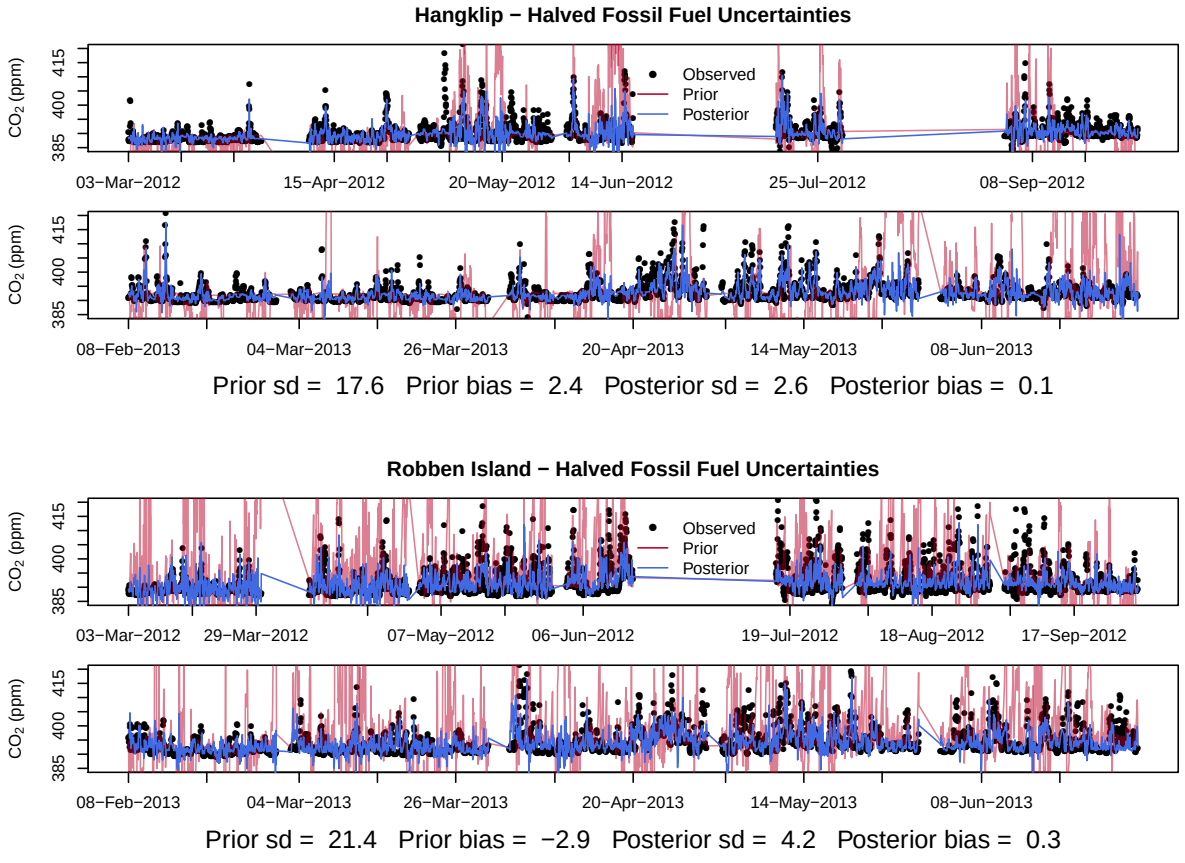

Figure S18. Prior and posterior modelled concentrations at Hangklip and Robben Island sites under the inversion where uncertainties in the fossil fuel fluxes were halved S8 over the full inversion period from March 2012 until June 2013.

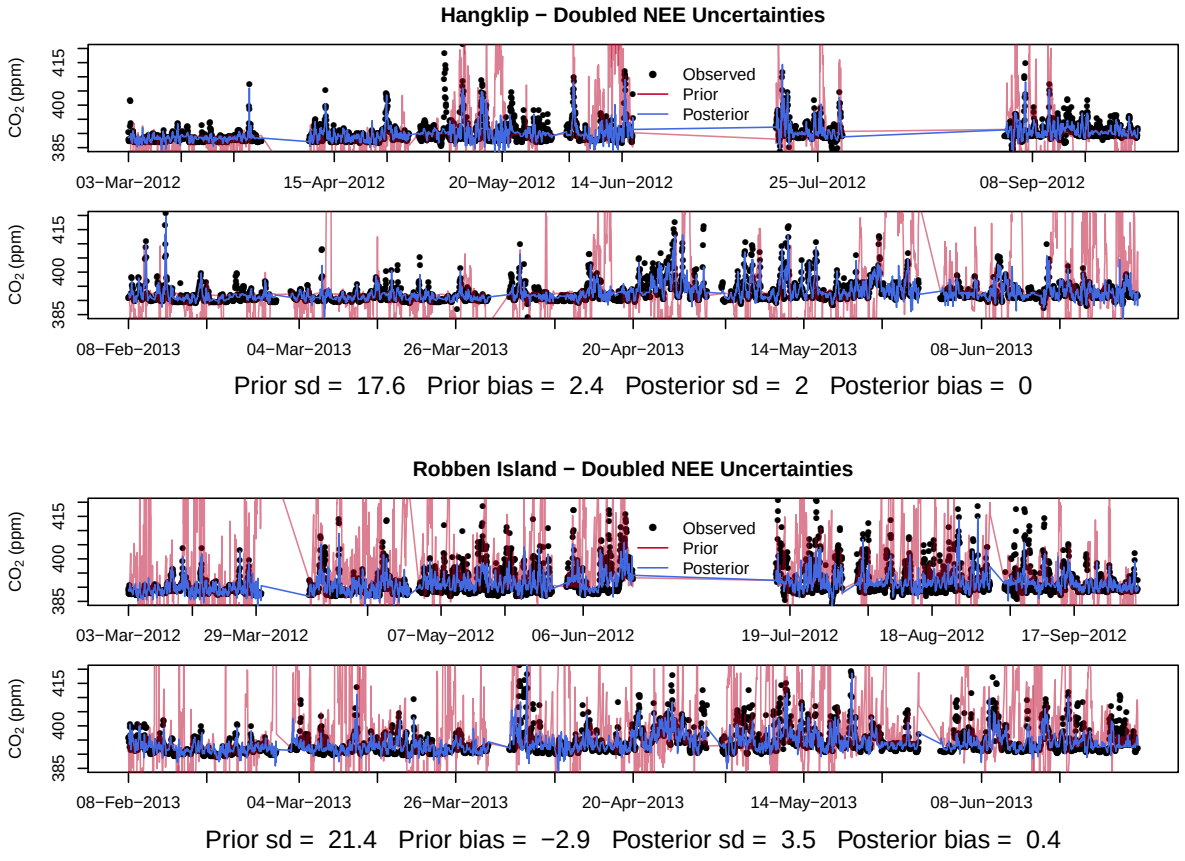

Figure S19. Prior and posterior modelled concentrations at Hangklip and Robben Island sites under the inversion where uncertainties in the NEE fluxes were doubled S9 over the full inversion period from March 2012 until June 2013.

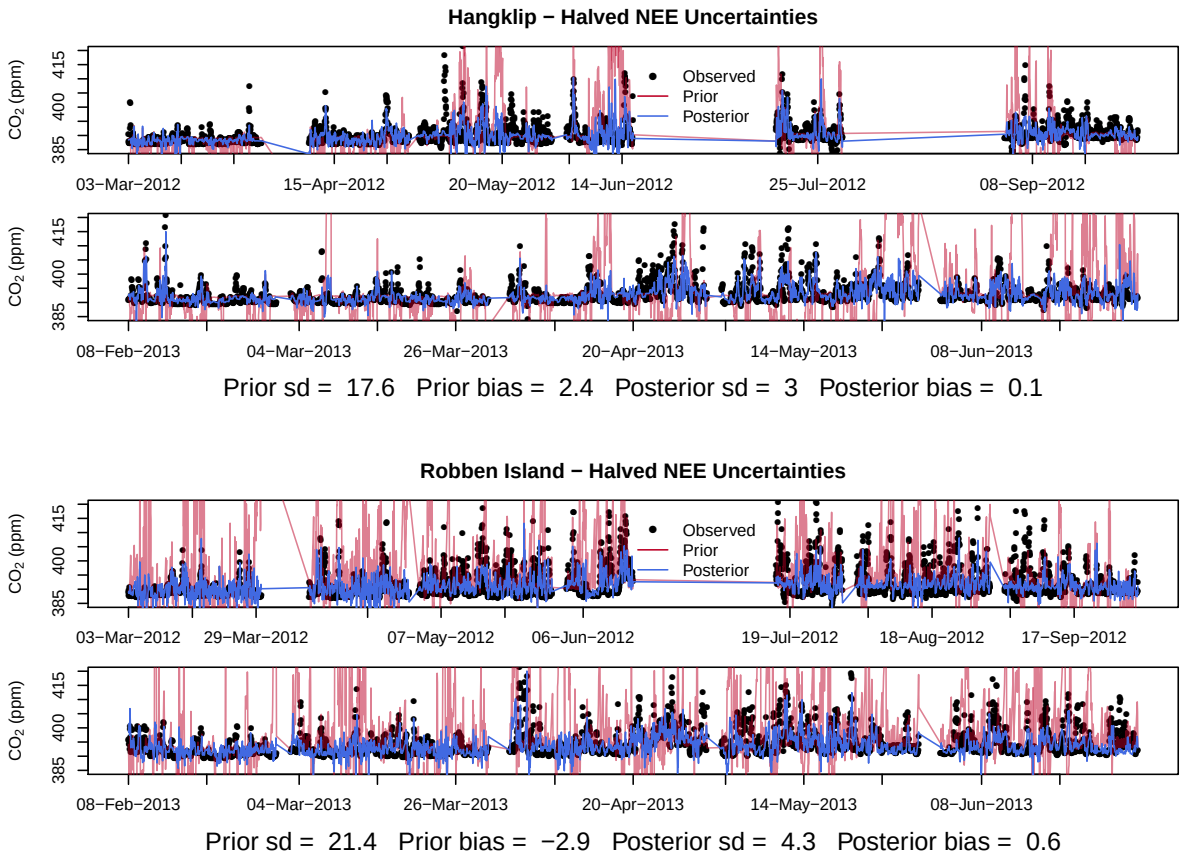

Figure S20. Prior and posterior modelled concentrations at Hangklip and Robben Island sites under the inversion where uncertainties in the NEE fluxes were halved S10 over the full inversion period from March 2012 until June 2013.

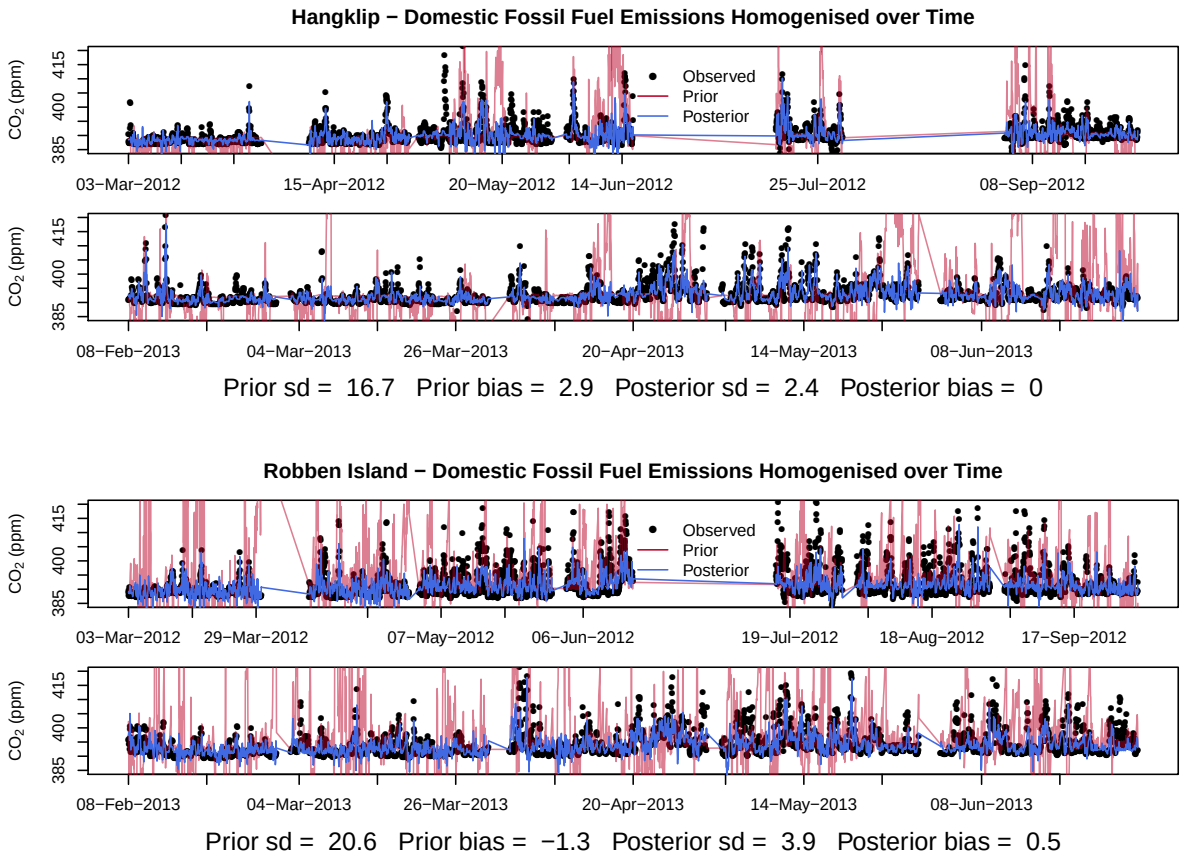

Figure S21. Prior and posterior modelled concentrations at Hangklip and Robben Island sites when the temporally homogenised domestic fossil fuel fluxes prior was used S11 over the full inversion period from March 2012 until June 2013.

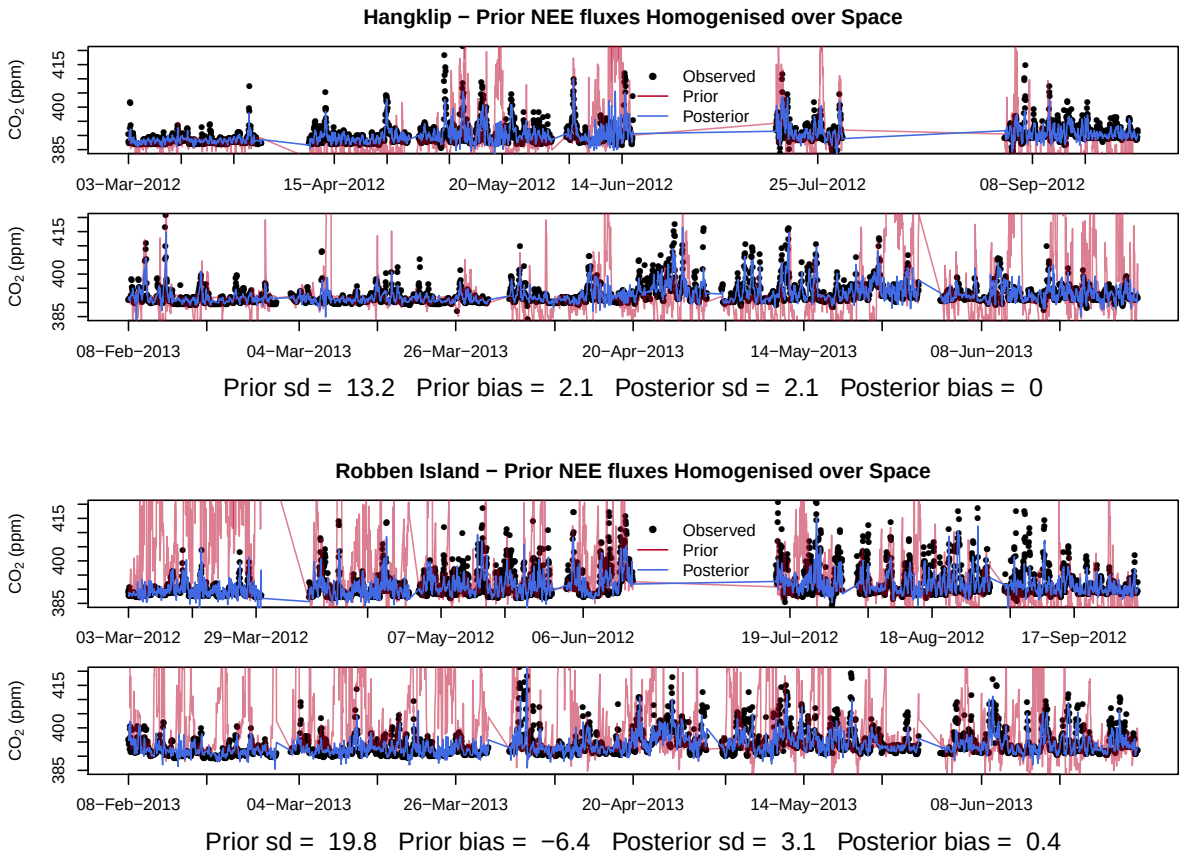

Figure S22. Prior and posterior modelled concentrations at Hangklip and Robben Island sites when the spatially homogenised NEE fluxes prior was used S12 over the full inversion period from March 2012 until June 2013.

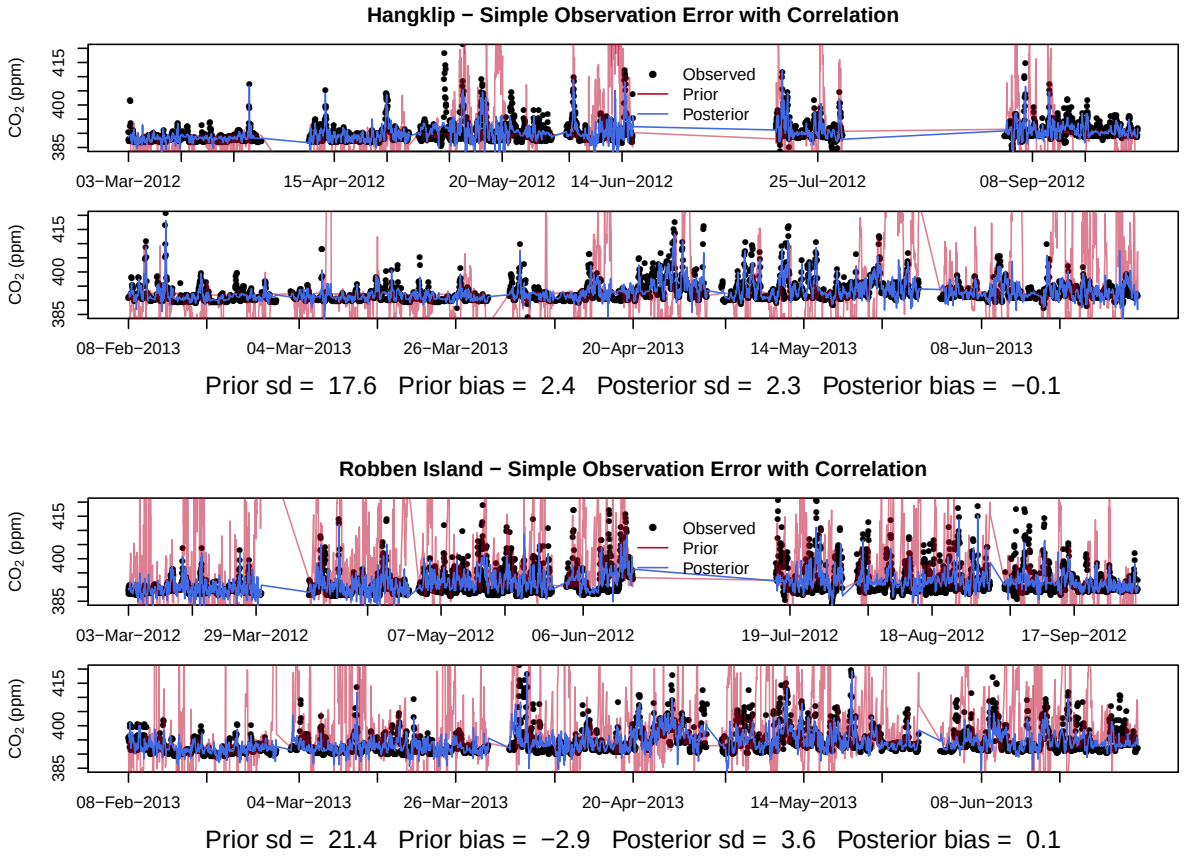

Figure S23. Prior and posterior modelled concentrations at Hangklip and Robben Island sites under the inversion where uncertainties in the observation errors were estimated to be 2 ppm during the day and 4 ppm at night S13 over the full inversion period from March 2012 until June 2013.

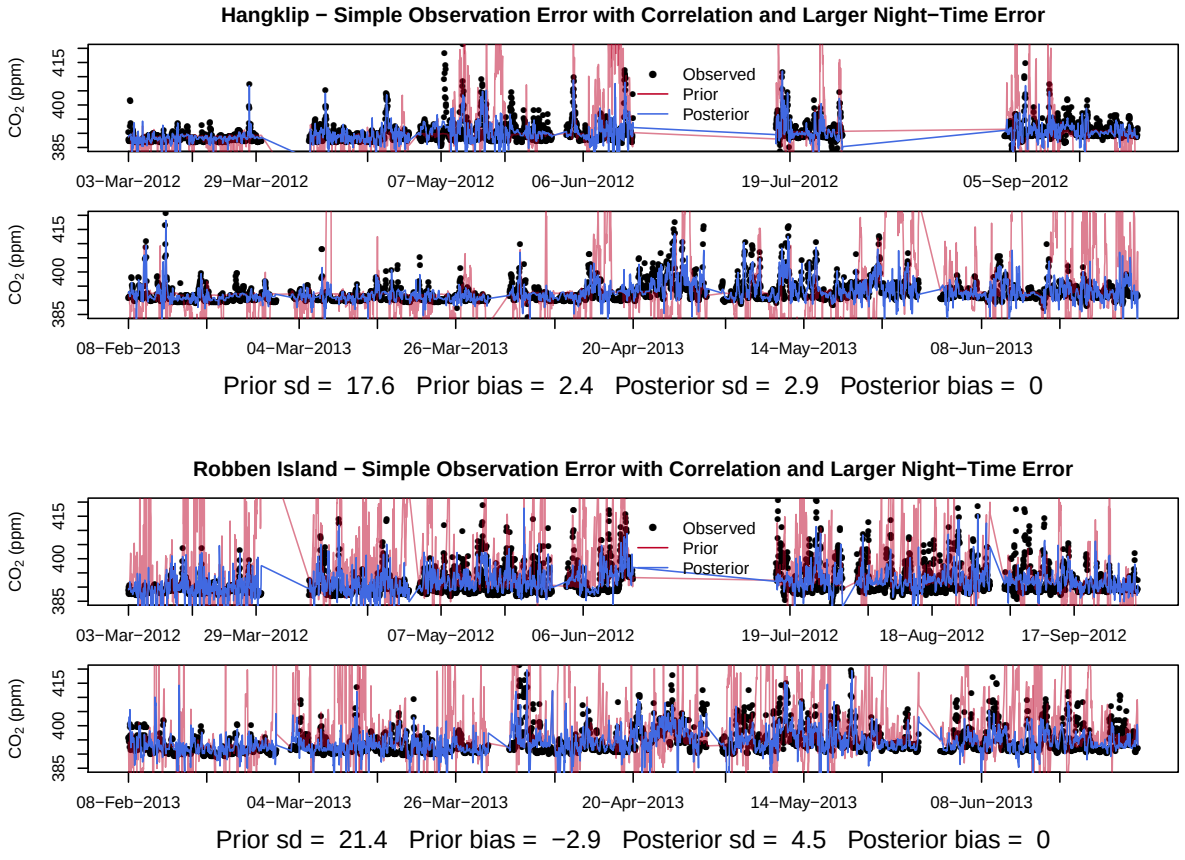

Figure S24. Prior and posterior modelled concentrations at Hangklip and Robben Island sites under the inversion where uncertainties in the observation errors were estimated to be 2 ppm during the day and 10 ppm at night S14 over the full inversion period from March 2012 until June 2013.

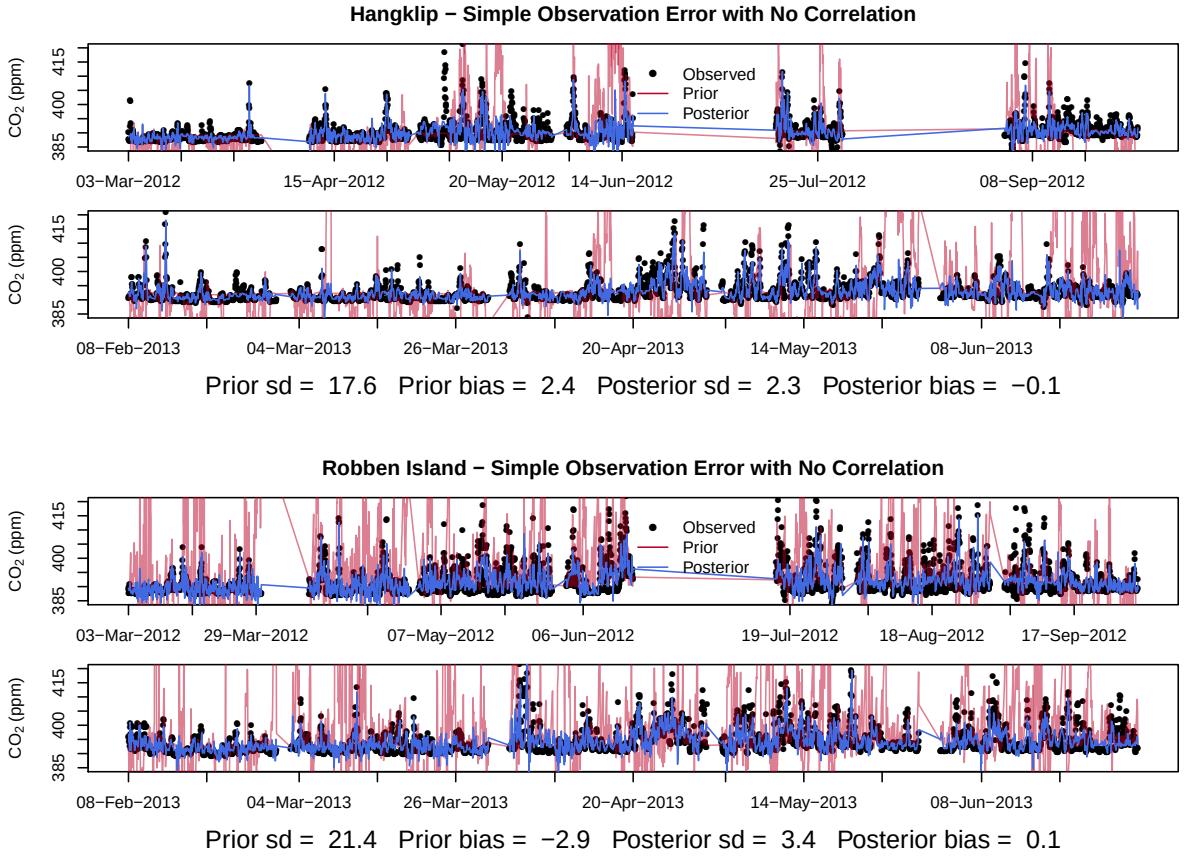

Figure S25. Prior and posterior modelled concentrations at Hangklip and Robben Island sites under the inversion where uncertainties in the observation errors were estimated to be 2 ppm during the day and 4 ppm at night, and no correlation was specified between the observation errors S15, over the full inversion period from March 2012 until June 2013.

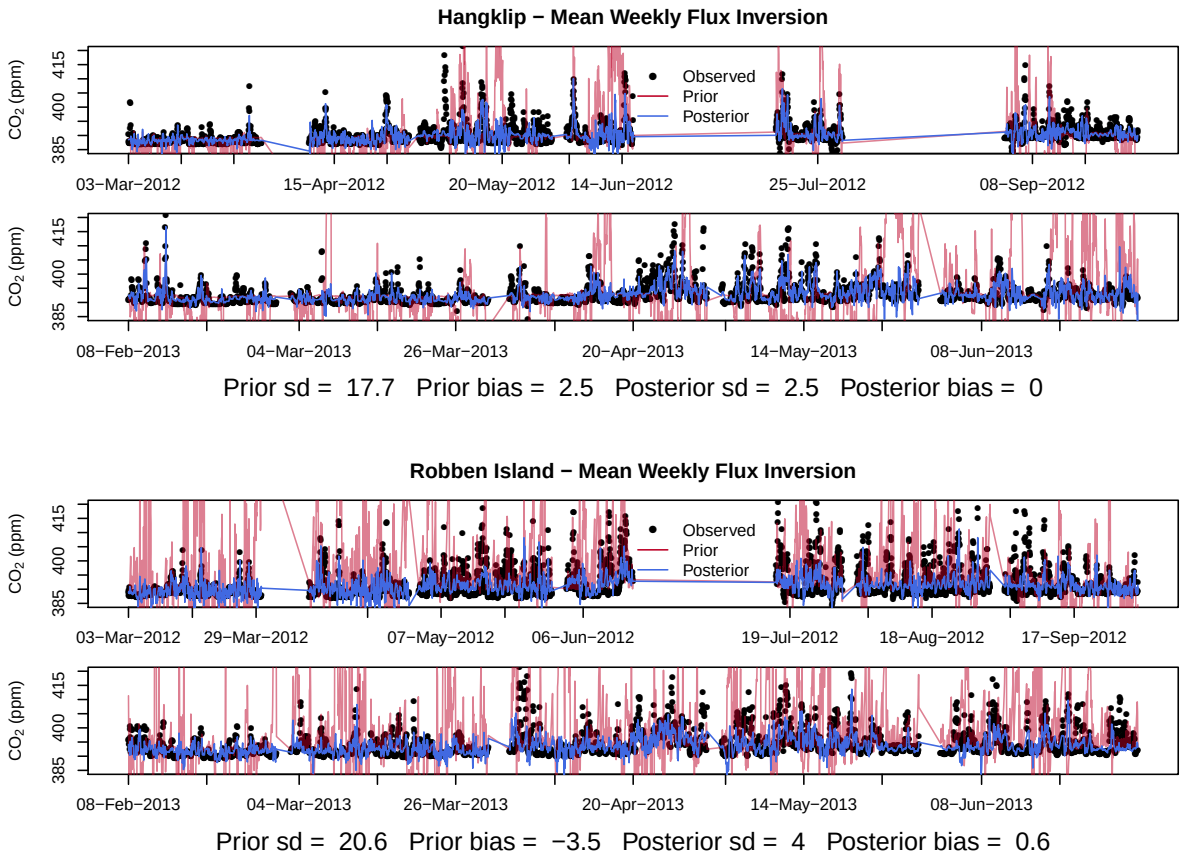

Figure S26. Prior and posterior modelled concentrations at Hangklip and Robben Island sites under the inversion which solved for the mean weekly flux S16 over the full inversion period from March 2012 until June 2013.

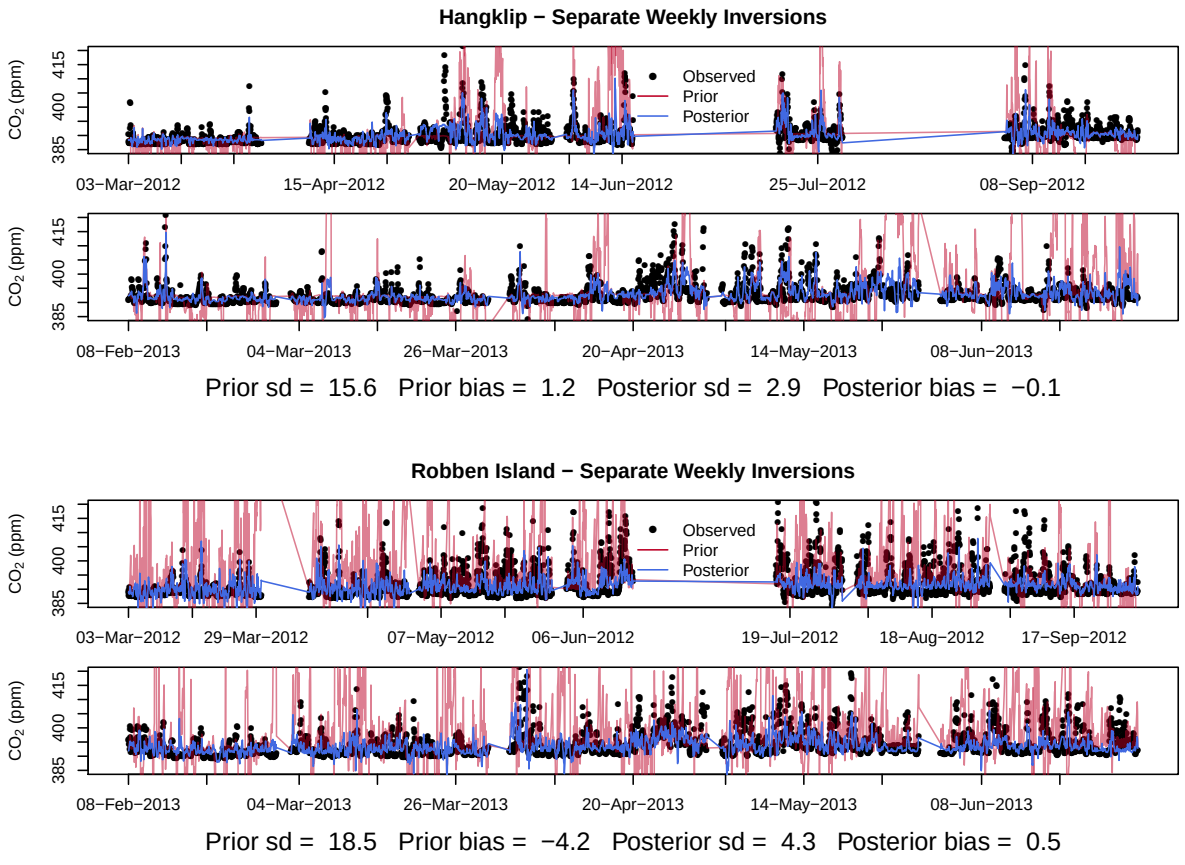

Figure S27. Prior and posterior modelled concentrations at Hangklip and Robben Island sites under separate weekly inversions S17 over the full inversion period from March 2012 until June 2013.

1.4 Modelled Contributions to the Concentration from Fossil Fuel and NEE

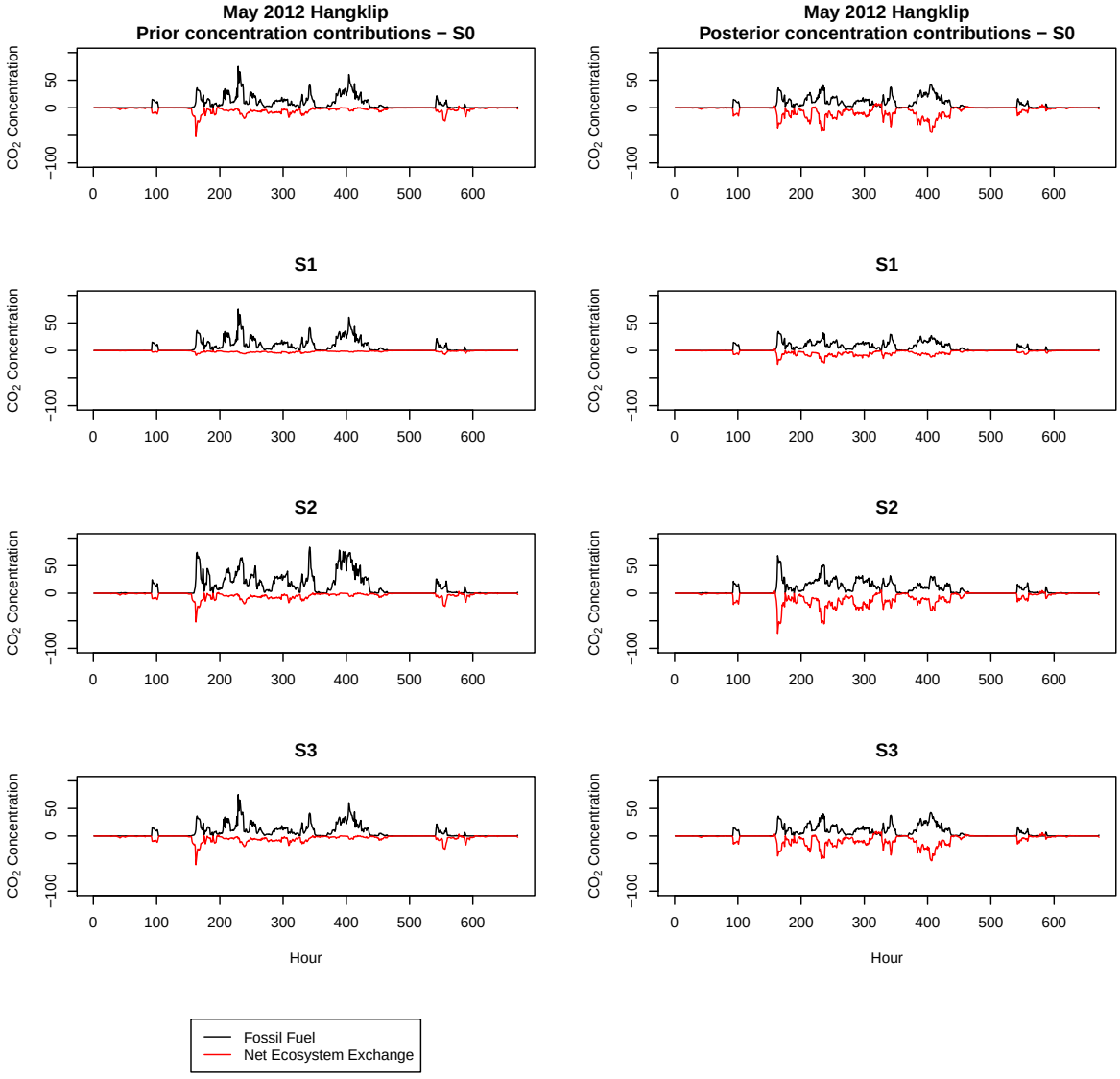

Figure S28. Prior and posterior modelled contributions to the concentration during May 2012 from fossil fuel and NEE fluxes for the inversions S0 to S3 at the Hangklip site.

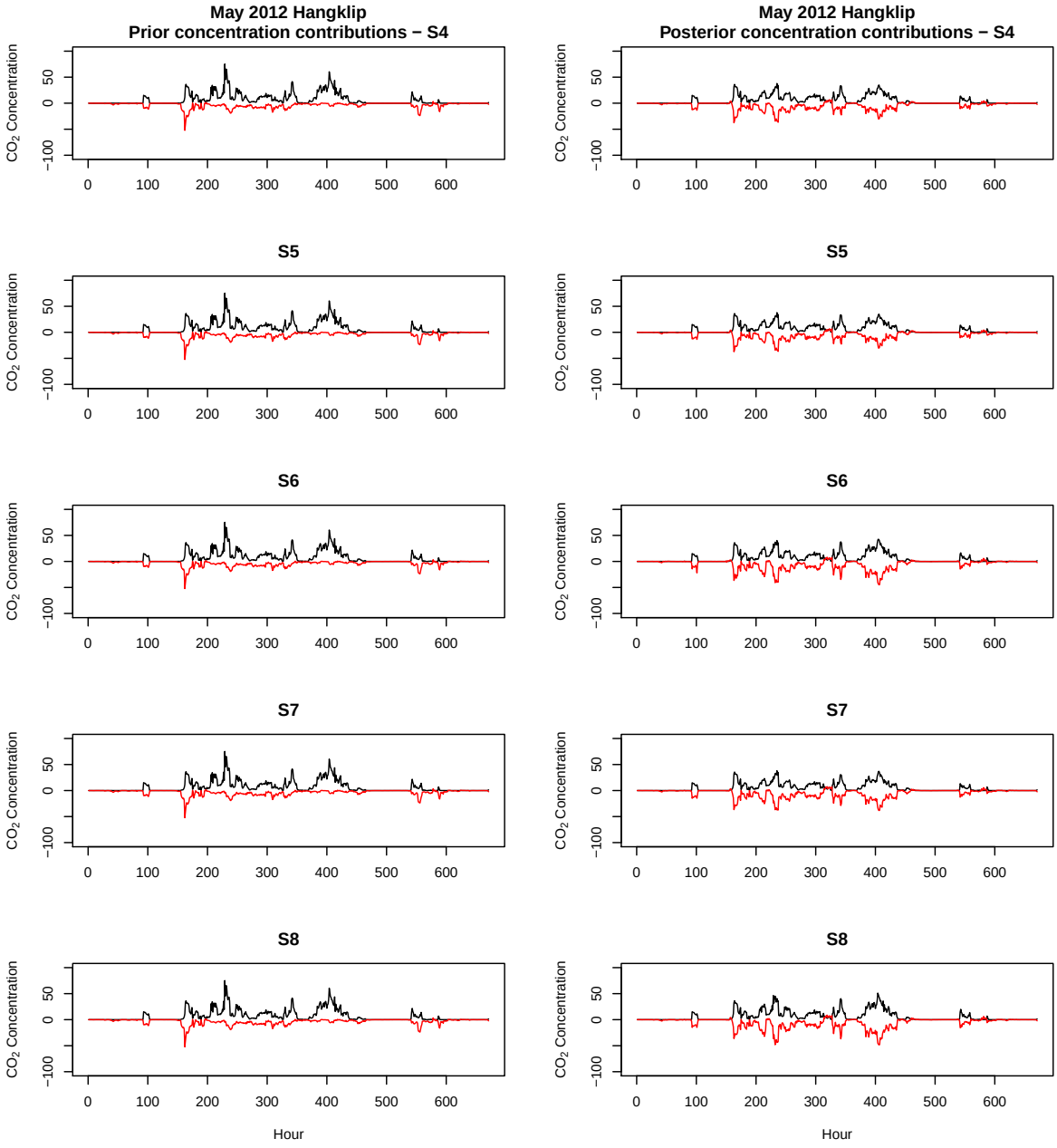

Figure S29. Prior and posterior modelled contributions to the concentration during May 2012 from fossil fuel and NEE fluxes for the inversions S4 to S8 at the Hangklip site.

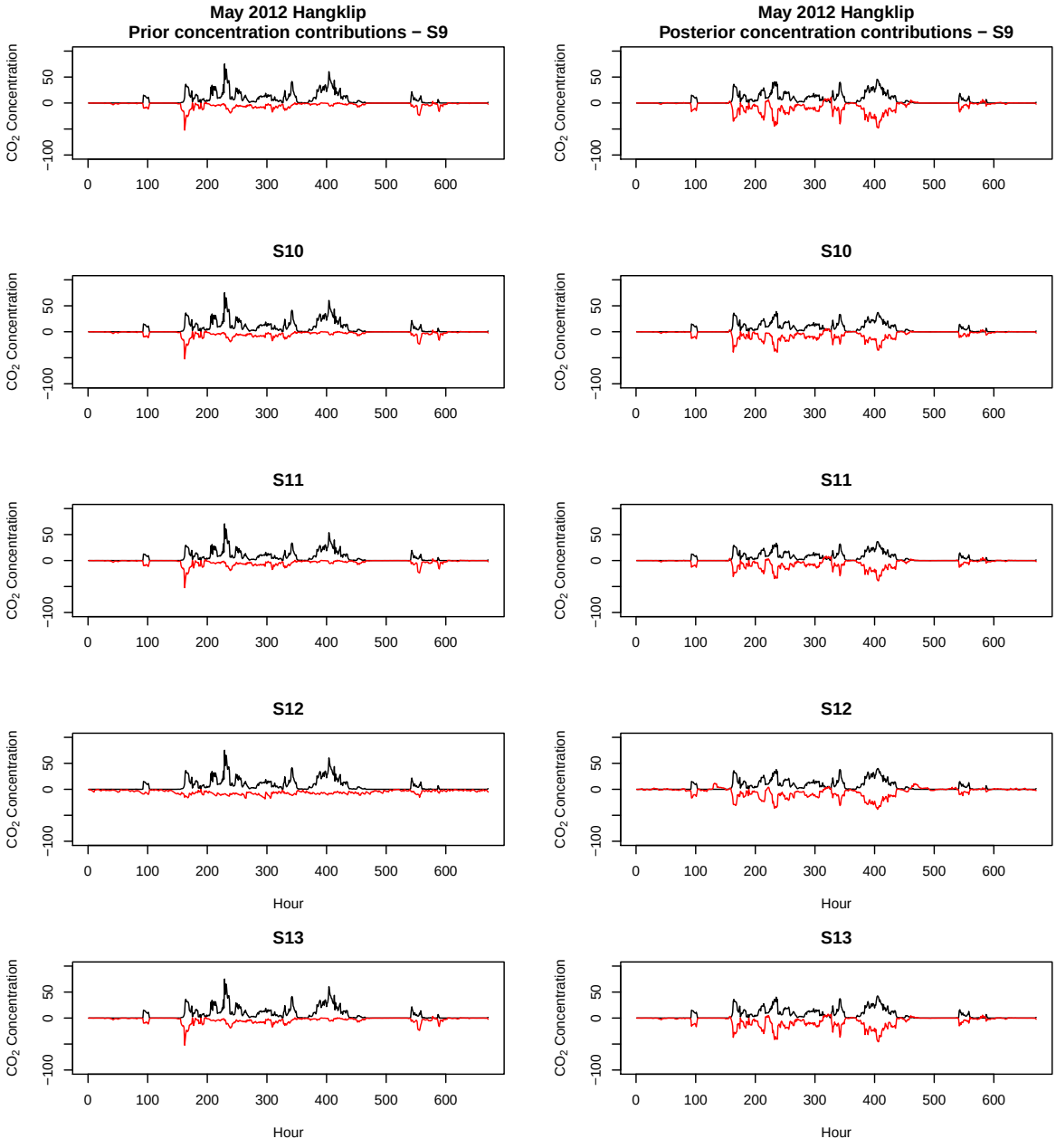

Figure S30. Prior and posterior modelled contributions to the concentration during May 2012 from fossil fuel and NEE fluxes for the inversions S9 to S13 at the Hangklip site.

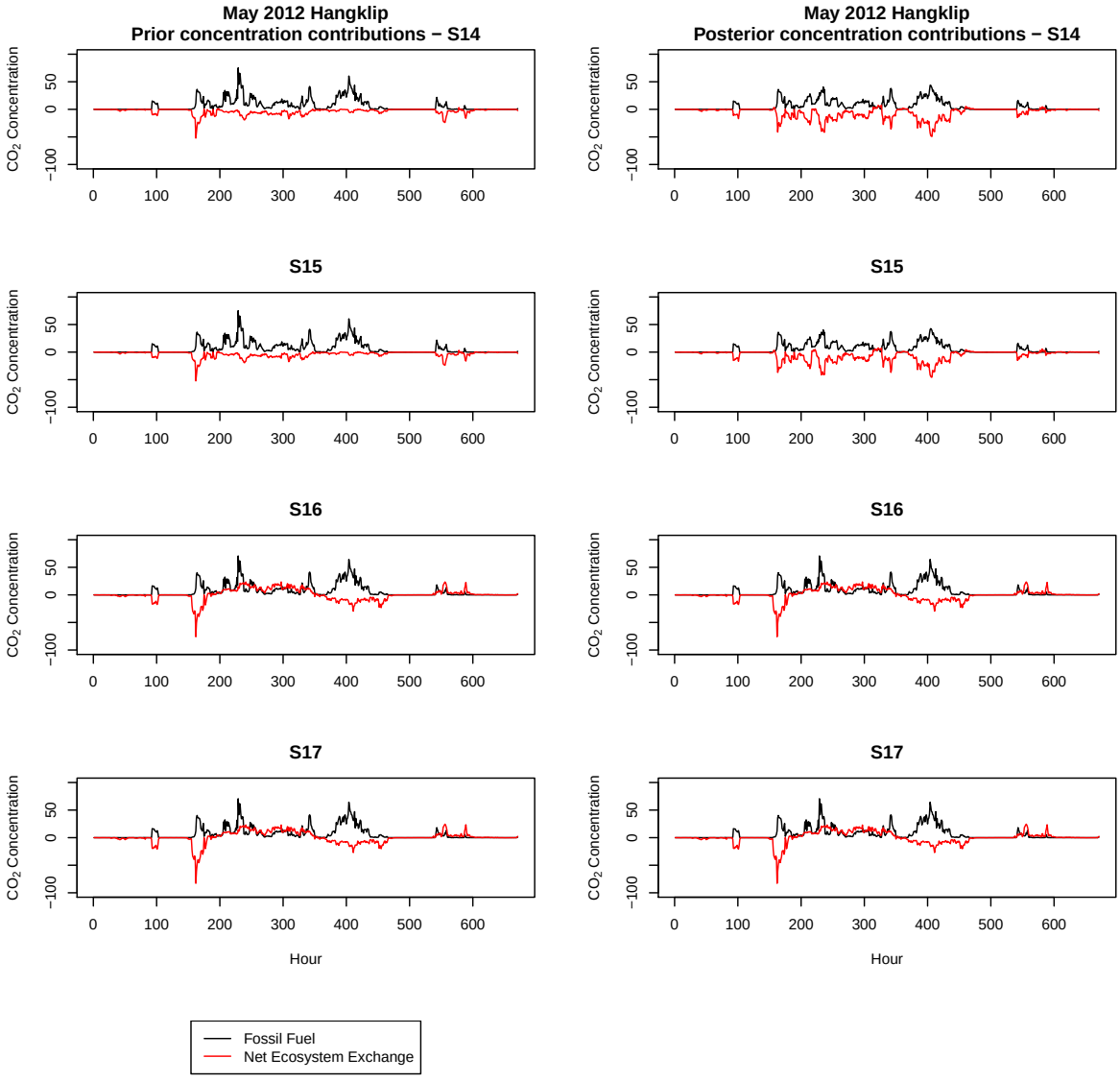

Figure S31. Prior and posterior modelled contributions to the concentration during May 2012 from fossil fuel and NEE fluxes for the inversions S14 to S17 at the Hangklip site.

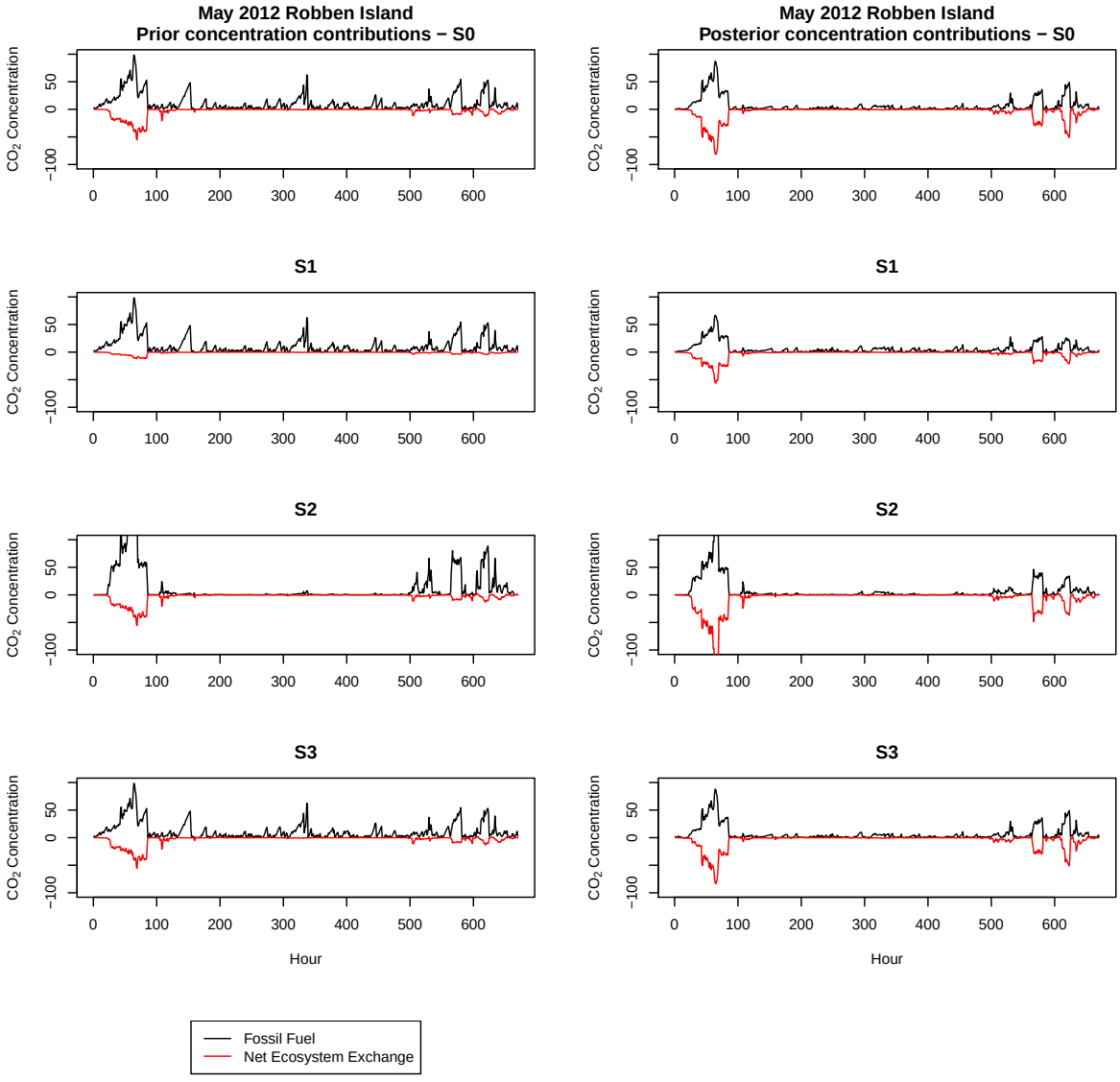

Figure S32. Prior and posterior modelled contributions to the concentration during May 2012 from fossil fuel and NEE fluxes for the inversions S0 to S3 at the Robben Island site.

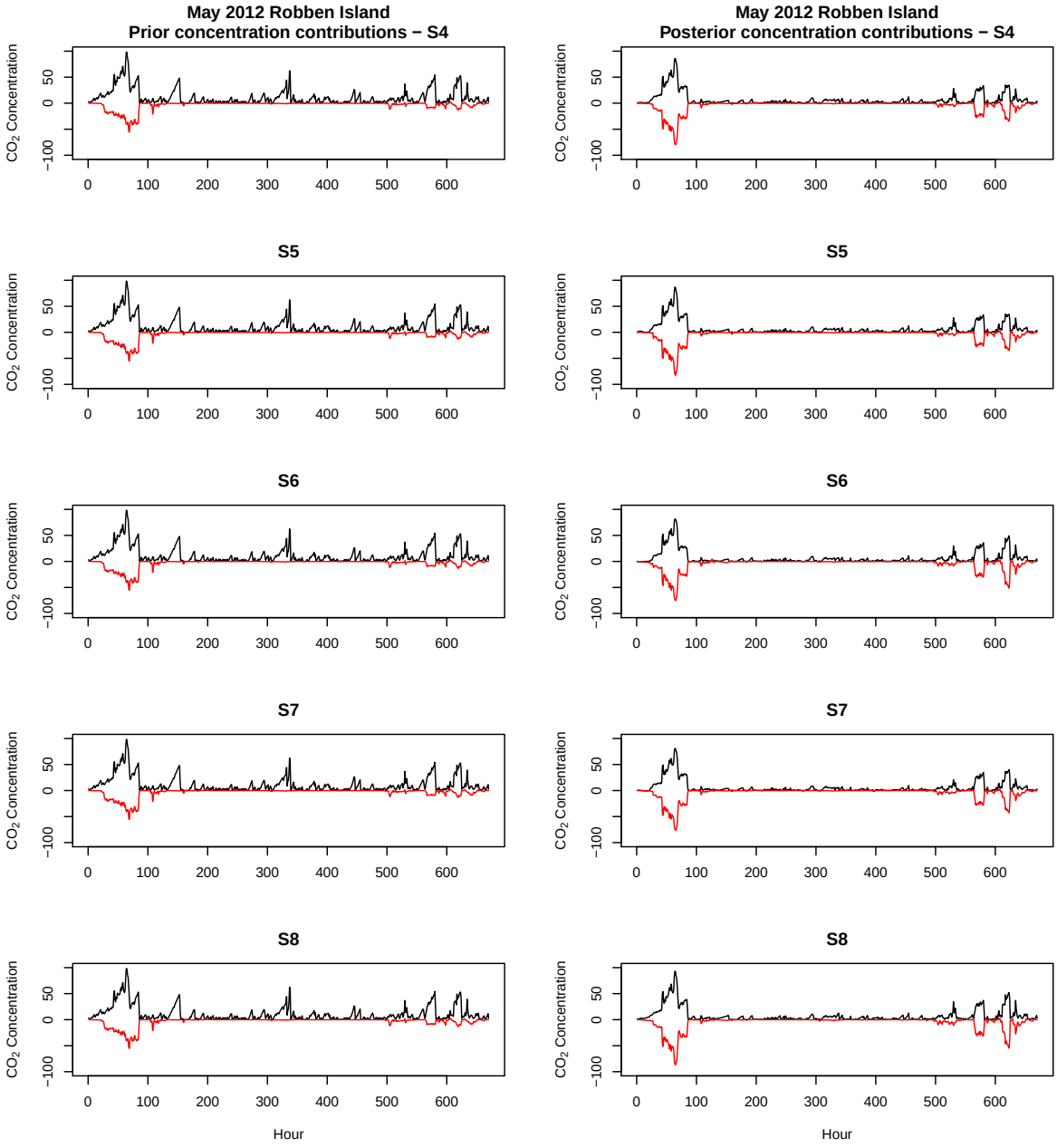

Figure S33. Prior and posterior modelled contributions to the concentration during May 2012 from fossil fuel and NEE fluxes for the inversions S4 to S8 at the Robben Island site.

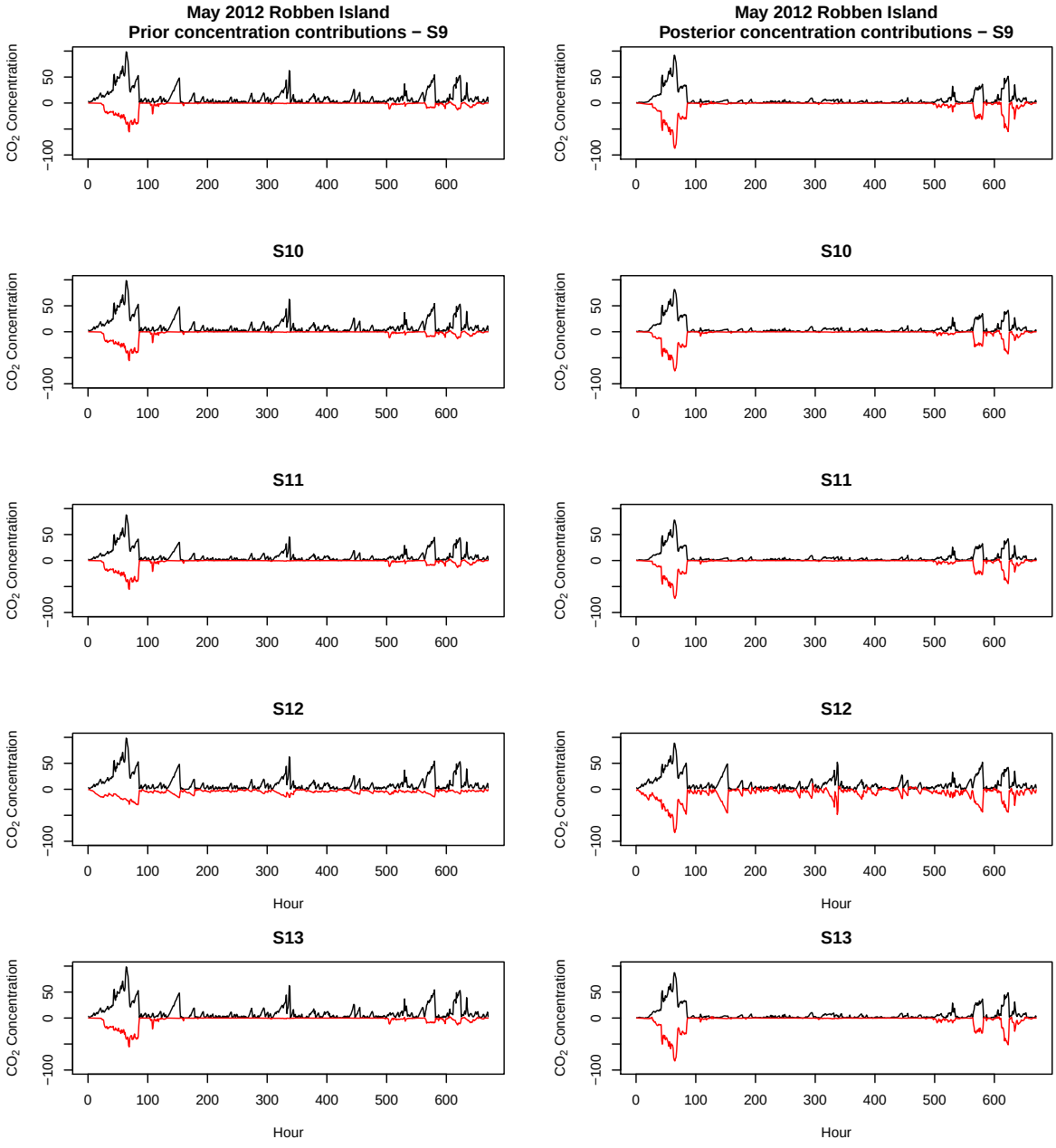

Figure S34. Prior and posterior modelled contributions to the concentration during May 2012 from fossil fuel and NEE fluxes for the inversions S9 to S13 at the Robben Island site.

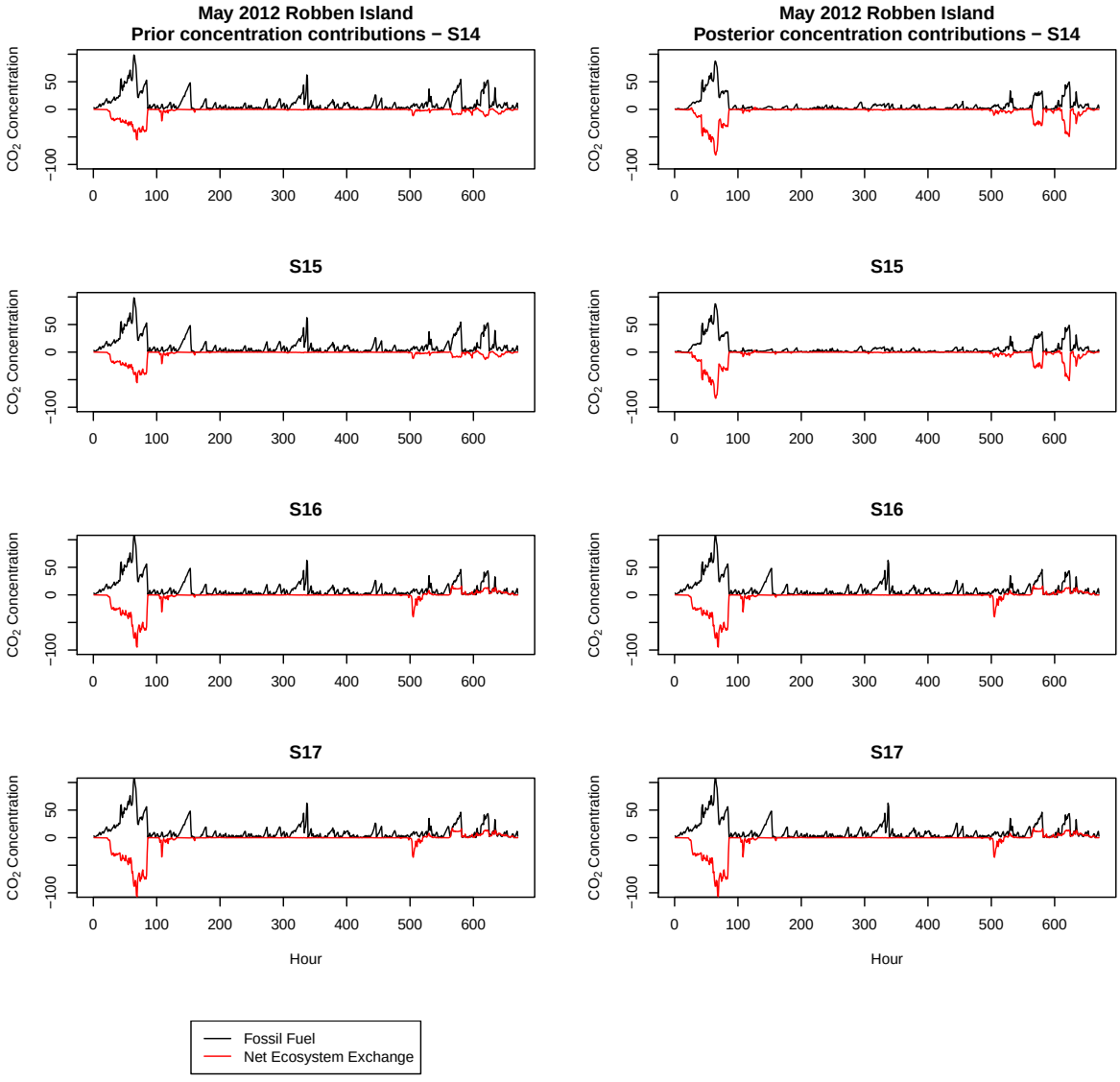

Figure S35. Prior and posterior modelled contributions to the concentration during May 2012 from fossil fuel and NEE fluxes for the inversions S14 to S17 at the Robben Island site.

1.5 Diurnal Concentration Plots

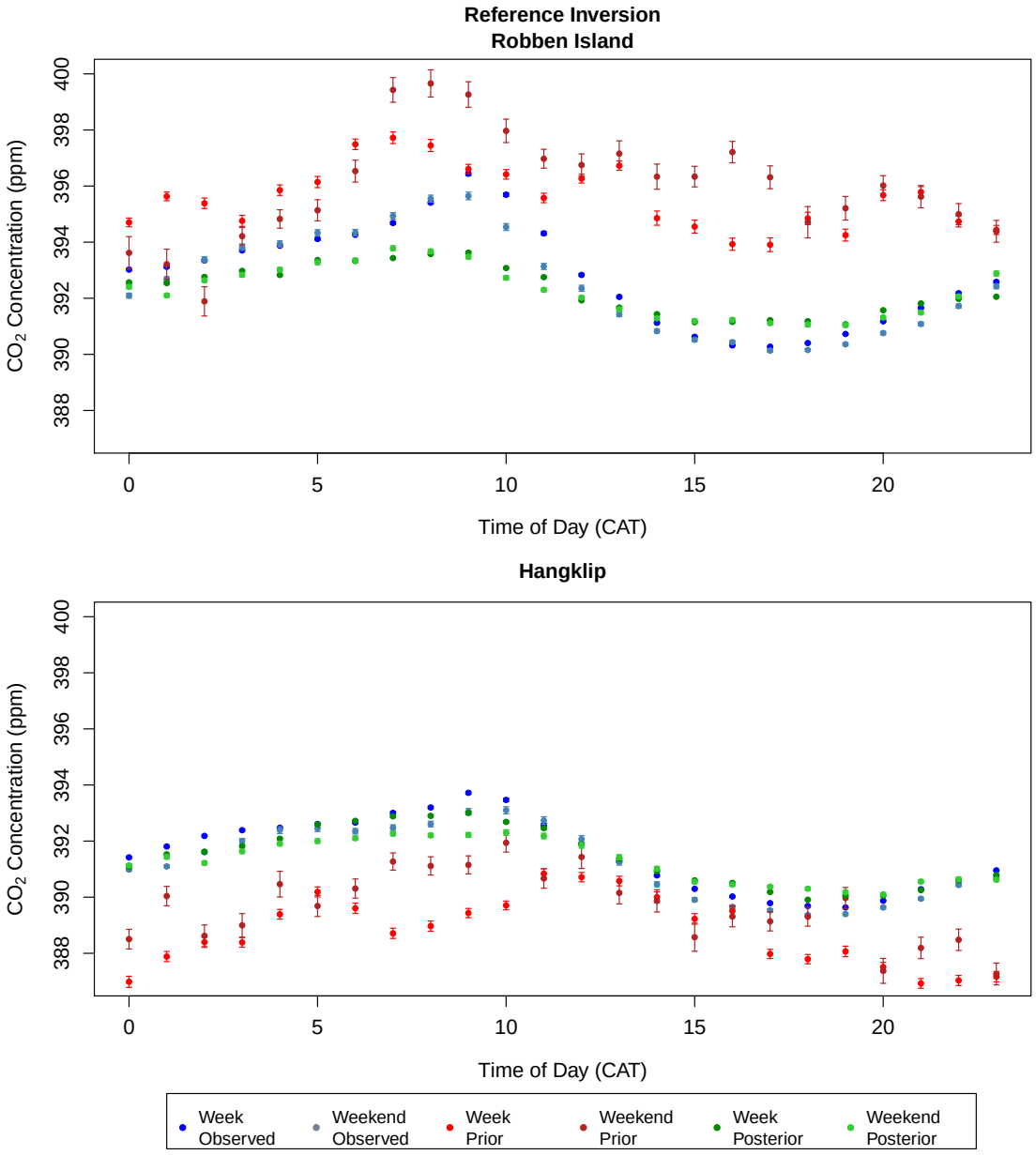

Figure S36. The hourly diurnal cycle (mean concentrations for each hour with 95% confidence interval) in the observed, prior and posterior modelled CO_2 concentrations (ppm) over the full measurement period from March 2012 until June 2013, separated by working week and weekend, and plotted separately for Robben Island (top) and Hangklip (bottom) measurement sites for the reference inversion S0. The diurnal plots are separated into working week and weekend observed concentrations (blue and light blue), working week and weekend prior modelled concentrations (red and dark red), and working week and weekend posterior modelled concentrations (green and light green).

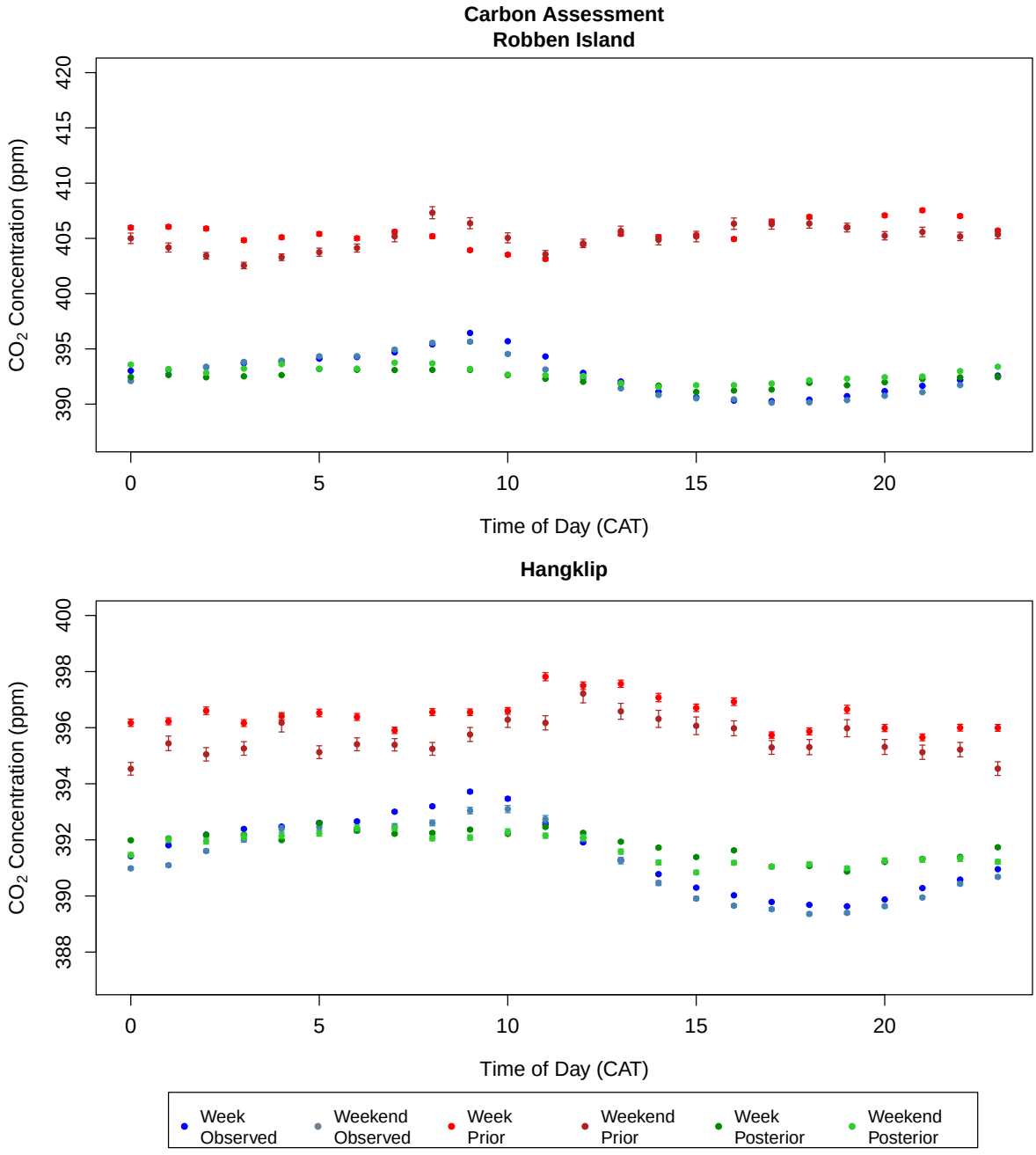

Figure S37. The hourly diurnal cycle (mean concentrations for each hour with 95% confidence interval) in the observed, prior and posterior modelled CO_2 concentrations (ppm) over the full measurement period from March 2012 until June 2013, separated by working week and weekend, and plotted separately for Robben Island (top) and Hangklip (bottom) measurement sites for the inversion using the carbon assessment product for the NEE prior flux estimates S1. The diurnal plots are separated into working week and weekend observed concentrations (blue and light blue), working week and weekend prior modelled concentrations (red and dark red), and working week and weekend posterior modelled concentrations (green and light green).

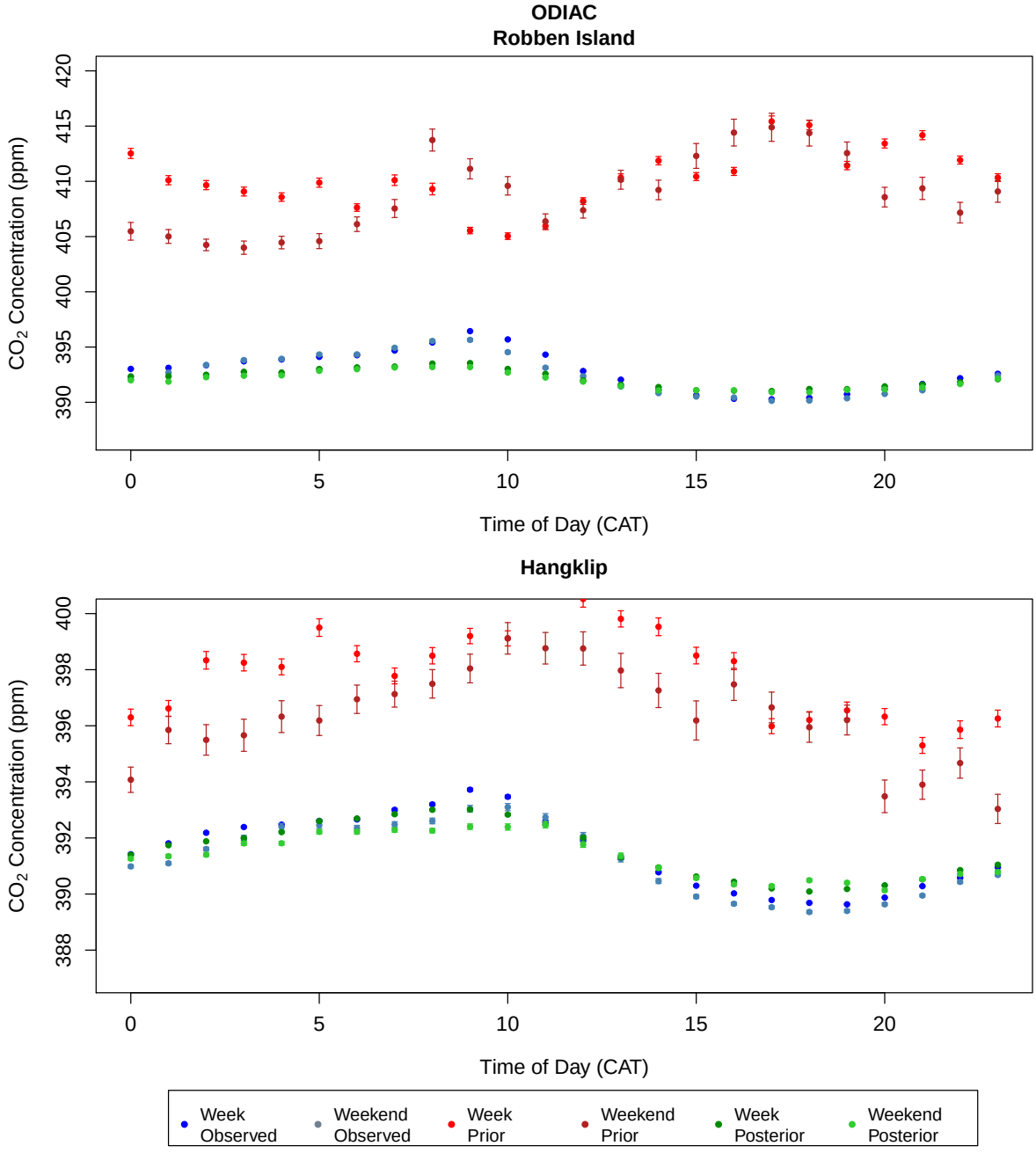

Figure S38. The hourly diurnal cycle (mean concentrations for each hour with 95% confidence interval) in the observed, prior and posterior modelled CO_2 concentrations (ppm) over the full measurement period from March 2012 until June 2013, separated by working week and weekend, and plotted separately for Robben Island (top) and Hangklip (bottom) measurement sites for the inversion using the ODIAC product for the fossil fuel flux prior estimates S2. The diurnal plots are separated into working week and weekend observed concentrations (blue and light blue), working week and weekend prior modelled concentrations (red and dark red), and working week and weekend posterior modelled concentrations (green and light green).

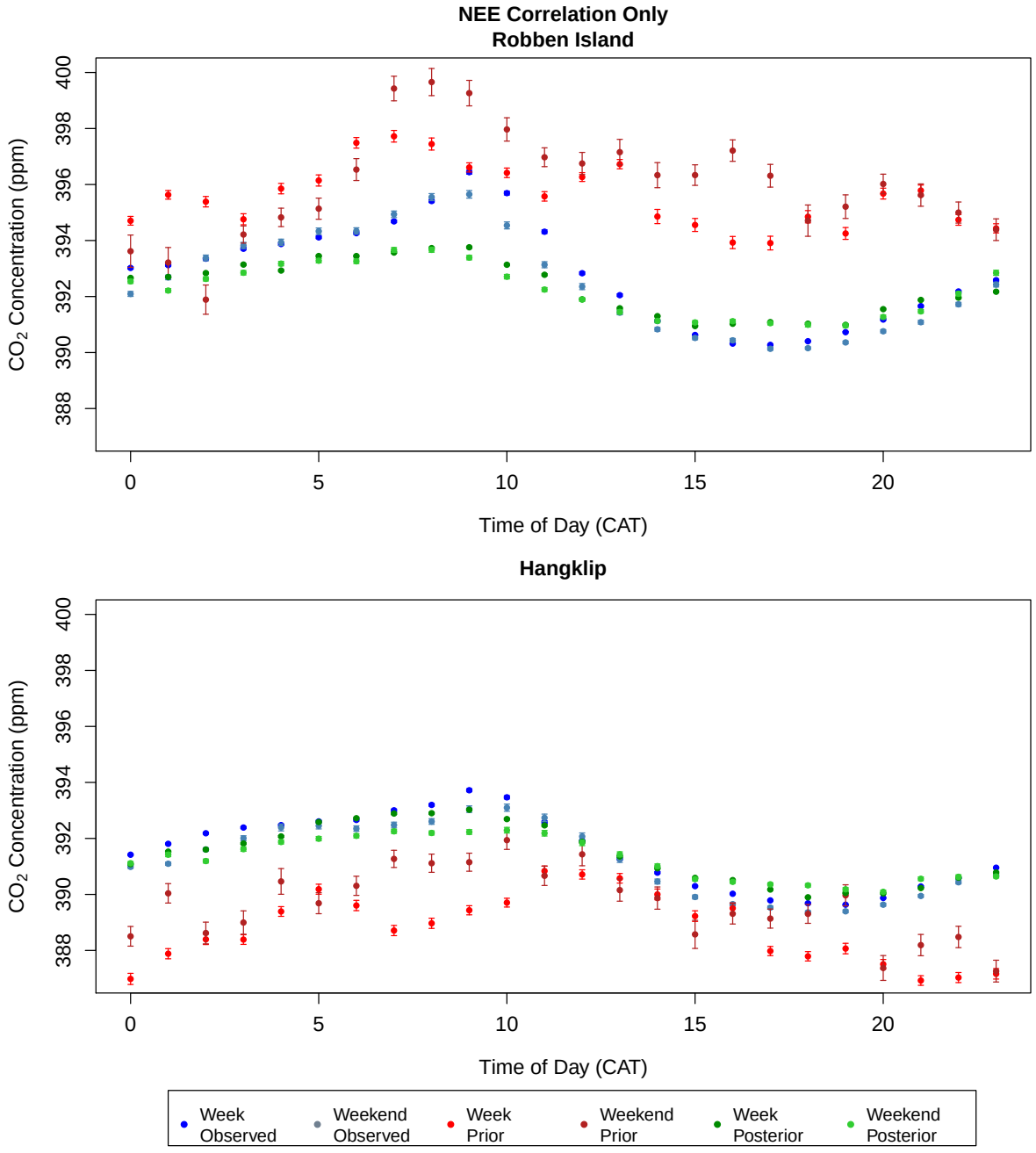

Figure S39. The hourly diurnal cycle (mean concentrations for each hour with 95% confidence interval) in the observed, prior and posterior modelled CO_2 concentrations (ppm) over the full measurement period from March 2012 until June 2013, separated by working week and weekend, and plotted separately for Robben Island (top) and Hangklip (bottom) measurement sites for the inversion accounting for only correlation between the NEE flux uncertainties S3. The diurnal plots are separated into working week and weekend observed concentrations (blue and light blue), working week and weekend prior modelled concentrations (red and dark red), and working week and weekend posterior modelled concentrations (green and light green).

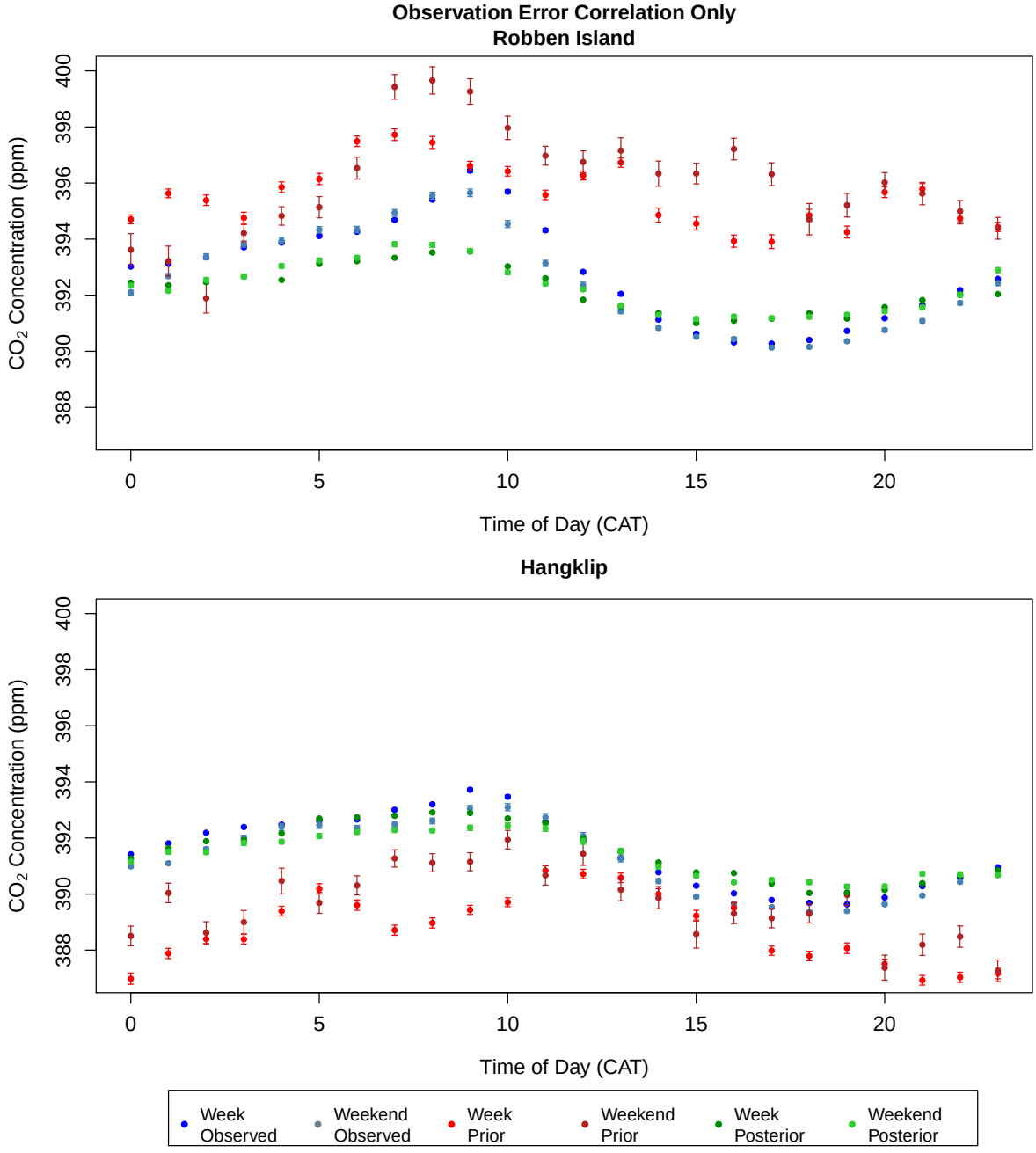

Figure S40. The hourly diurnal cycle (mean concentrations for each hour with 95% confidence interval) in the observed, prior and posterior modelled CO_2 concentrations (ppm) over the full measurement period from March 2012 until June 2013, separated by working week and weekend, and plotted separately for Robben Island (top) and Hangklip (bottom) measurement sites for the inversion accounting for only correlation between the observation errors with no correlation specified between the NEE flux uncertainties S4. The diurnal plots are separated into working week and weekend observed concentrations (blue and light blue), working week and weekend prior modelled concentrations (red and dark red), and working week and weekend posterior modelled concentrations (green and light green).

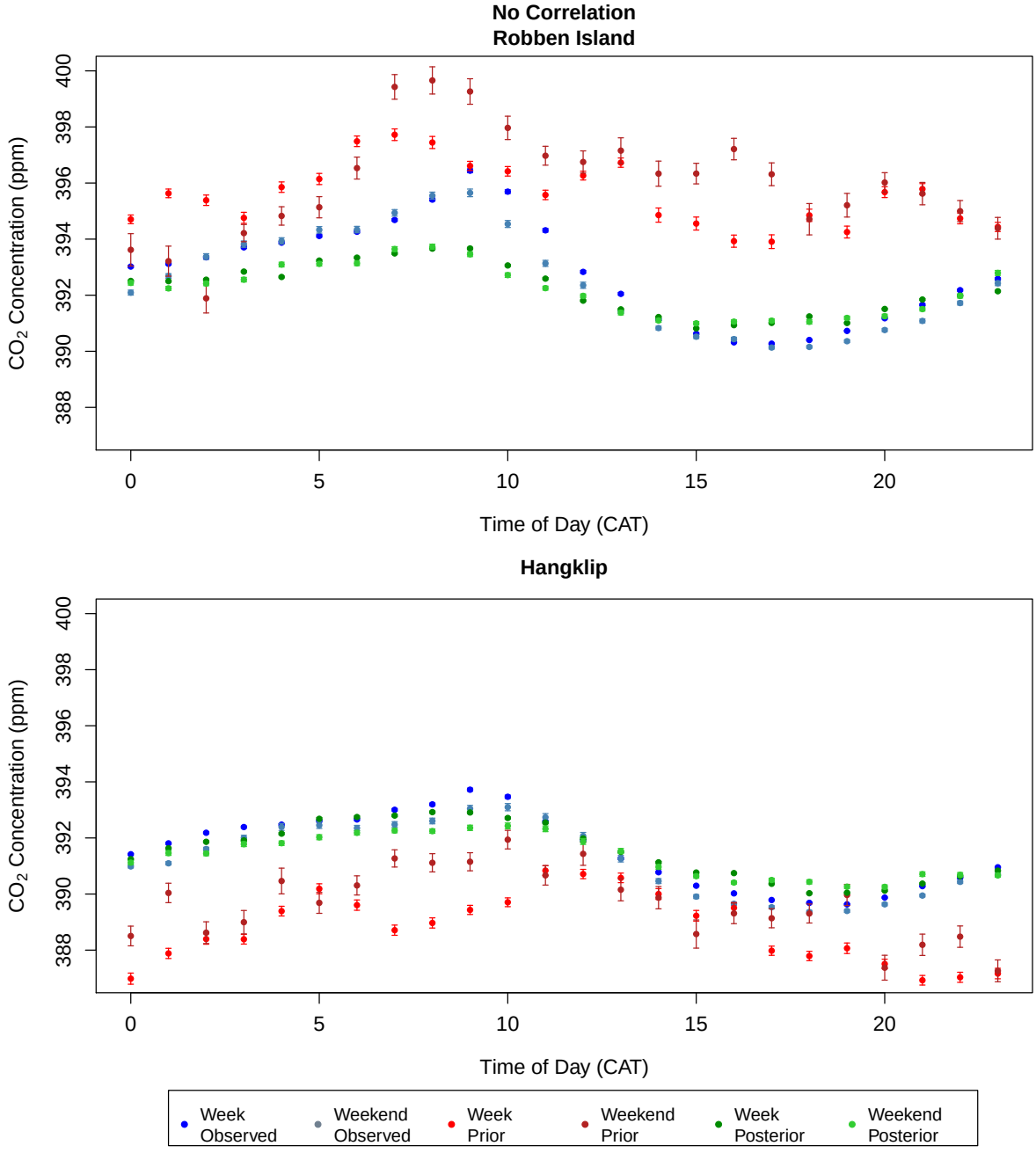

Figure S41. The hourly diurnal cycle (mean concentrations for each hour with 95% confidence interval) in the observed, prior and posterior modelled CO_2 concentrations (ppm) over the full measurement period from March 2012 until June 2013, separated by working week and weekend, and plotted separately for Robben Island (top) and Hangklip (bottom) measurement sites for the inversion specifying no correlation between the observation errors and no correlation between the NEE flux uncertainties S5. The diurnal plots are separated into working week and weekend observed concentrations (blue and light blue), working week and weekend prior modelled concentrations (red and dark red), and working week and weekend posterior modelled concentrations (green and light green).

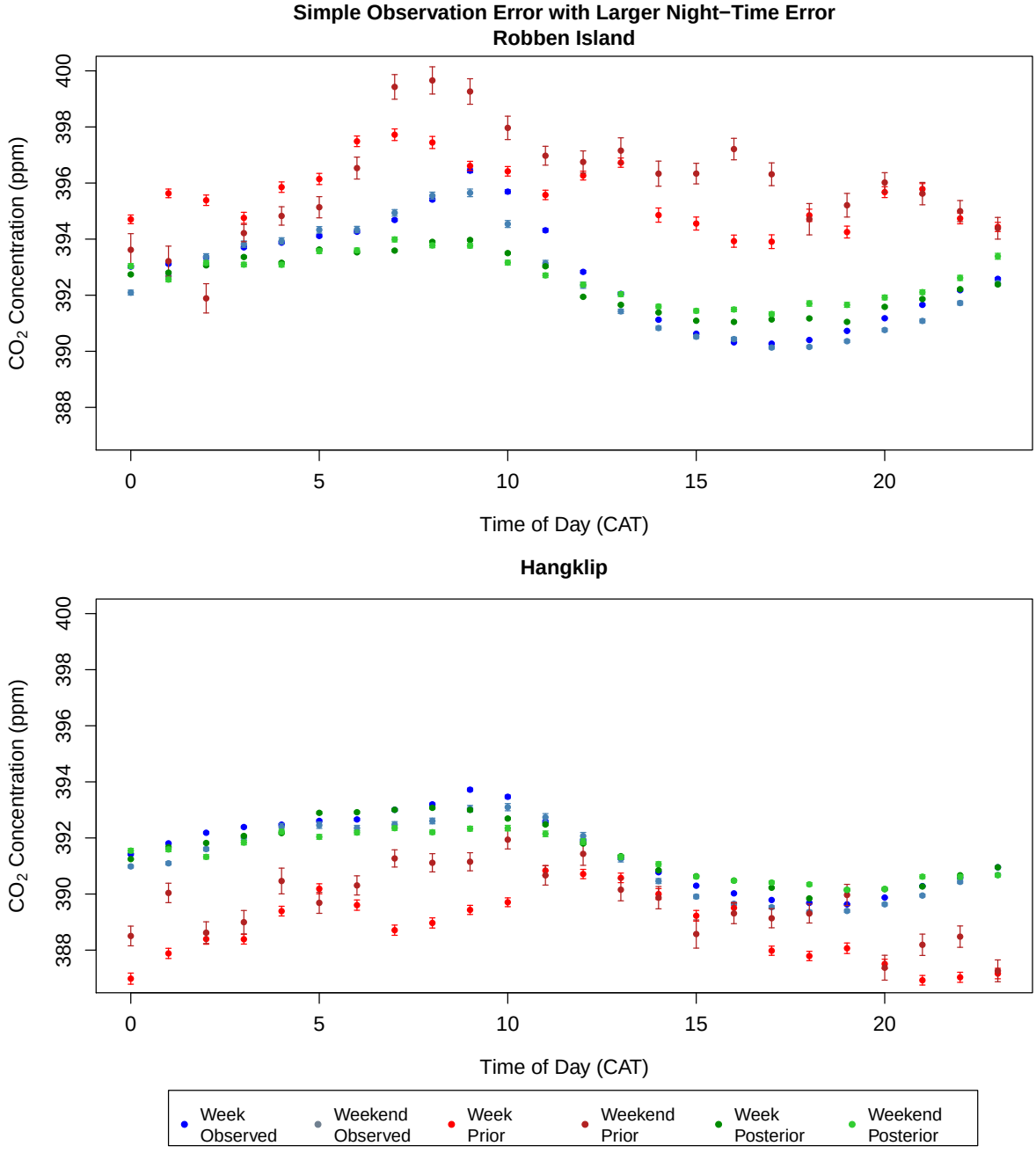

Figure S42. The hourly diurnal cycle (mean concentrations for each hour with 95% confidence interval) in the observed, prior and posterior modelled CO_2 concentrations (ppm) over the full measurement period from March 2012 until June 2013, separated by working week and weekend, and plotted separately for Robben Island (top) and Hangklip (bottom) measurement sites for the inversion assigning a seven hour correlation length to the observation errors S6. The diurnal plots are separated into working week and weekend observed concentrations (blue and light blue), working week and weekend prior modelled concentrations (red and dark red), and working week and weekend posterior modelled concentrations (green and light green).

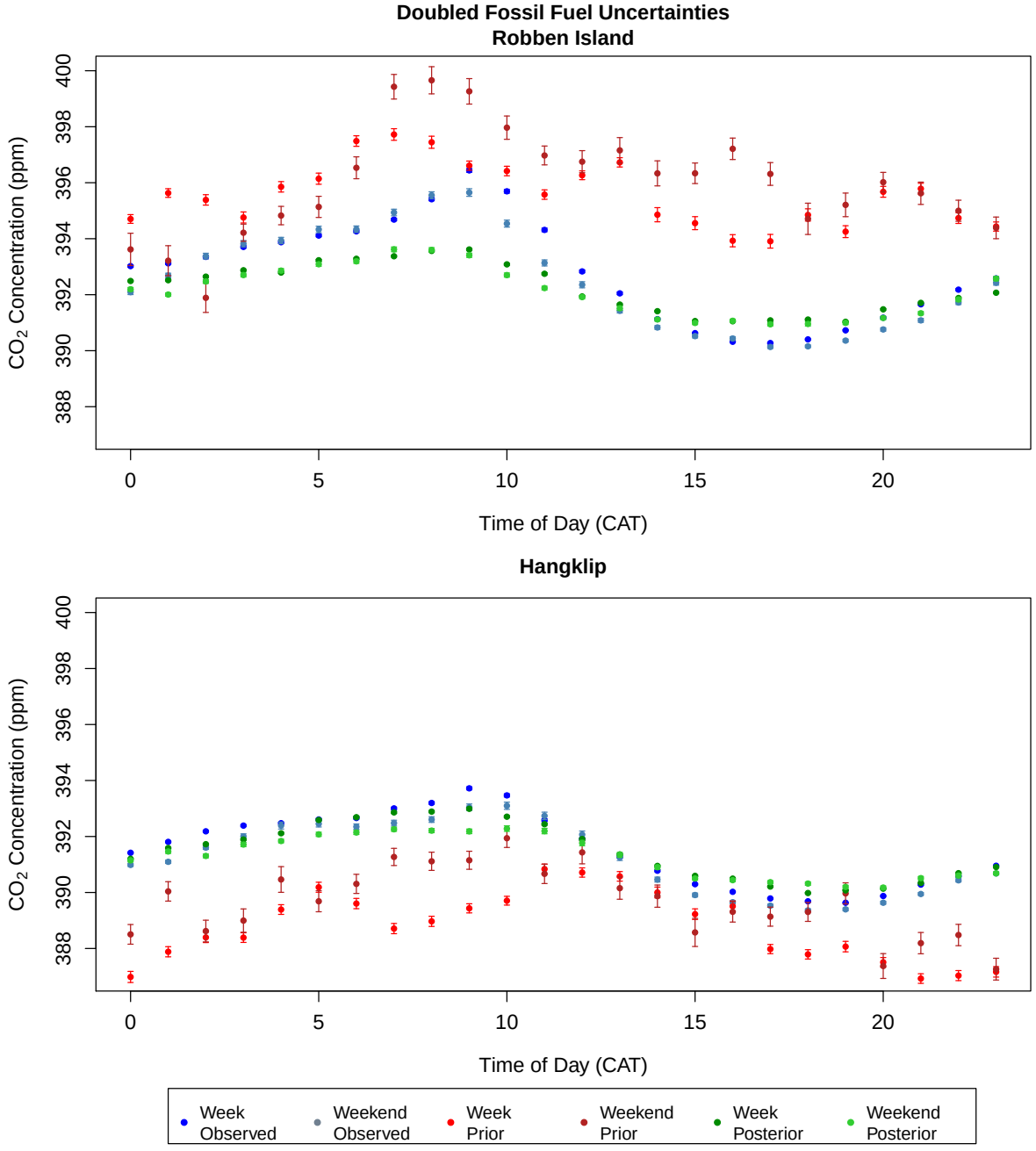

Figure S43. The hourly diurnal cycle (mean concentrations for each hour with 95% confidence interval) in the observed, prior and posterior modelled CO_2 concentrations (ppm) over the full measurement period from March 2012 until June 2013, separated by working week and weekend, and plotted separately for Robben Island (top) and Hangklip (bottom) measurement sites for the inversion with doubled fossil fuel flux uncertainties S7. The diurnal plots are separated into working week and weekend observed concentrations (blue and light blue), working week and weekend prior modelled concentrations (red and dark red), and working week and weekend posterior modelled concentrations (green and light green).

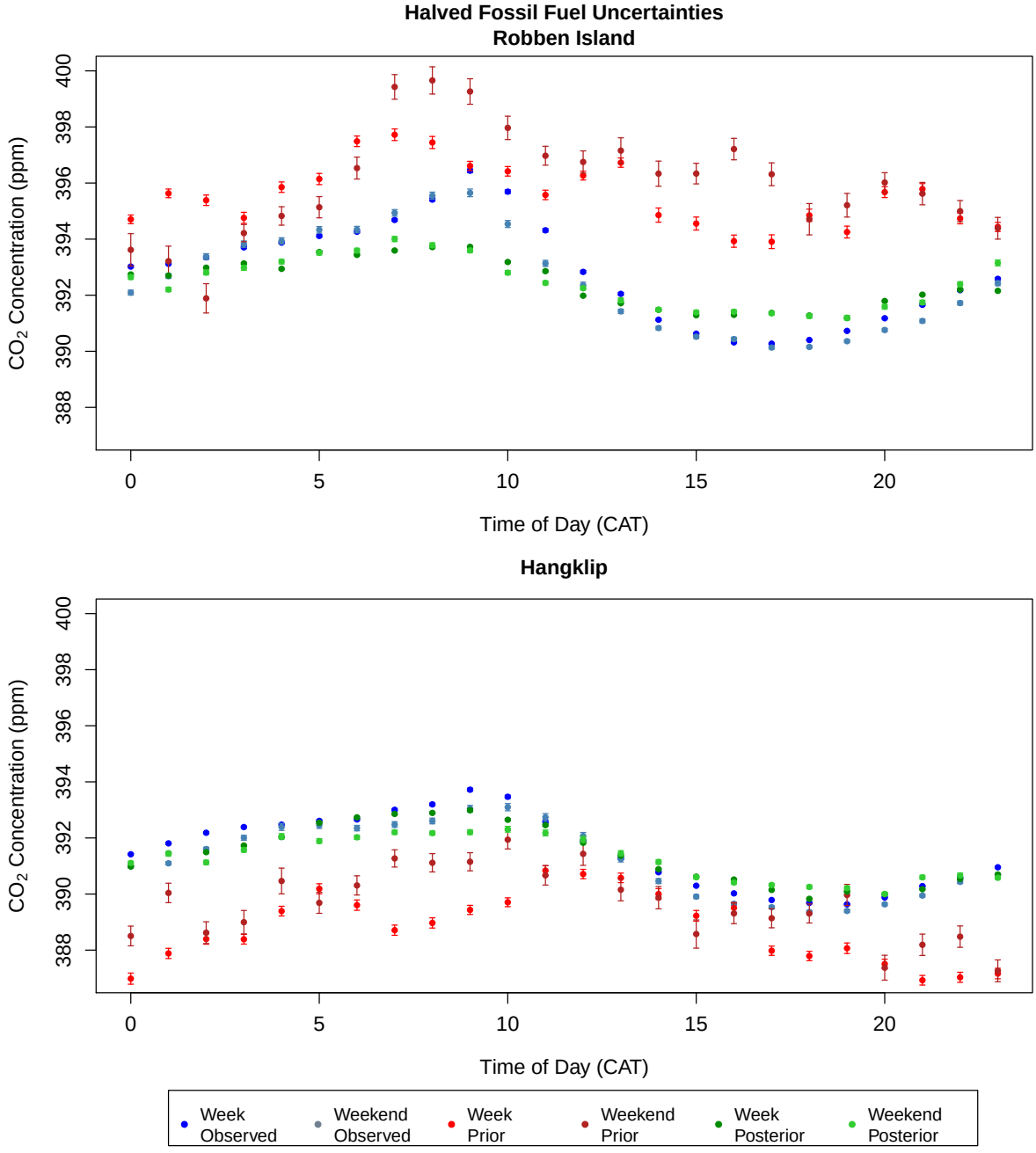

Figure S44. The hourly diurnal cycle (mean concentrations for each hour with 95% confidence interval) in the observed, prior and posterior modelled CO_2 concentrations (ppm) over the full measurement period from March 2012 until June 2013, separated by working week and weekend, and plotted separately for Robben Island (top) and Hangklip (bottom) measurement sites for the inversion with halved fossil fuel flux uncertainties S8. The diurnal plots are separated into working week and weekend observed concentrations (blue and light blue), working week and weekend prior modelled concentrations (red and dark red), and working week and weekend posterior modelled concentrations (green and light green).

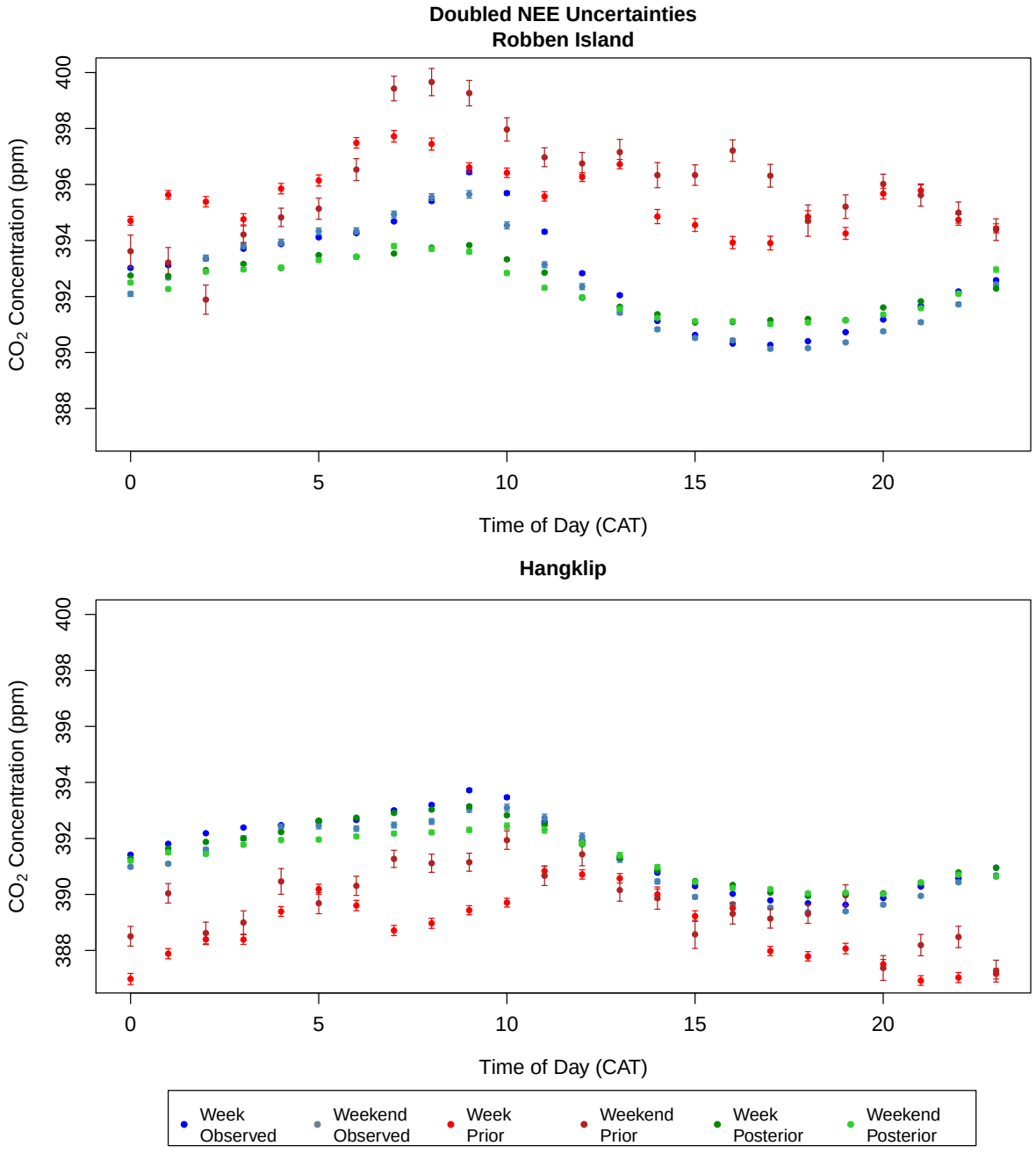

Figure S45. The hourly diurnal cycle (mean concentrations for each hour with 95% confidence interval) in the observed, prior and posterior modelled CO_2 concentrations (ppm) over the full measurement period from March 2012 until June 2013, separated by working week and weekend, and plotted separately for Robben Island (top) and Hangklip (bottom) measurement sites for the inversion with doubled NEE flux uncertainties S9. The diurnal plots are separated into working week and weekend observed concentrations (blue and light blue), working week and weekend prior modelled concentrations (red and dark red), and working week and weekend posterior modelled concentrations (green and light green).

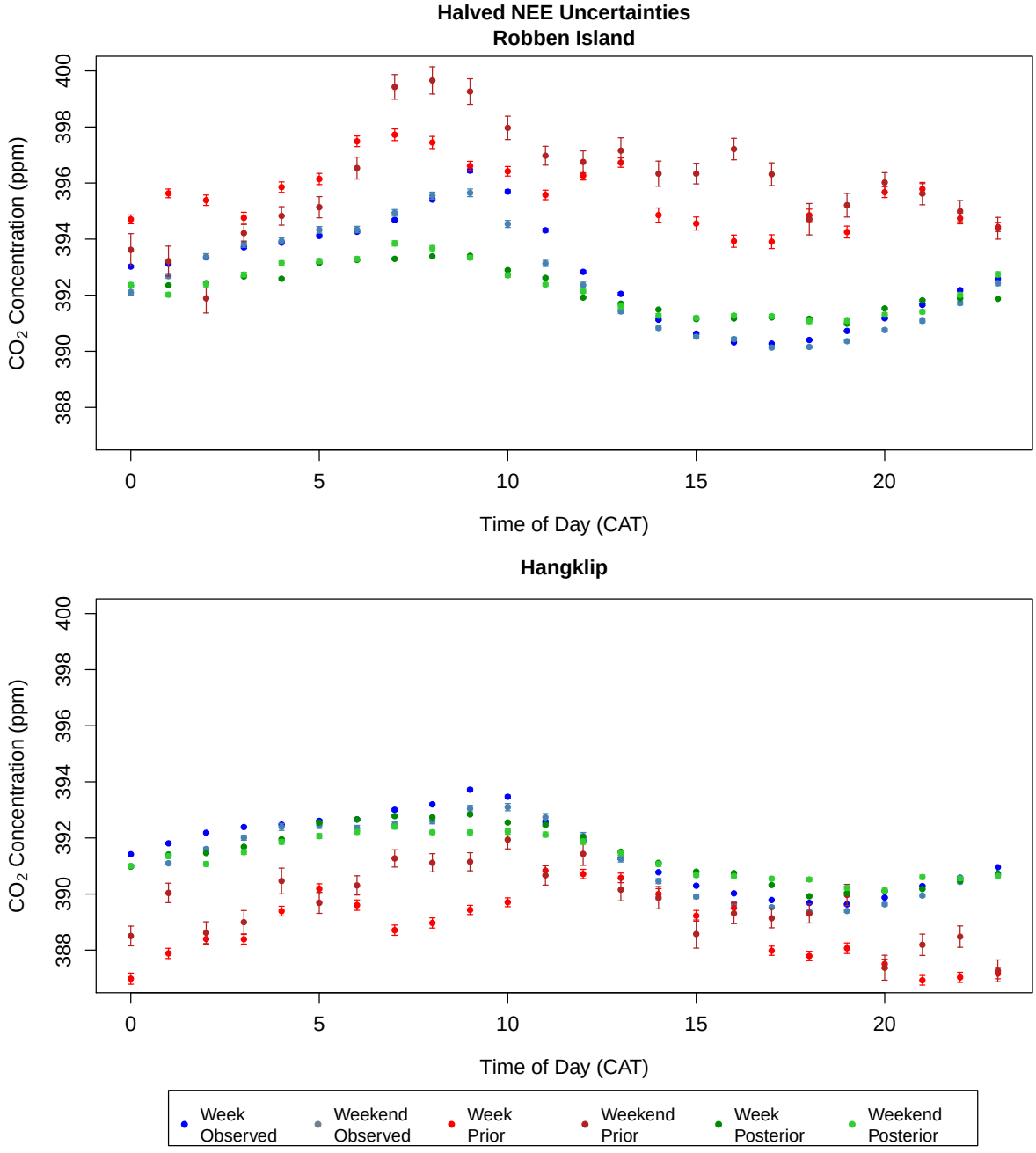

Figure S46. The hourly diurnal cycle (mean concentrations for each hour with 95% confidence interval) in the observed, prior and posterior modelled CO_2 concentrations (ppm) over the full measurement period from March 2012 until June 2013, separated by working week and weekend, and plotted separately for Robben Island (top) and Hangklip (bottom) measurement sites for the inversion with halved NEE flux uncertainties S10. The diurnal plots are separated into working week and weekend observed concentrations (blue and light blue), working week and weekend prior modelled concentrations (red and dark red), and working week and weekend posterior modelled concentrations (green and light green).

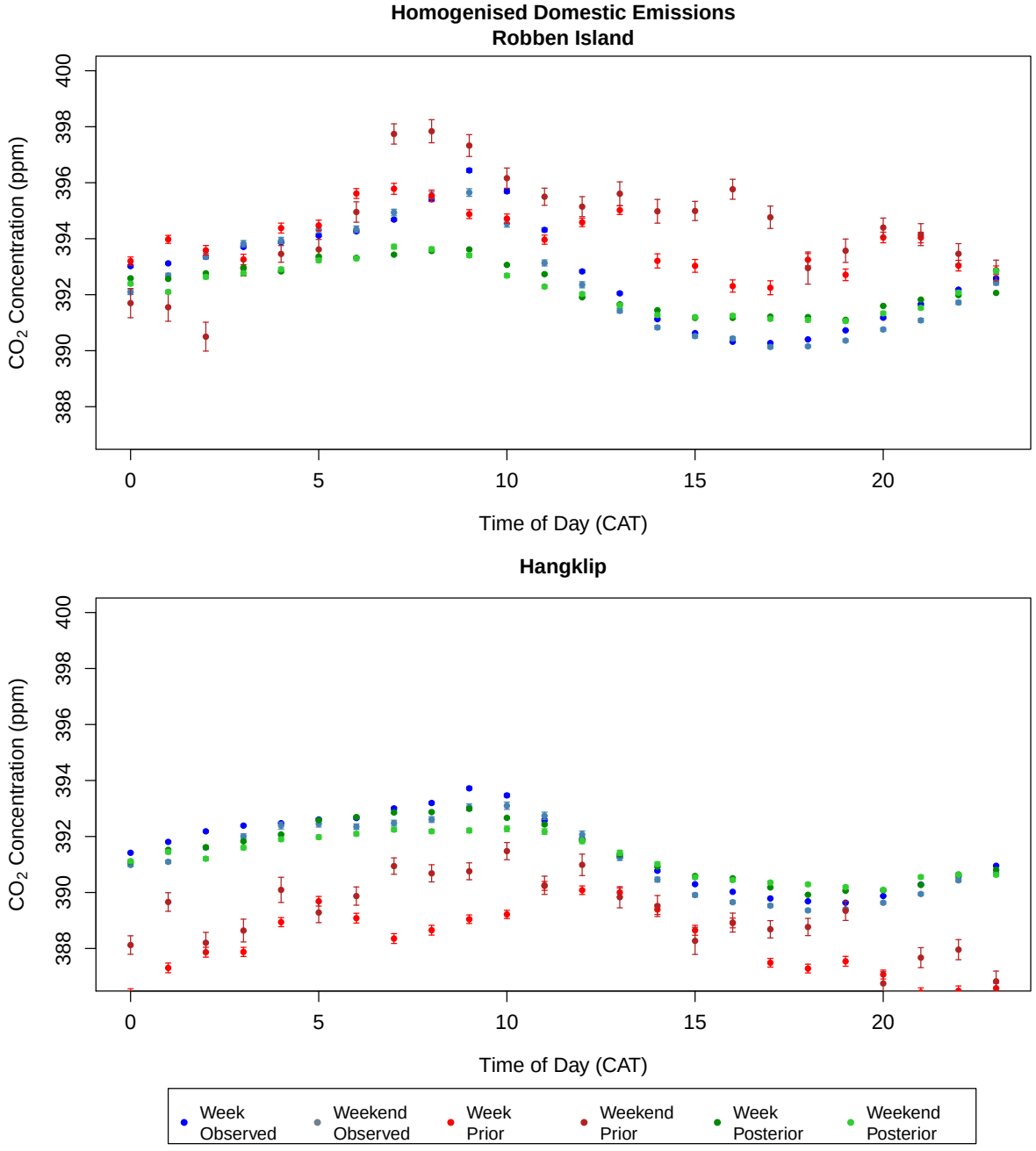

Figure S47. The hourly diurnal cycle (mean concentrations for each hour with 95% confidence interval) in the observed, prior and posterior modelled CO_2 concentrations (ppm) over the full measurement period from March 2012 until June 2013, separated by working week and weekend, and plotted separately for Robben Island (top) and Hangklip (bottom) measurement sites for the inversion with temporally homogenised domestic fossil fuel prior fluxes S11. The diurnal plots are separated into working week and weekend observed concentrations (blue and light blue), working week and weekend prior modelled concentrations (red and dark red), and working week and weekend posterior modelled concentrations (green and light green).

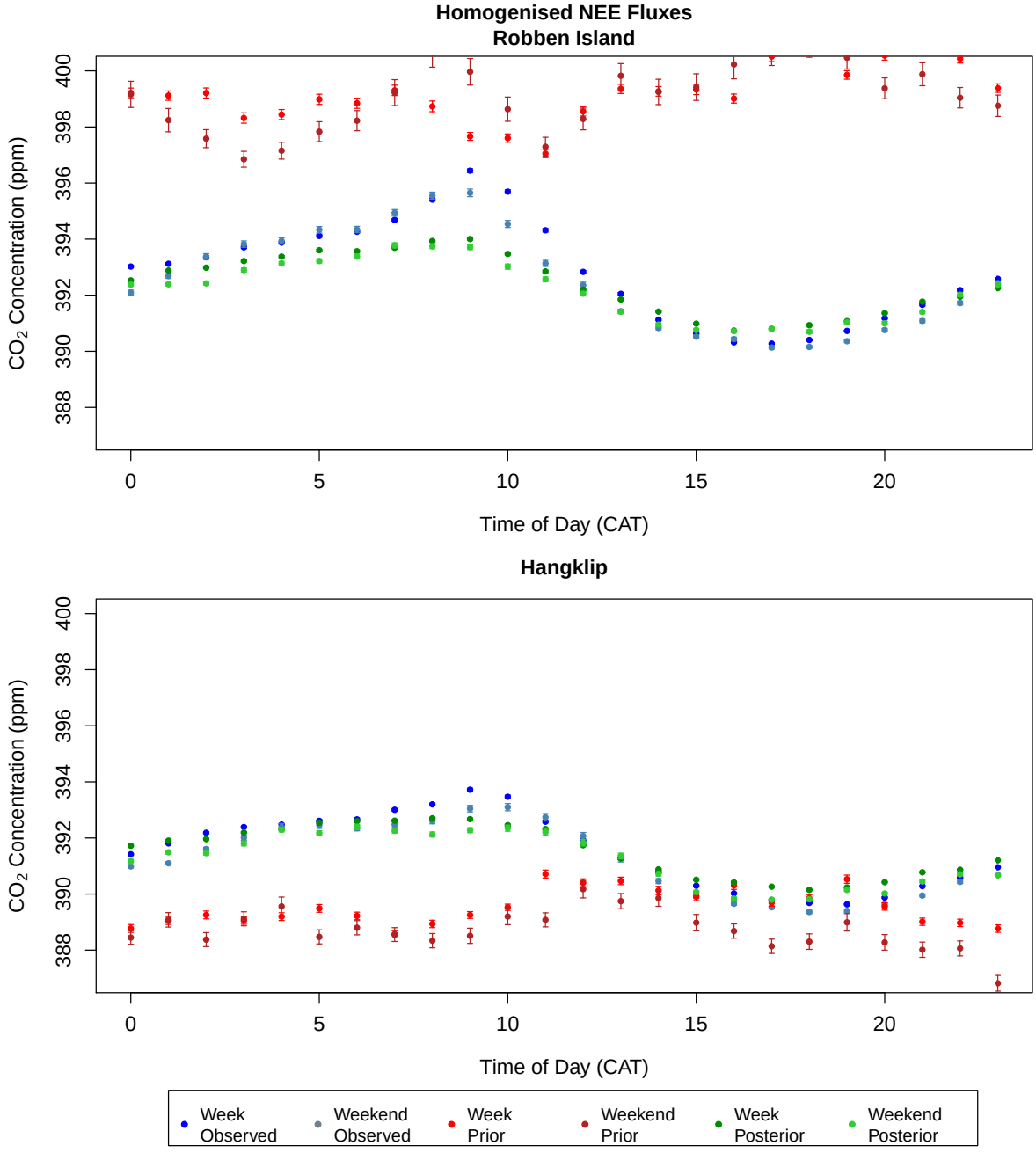

Figure S48. The hourly diurnal cycle (mean concentrations for each hour with 95% confidence interval) in the observed, prior and posterior modelled CO_2 concentrations (ppm) over the full measurement period from March 2012 until June 2013, separated by working week and weekend, and plotted separately for Robben Island (top) and Hangklip (bottom) measurement sites for the inversion with spatially homogenised NEE prior fluxes S12. The diurnal plots are separated into working week and weekend observed concentrations (blue and light blue), working week and weekend prior modelled concentrations (red and dark red), and working week and weekend posterior modelled concentrations (green and light green).

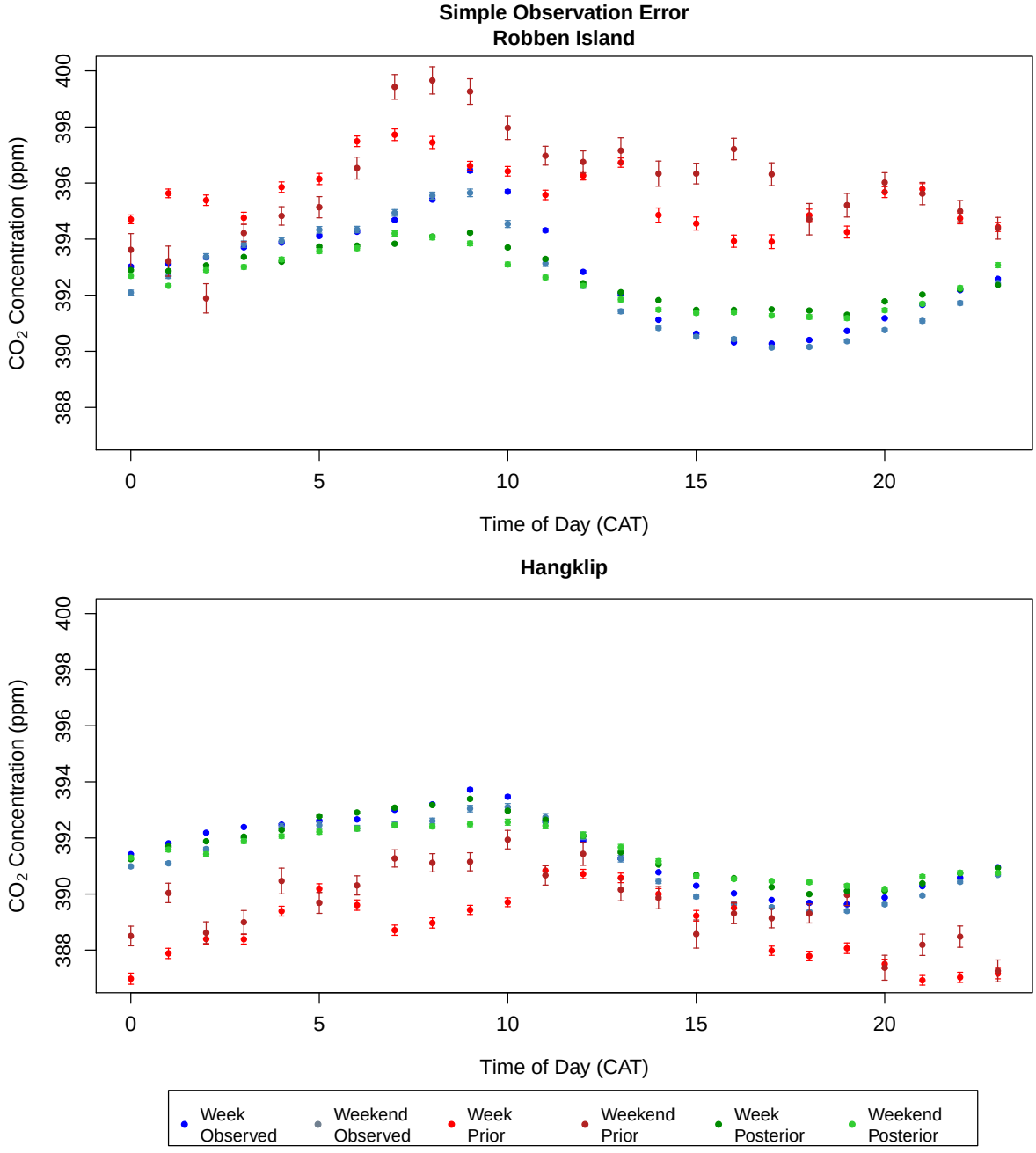

Figure S49. The hourly diurnal cycle (mean concentrations for each hour with 95% confidence interval) in the observed, prior and posterior modelled CO_2 concentrations (ppm) over the full measurement period from March 2012 until June 2013, separated by working week and weekend, and plotted separately for Robben Island (top) and Hangklip (bottom) measurement sites for the inversion specifying uncertainties of 2 ppm and 4 ppm for the day and night-time observation errors S13. The diurnal plots are separated into working week and weekend observed concentrations (blue and light blue), working week and weekend prior modelled concentrations (red and dark red), and working week and weekend posterior modelled concentrations (green and light green).

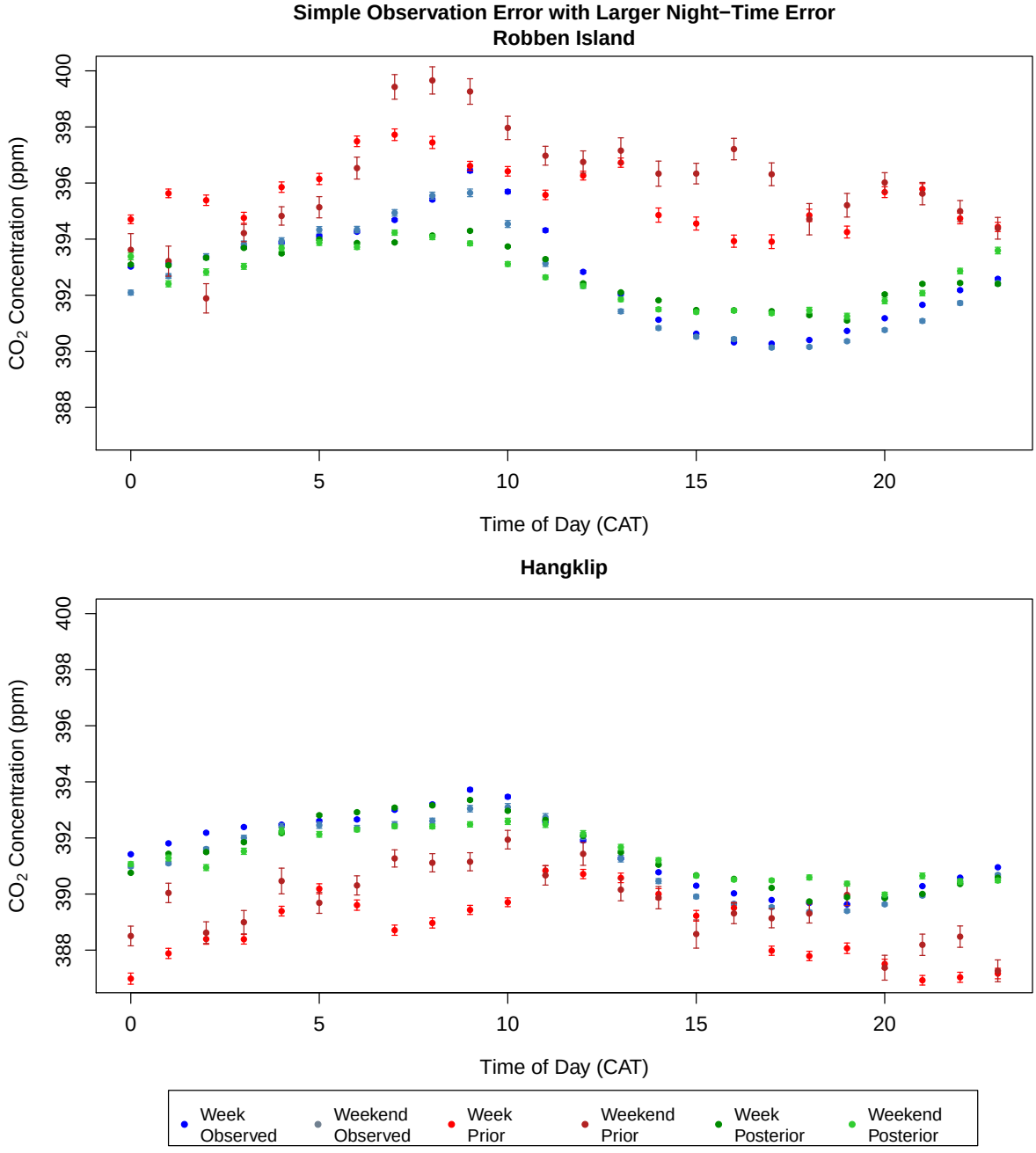

Figure S50. The hourly diurnal cycle (mean concentrations for each hour with 95% confidence interval) in the observed, prior and posterior modelled CO_2 concentrations (ppm) over the full measurement period from March 2012 until June 2013, separated by working week and weekend, and plotted separately for Robben Island (top) and Hangklip (bottom) measurement sites for the inversion specifying uncertainties of 2 ppm and 10 ppm for the day and night-time observation errors S14. The diurnal plots are separated into working week and weekend observed concentrations (blue and light blue), working week and weekend prior modelled concentrations (red and dark red), and working week and weekend posterior modelled concentrations (green and light green).

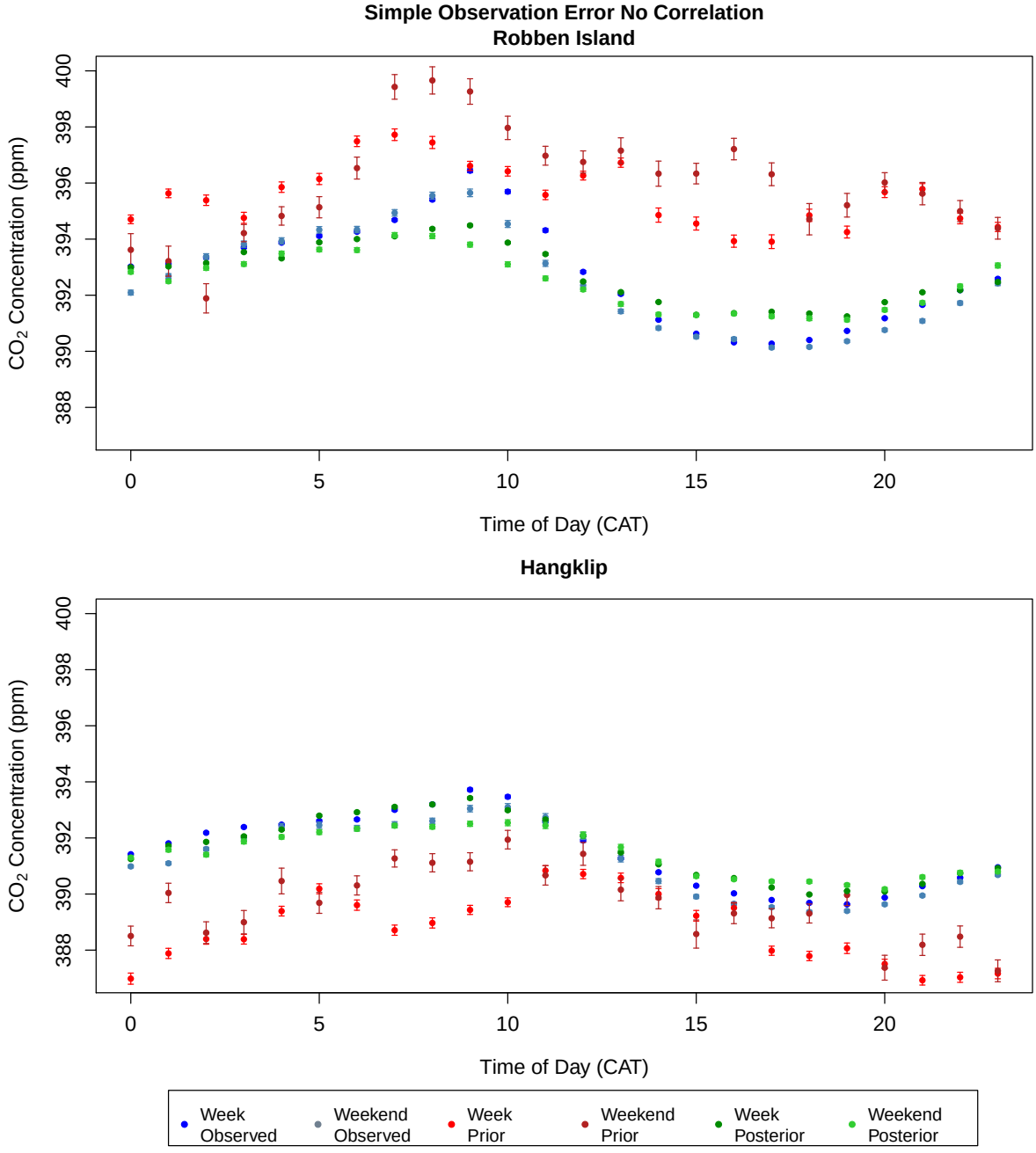

Figure S51. The hourly diurnal cycle (mean concentrations for each hour with 95% confidence interval) in the observed, prior and posterior modelled CO_2 concentrations (ppm) over the full measurement period from March 2012 until June 2013, separated by working week and weekend, and plotted separately for Robben Island (top) and Hangklip (bottom) measurement sites for the inversion specifying uncertainties of 2 ppm and 4 ppm for the day and night-time observation errors with no correlation S15. The diurnal plots are separated into working week and weekend observed concentrations (blue and light blue), working week and weekend prior modelled concentrations (red and dark red), and working week and weekend posterior modelled concentrations (green and light green).

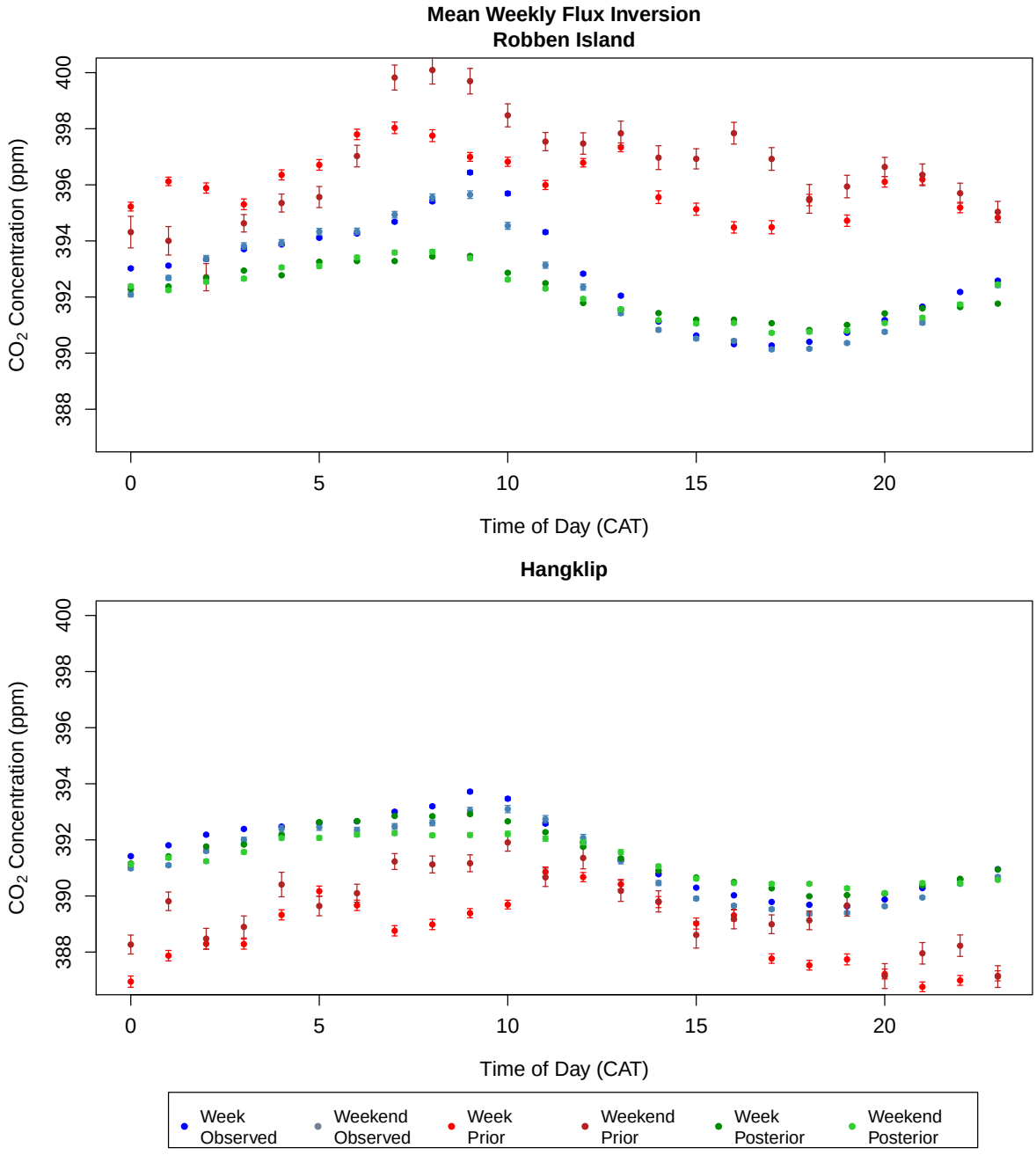

Figure S52. The hourly diurnal cycle (mean concentrations for each hour with 95% confidence interval) in the observed, prior and posterior modelled CO_2 concentrations (ppm) over the full measurement period from March 2012 until June 2013, separated by working week and weekend, and plotted separately for Robben Island (top) and Hangklip (bottom) measurement sites for the inversion solving for the mean weekly flux S16. The diurnal plots are separated into working week and weekend observed concentrations (blue and light blue), working week and weekend prior modelled concentrations (red and dark red), and working week and weekend posterior modelled concentrations (green and light green).

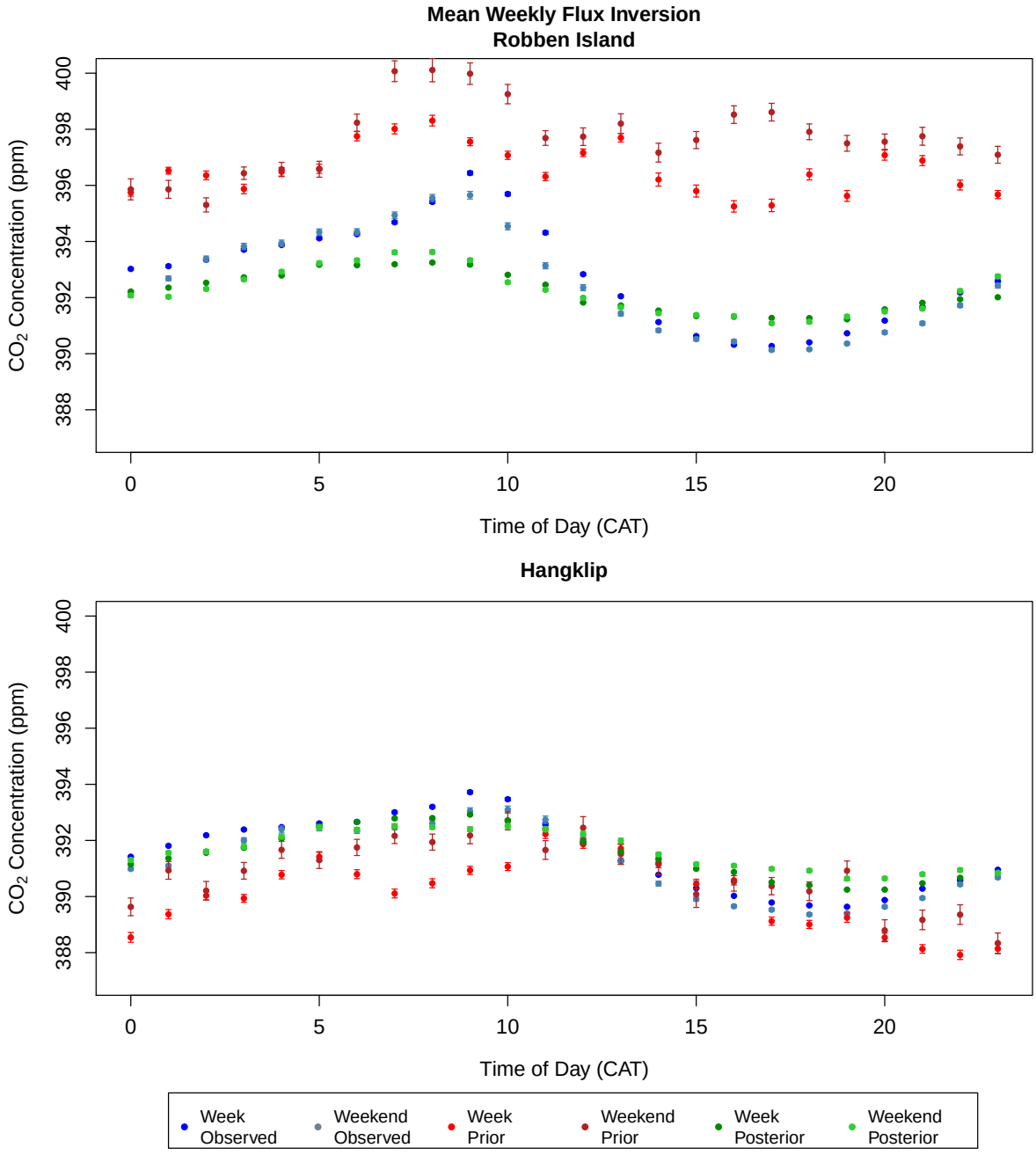

Figure S53. The hourly diurnal cycle (mean concentrations for each hour with 95% confidence interval) in the observed, prior and posterior modelled CO_2 concentrations (ppm) over the full measurement period from March 2012 until June 2013, separated by working week and weekend, and plotted separately for Robben Island (top) and Hangklip (bottom) measurement sites for the separate weekly inversions S17. The diurnal plots are separated into working week and weekend observed concentrations (blue and light blue), working week and weekend prior modelled concentrations (red and dark red), and working week and weekend posterior modelled concentrations (green and light green).

1.6 Spatial Distribution of Prior and Posterior Fluxes, and Uncertainty Reductions

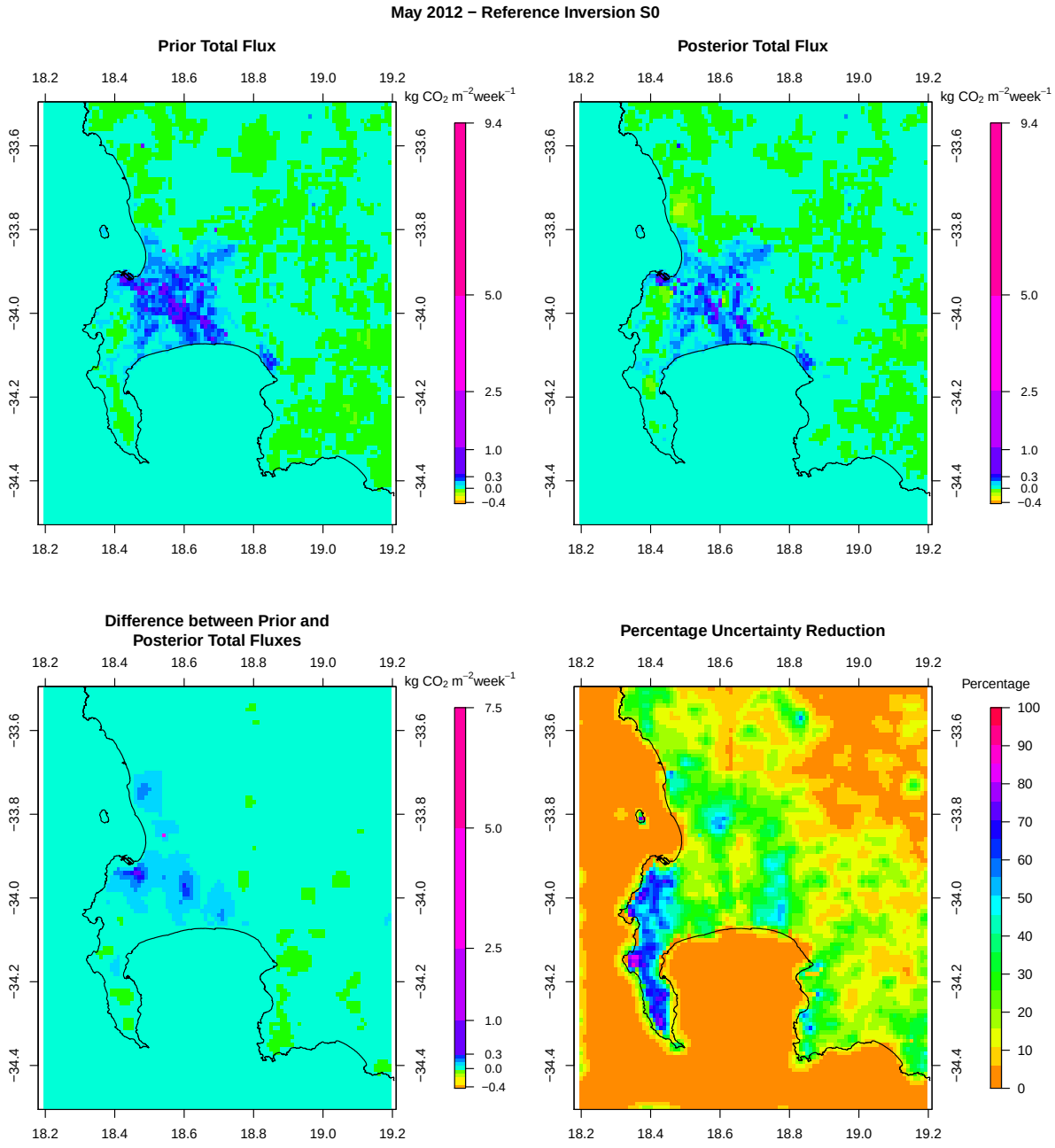

Figure S54. Spatial distribution of the pixel-level prior and posterior CO_2 fluxes of the reference inversion S0, the difference between prior and posterior flux estimates, and the uncertainty reduction relative to the prior uncertainty for May 2012.

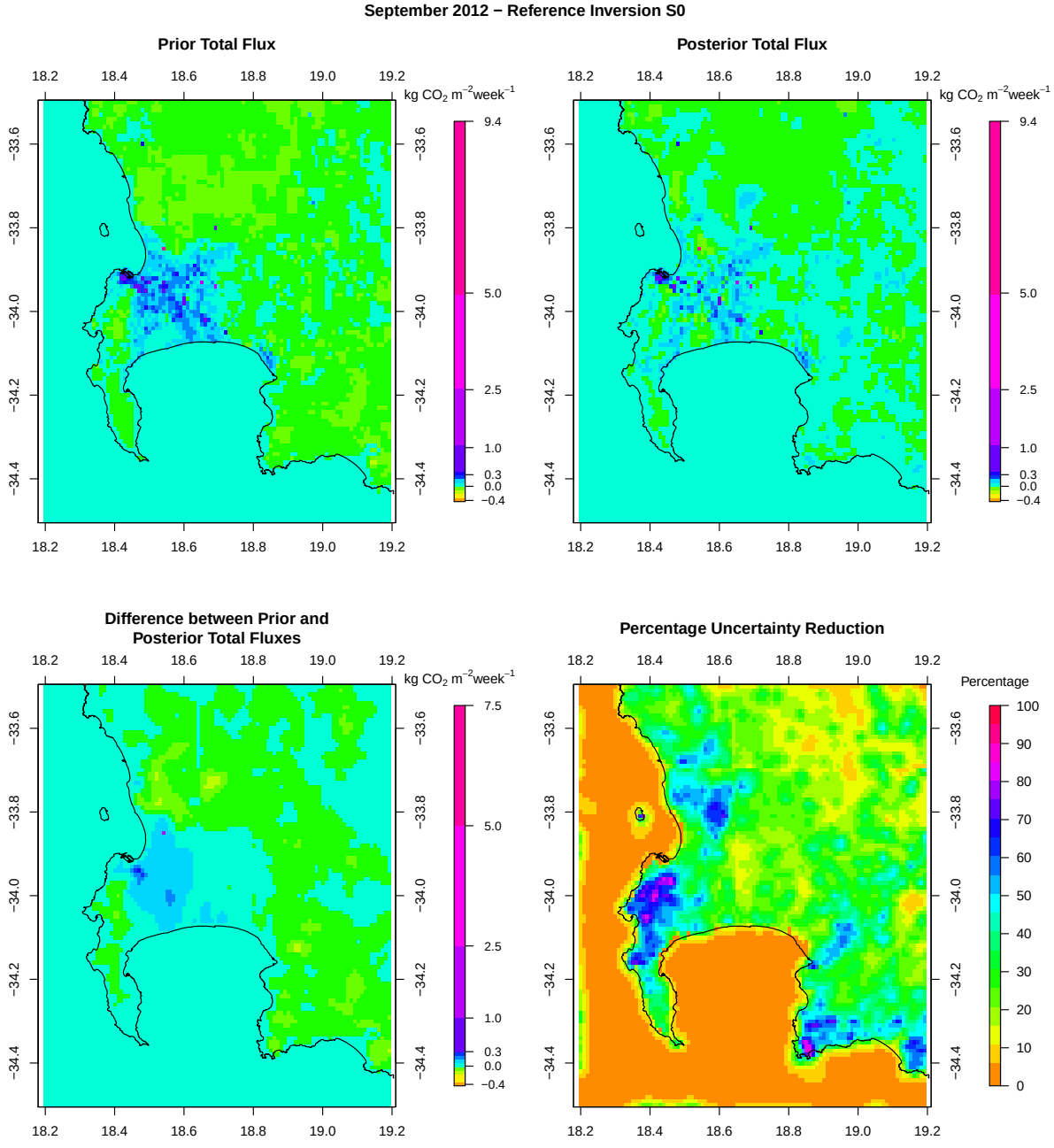

Figure S55. Spatial distribution of the pixel-level prior and posterior CO_2 fluxes of the reference inversion S0, the difference between prior and posterior flux estimates, and the uncertainty reduction relative to the prior uncertainty for September 2012.

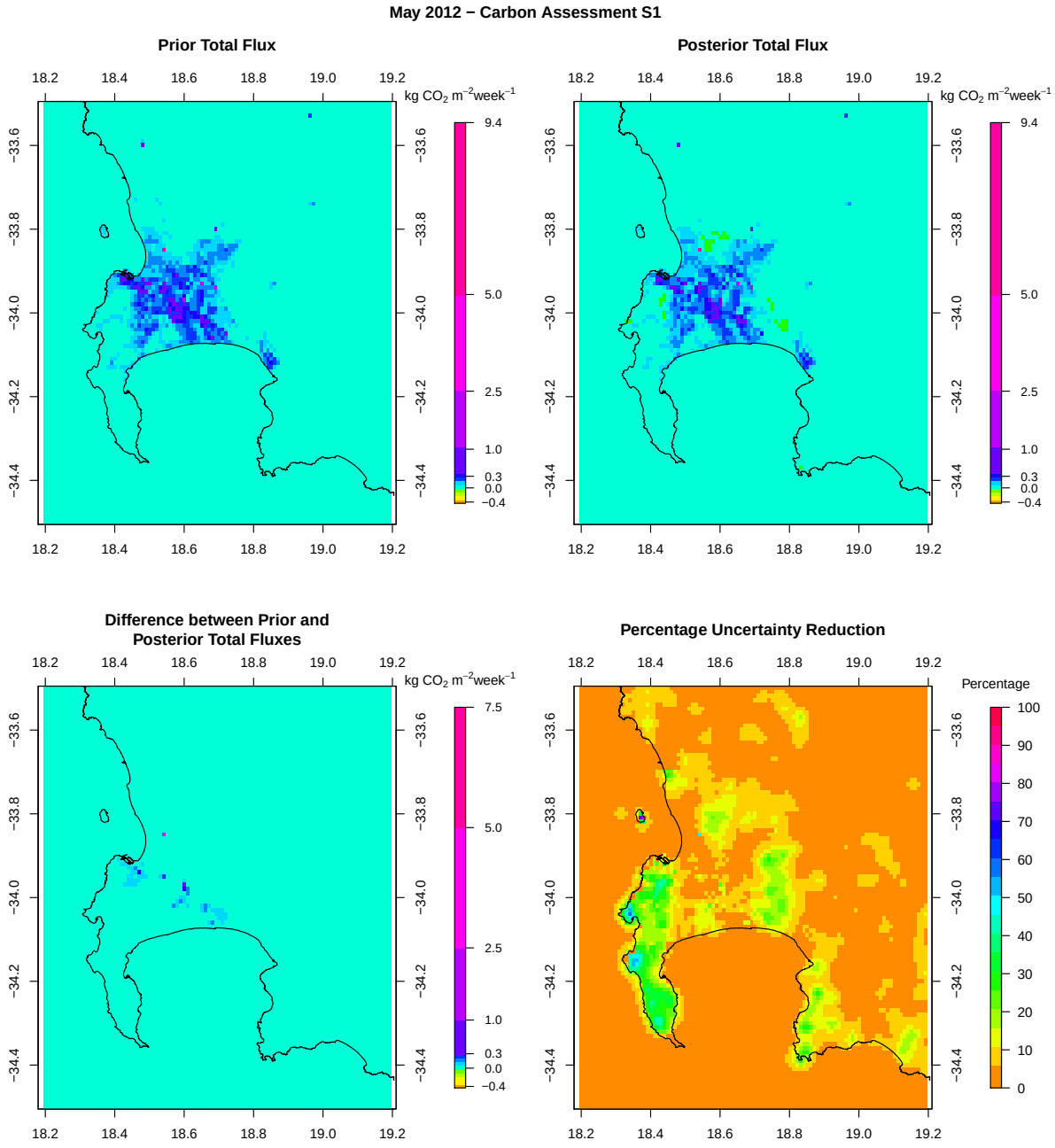

Figure S56. Spatial distribution of the pixel-level prior and posterior CO_2 fluxes of the inversion using the carbon assessment product for the NEE prior flux estimates S1, the difference between prior and posterior flux estimates, and the uncertainty reduction relative to the prior uncertainty for May 2012.

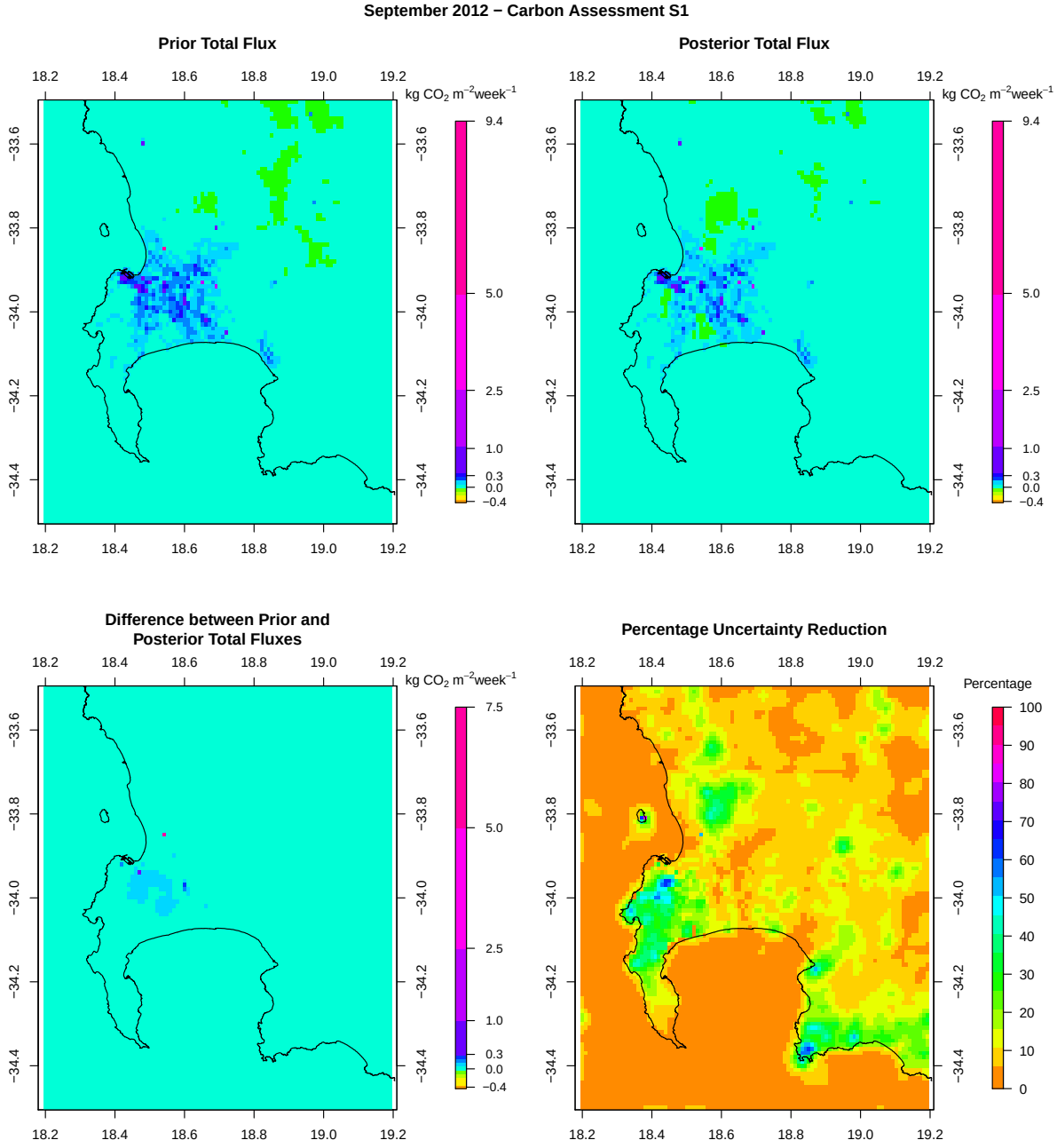

Figure S57. Spatial distribution of the pixel-level prior and posterior CO_2 fluxes of the inversion using the carbon assessment product for the NEE prior flux estimates S1, the difference between prior and posterior flux estimates, and the uncertainty reduction relative to the prior uncertainty for September 2012.

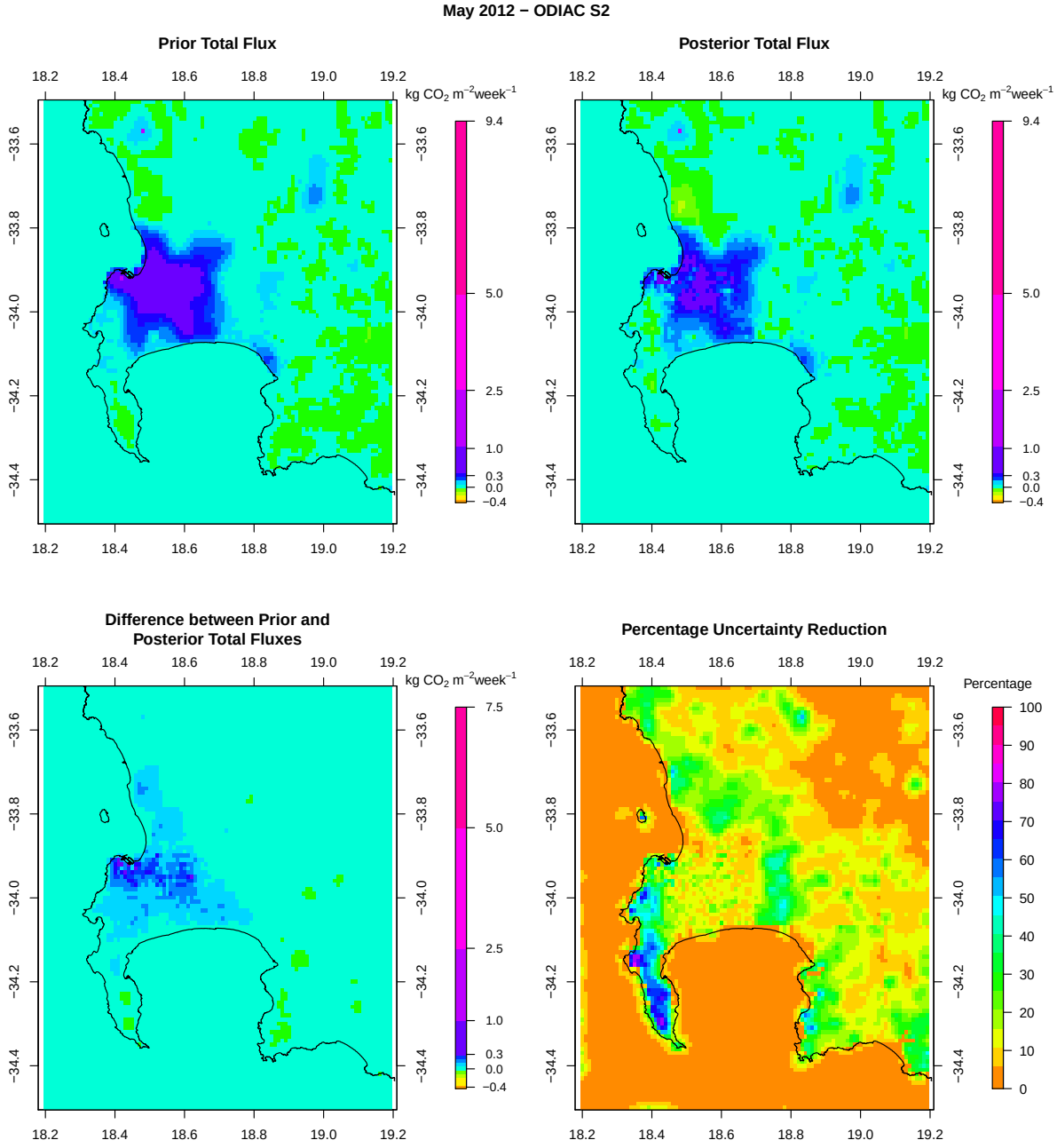

Figure S58. Spatial distribution of the pixel-level prior and posterior CO_2 fluxes of the inversion using the ODIAC product for the fossil fuel flux prior estimates S2, the difference between prior and posterior flux estimates, and the uncertainty reduction relative to the prior uncertainty for May 2012.

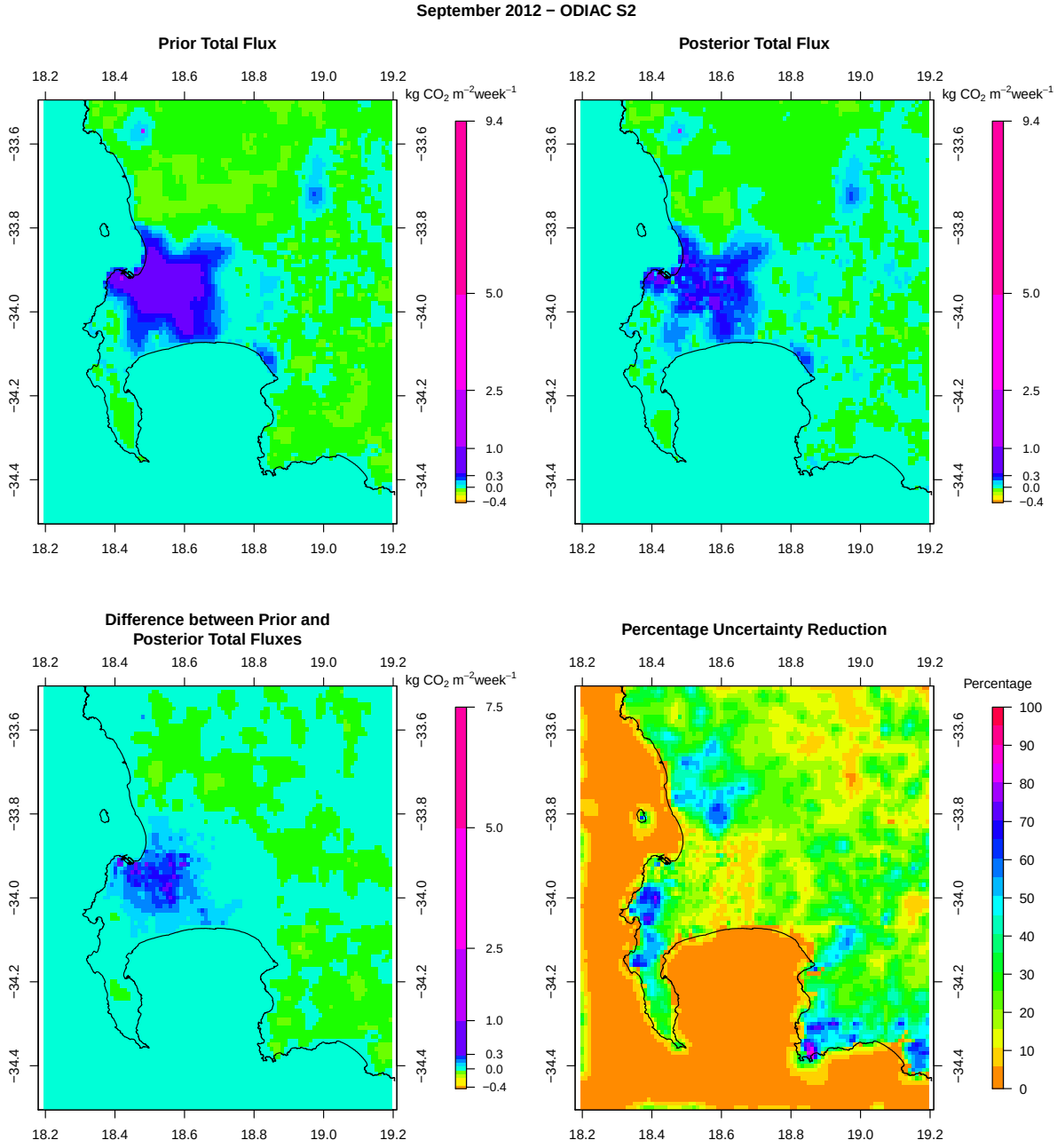

Figure S59. Spatial distribution of the pixel-level prior and posterior CO_2 fluxes of the inversion using the ODIAC product for the fossil fuel flux prior estimates S2, the difference between prior and posterior flux estimates, and the uncertainty reduction relative to the prior uncertainty for September 2012.

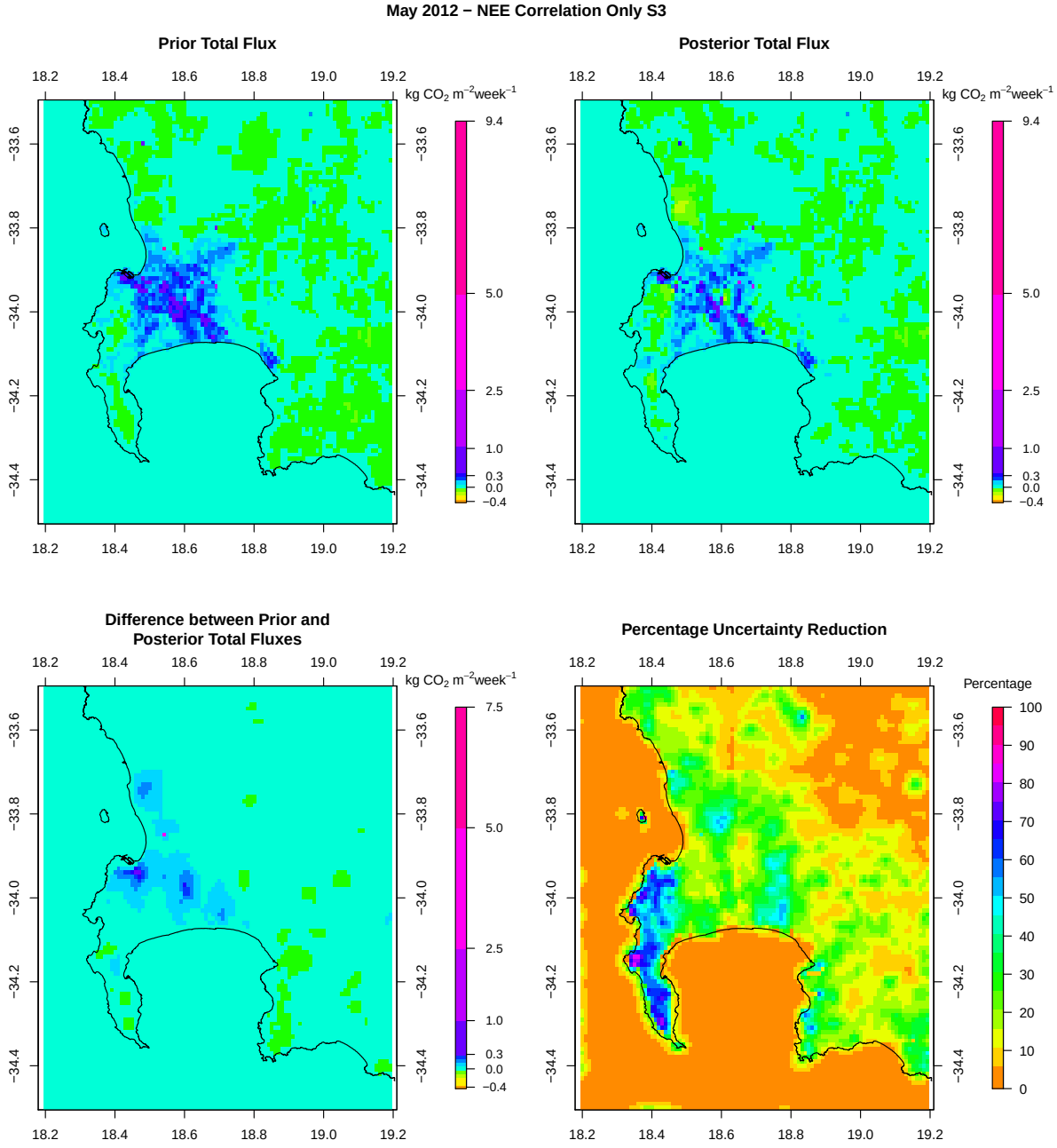

Figure S60. Spatial distribution of the pixel-level prior and posterior CO_2 fluxes of the inversion accounting for only correlation between the NEE flux uncertainties S3, the difference between prior and posterior flux estimates, and the uncertainty reduction relative to the prior uncertainty for May 2012.

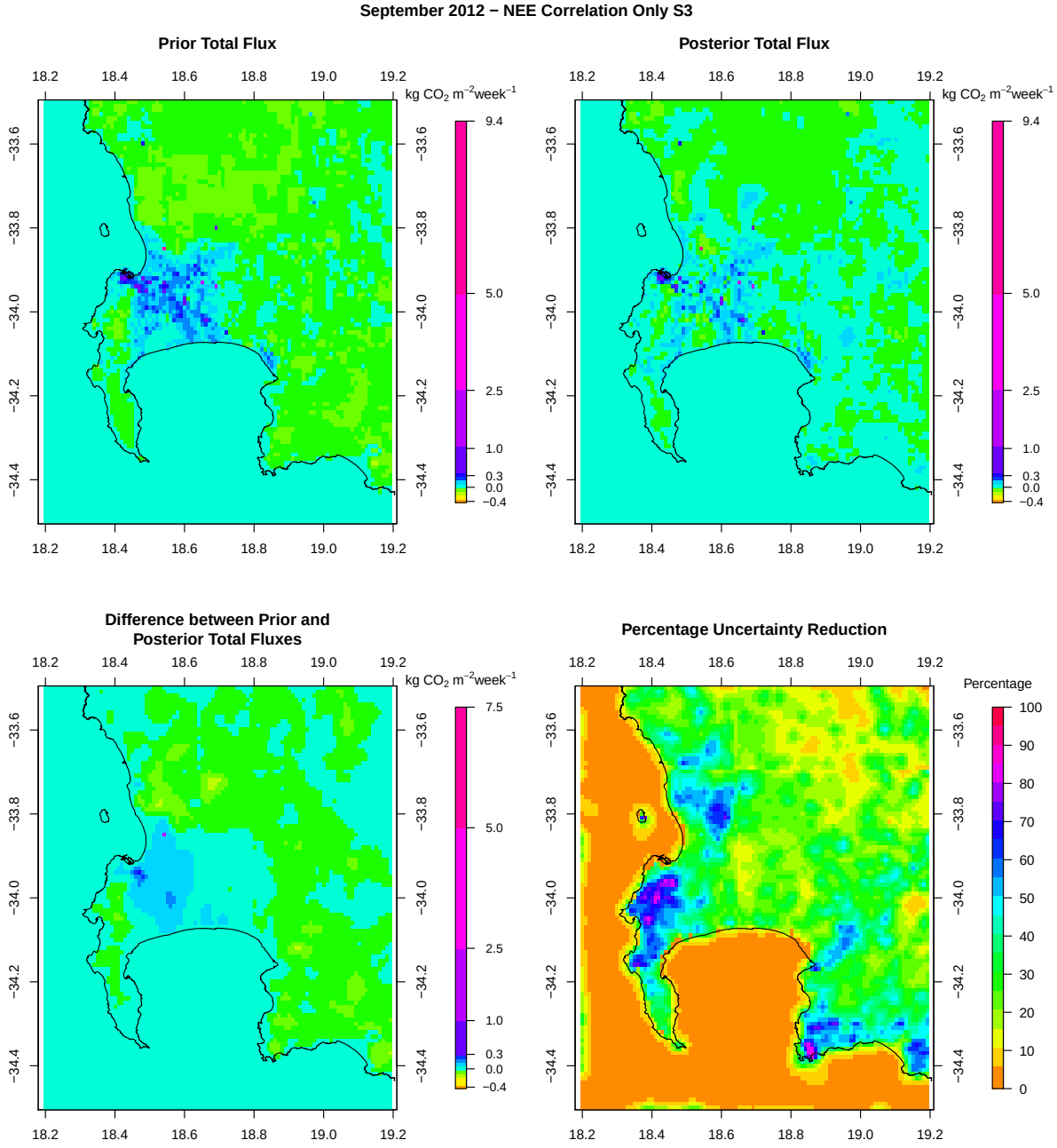

Figure S61. Spatial distribution of the pixel-level prior and posterior CO_2 fluxes of the inversion accounting for only correlation between the NEE flux uncertainties S3, the difference between prior and posterior flux estimates, and the uncertainty reduction relative to the prior uncertainty for September 2012.

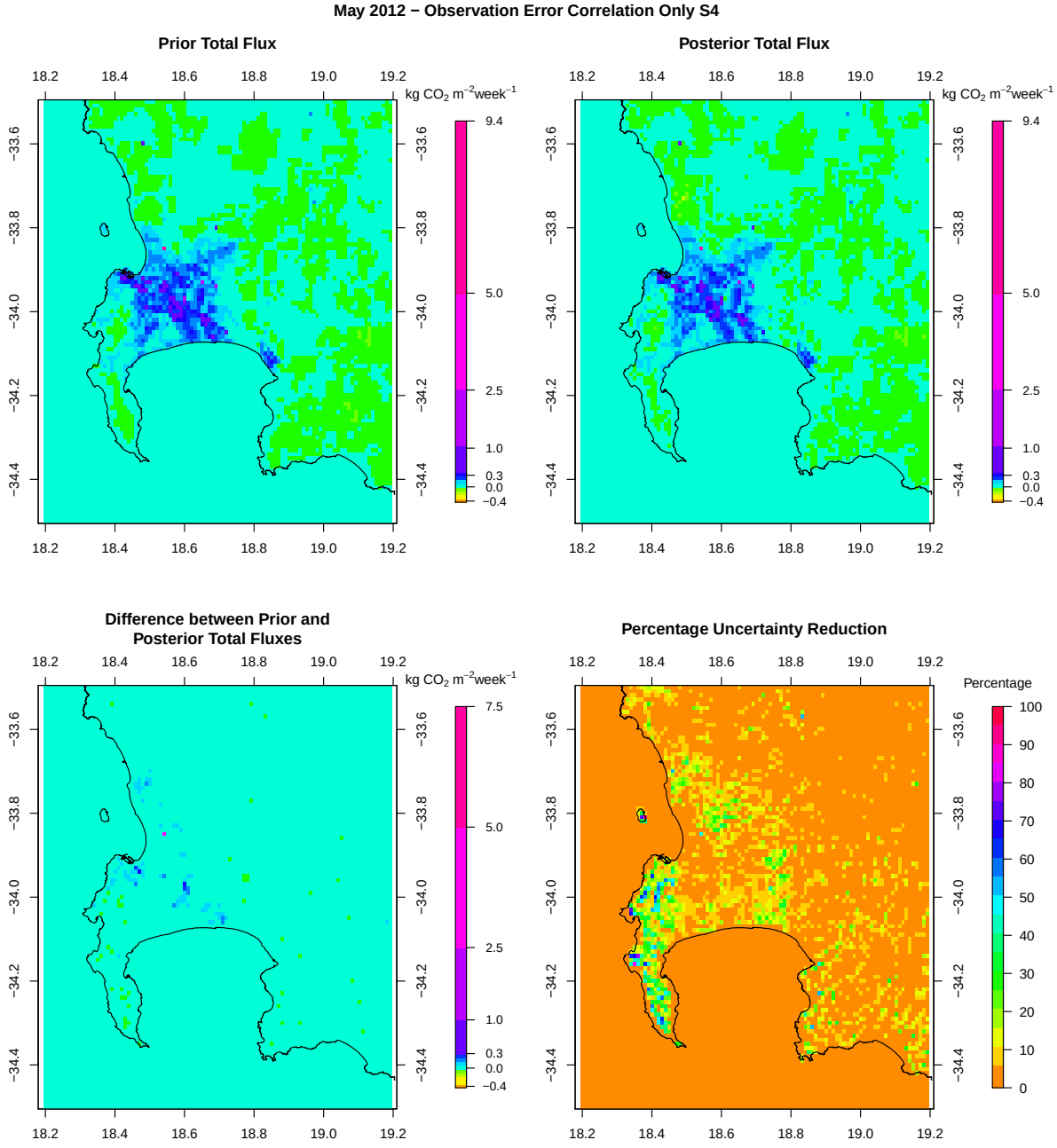

Figure S62. Spatial distribution of the pixel-level prior and posterior CO_2 fluxes of the inversion accounting for only correlation between the observation errors with no correlation specified between the NEE flux uncertainties S4, the difference between prior and posterior flux estimates, and the uncertainty reduction relative to the prior uncertainty for May 2012.

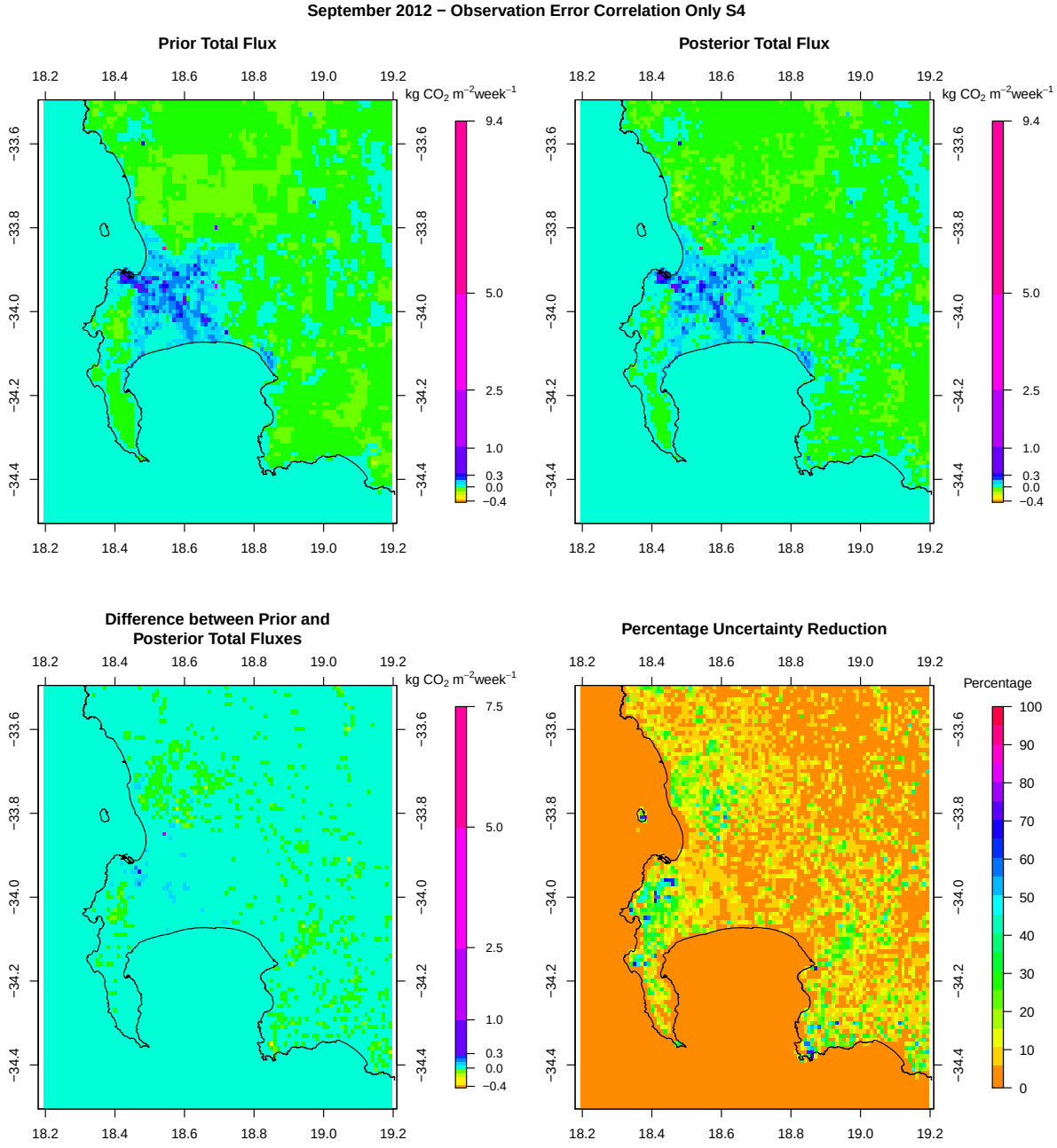

Figure S63. Spatial distribution of the pixel-level prior and posterior CO_2 fluxes of the inversion accounting for only correlation between the observation errors with no correlation specified between the NEE flux uncertainties S4, the difference between prior and posterior flux estimates, and the uncertainty reduction relative to the prior uncertainty for September 2012.

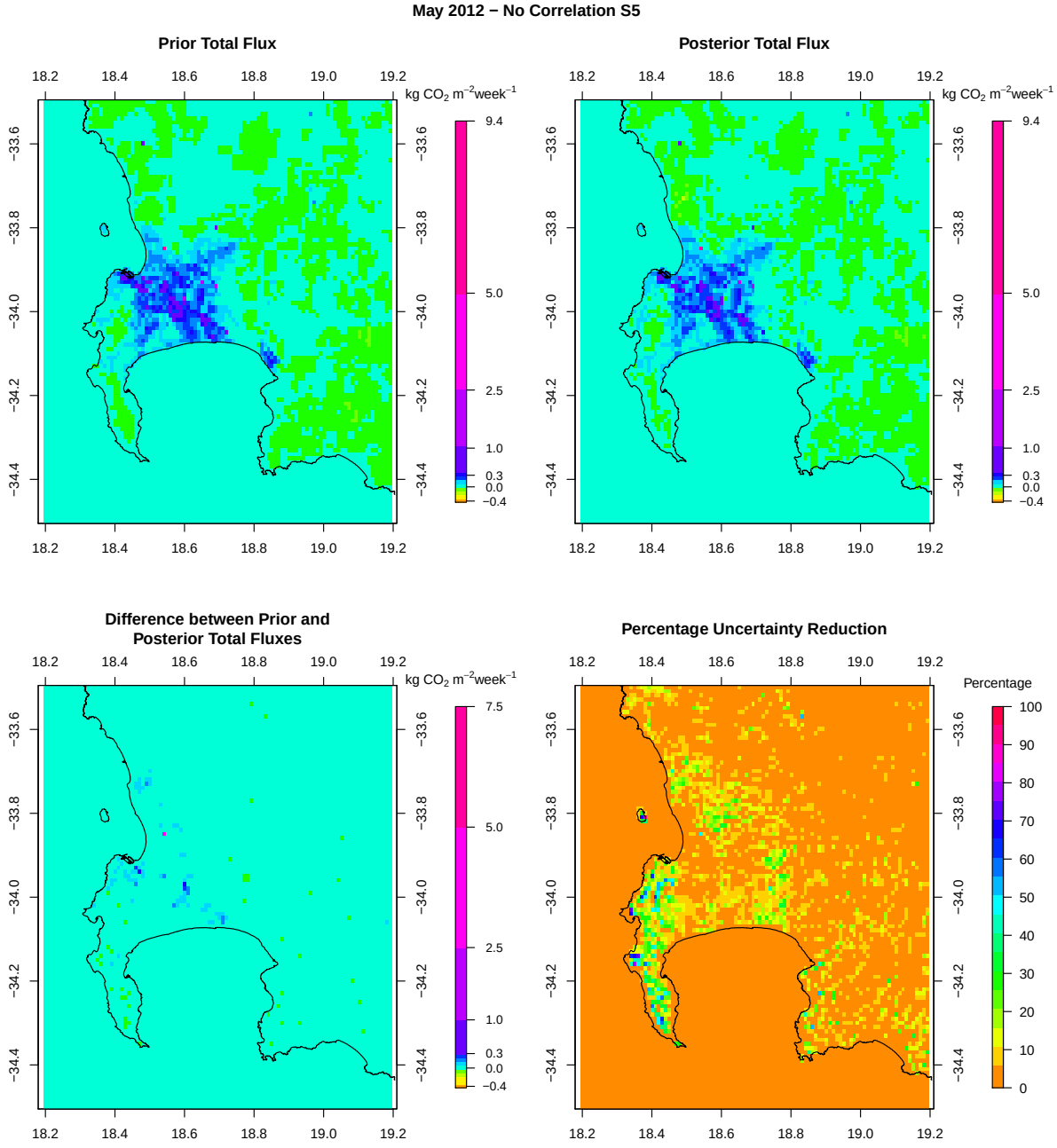

Figure S64. Spatial distribution of the pixel-level prior and posterior CO_2 fluxes of the inversion specifying no correlation between the observation errors and no correlation between the NEE flux uncertainties S5, the difference between prior and posterior flux estimates, and the uncertainty reduction relative to the prior uncertainty for May 2012.

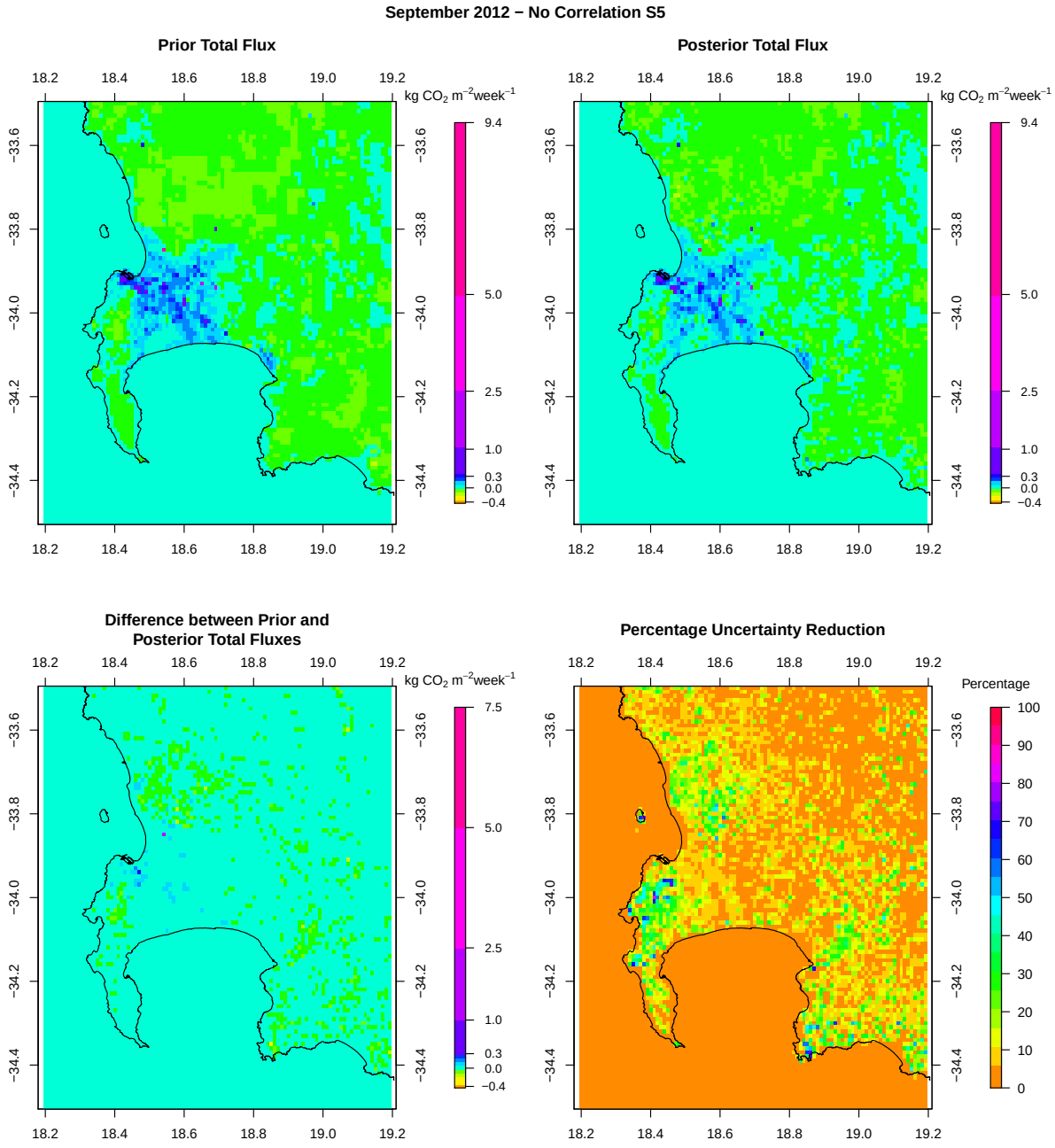

Figure S65. Spatial distribution of the pixel-level prior and posterior CO_2 fluxes of the inversion specifying no correlation between the observation errors and no correlation between the NEE flux uncertainties S5, the difference between prior and posterior flux estimates, and the uncertainty reduction relative to the prior uncertainty for September 2012.

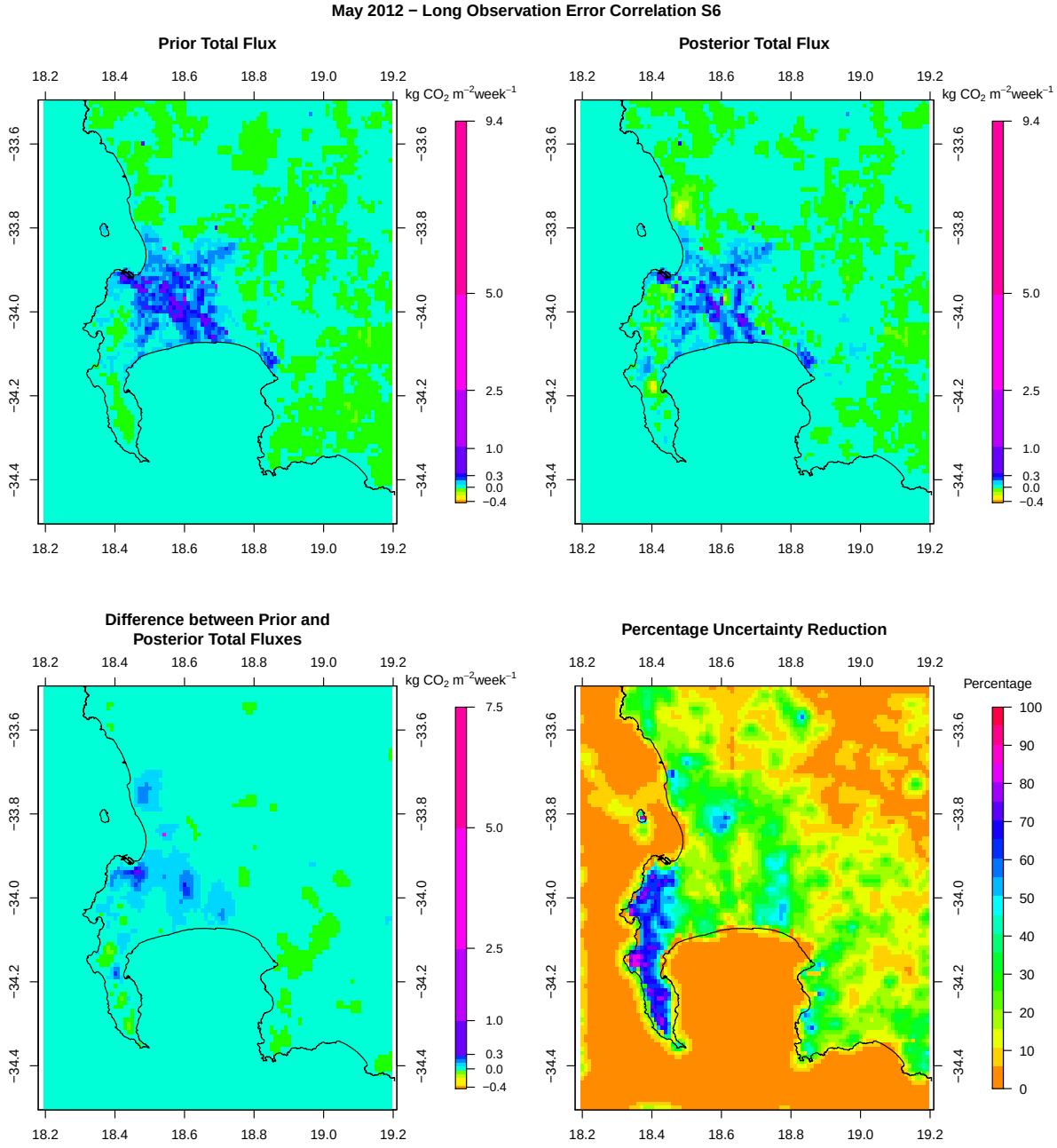

Figure S66. Spatial distribution of the pixel-level prior and posterior CO_2 fluxes of the inversion specifying a seven hour error correlation length for the observations S6, the difference between prior and posterior flux estimates, and the uncertainty reduction relative to the prior uncertainty for May 2012.

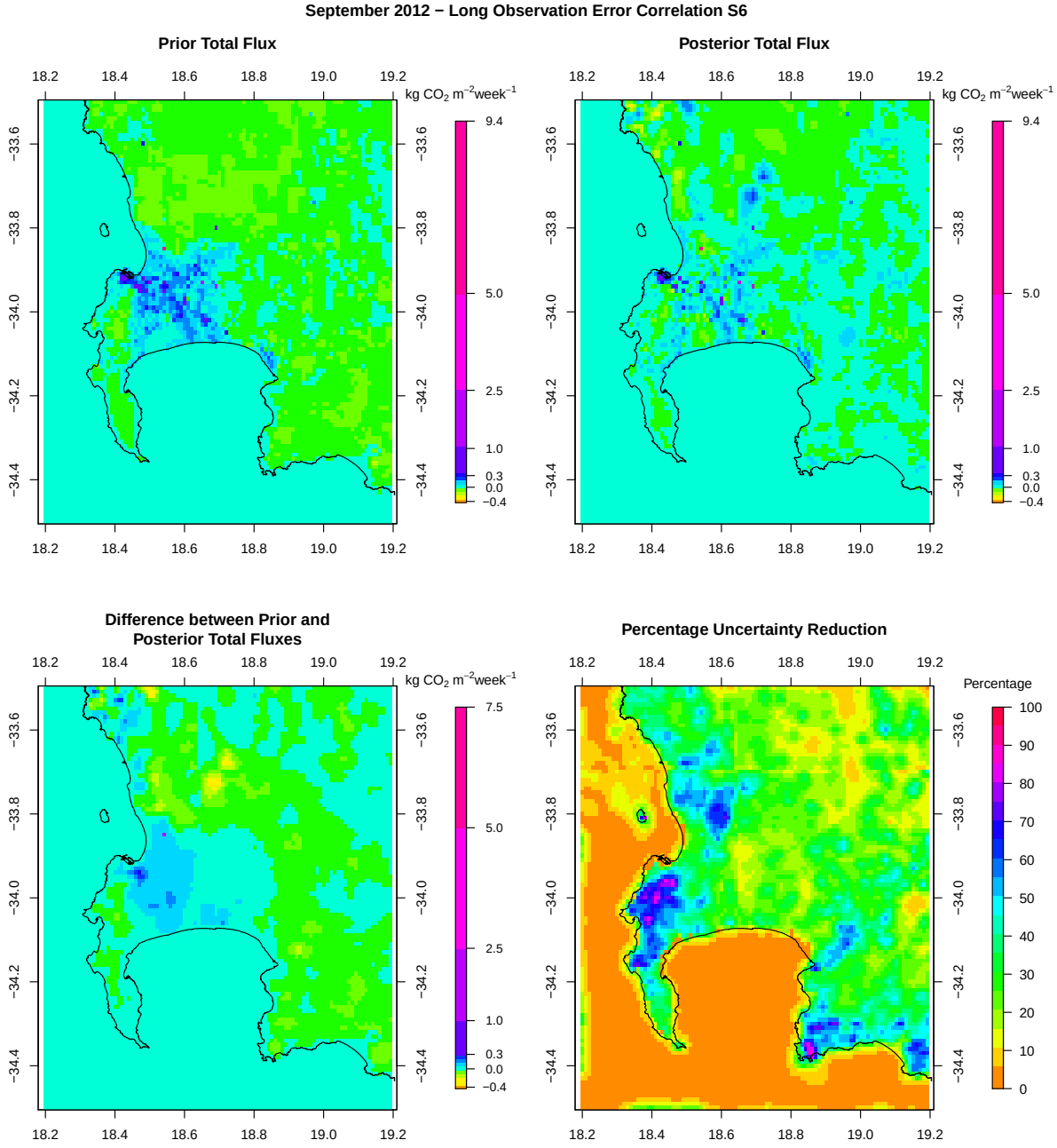

Figure S67. Spatial distribution of the pixel-level prior and posterior CO_2 fluxes of the inversion specifying a seven hour error correlation length for the observations S6, the difference between prior and posterior flux estimates, and the uncertainty reduction relative to the prior uncertainty for September 2012.

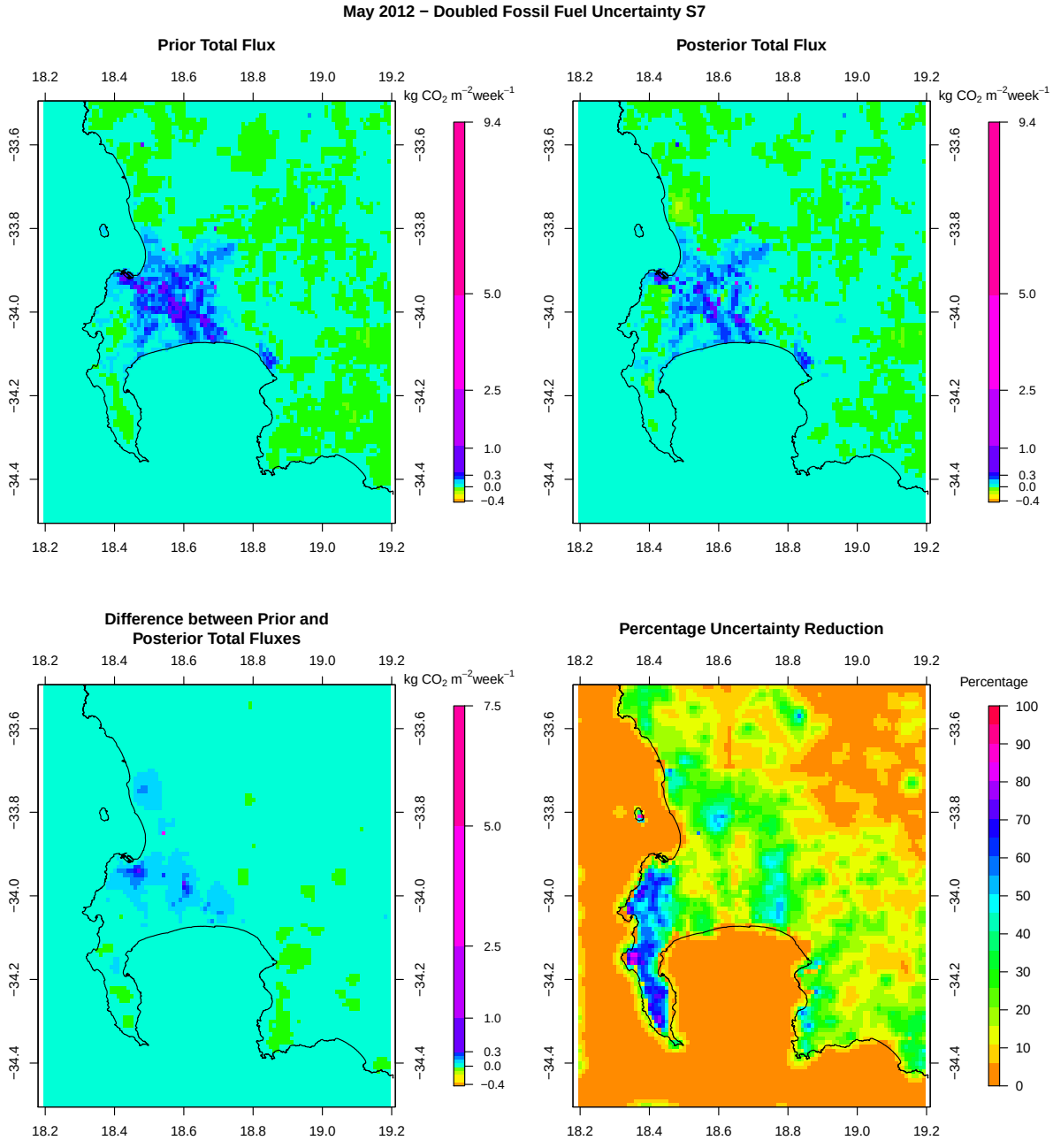

Figure S68. Spatial distribution of the pixel-level prior and posterior CO_2 fluxes of the inversion with doubled fossil fuel flux uncertainties S7, the difference between prior and posterior flux estimates, and the uncertainty reduction relative to the prior uncertainty for May 2012.

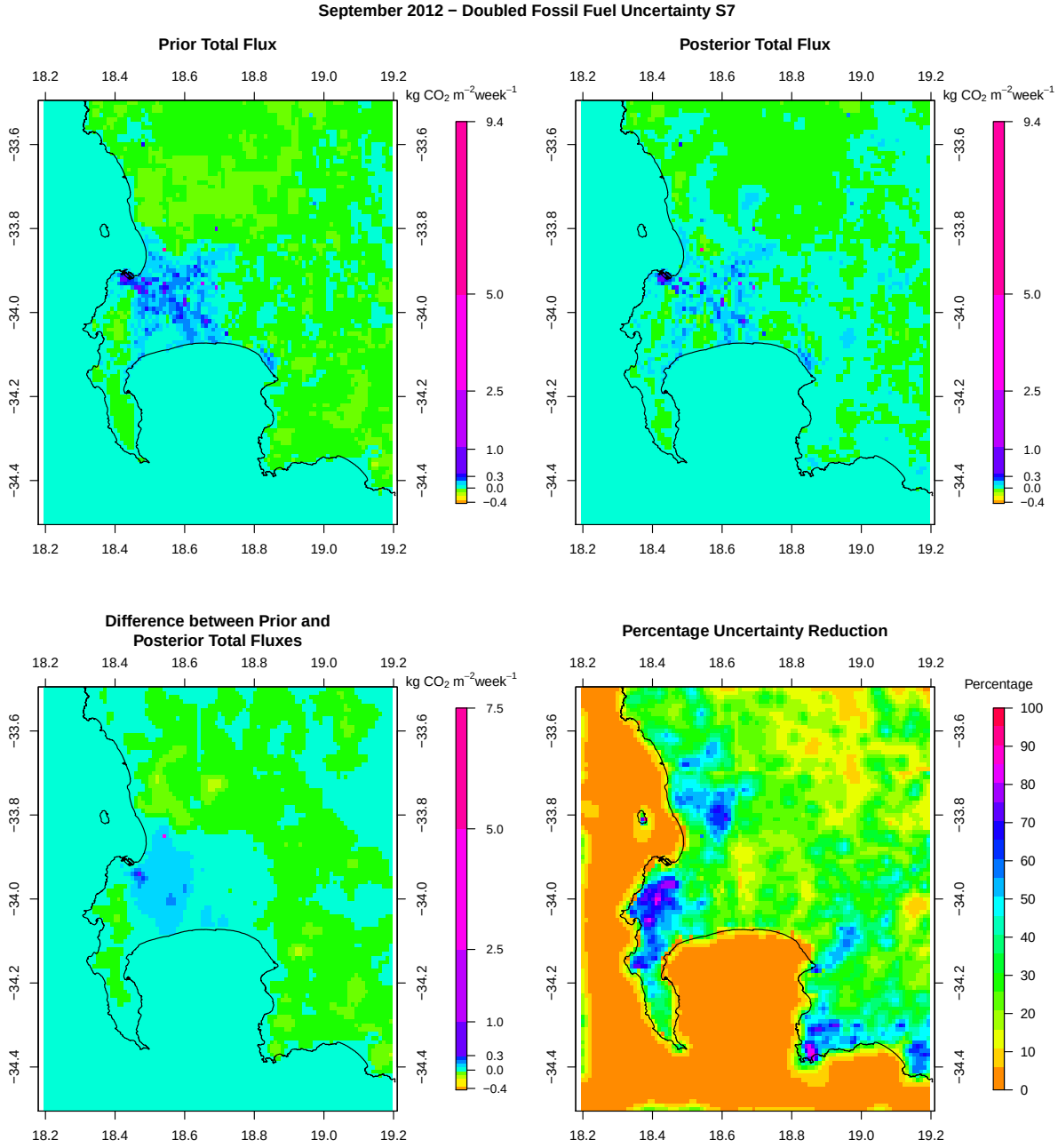

Figure S69. Spatial distribution of the pixel-level prior and posterior CO_2 fluxes of the inversion with doubled fossil fuel flux uncertainties S7, the difference between prior and posterior flux estimates, and the uncertainty reduction relative to the prior uncertainty for September 2012.

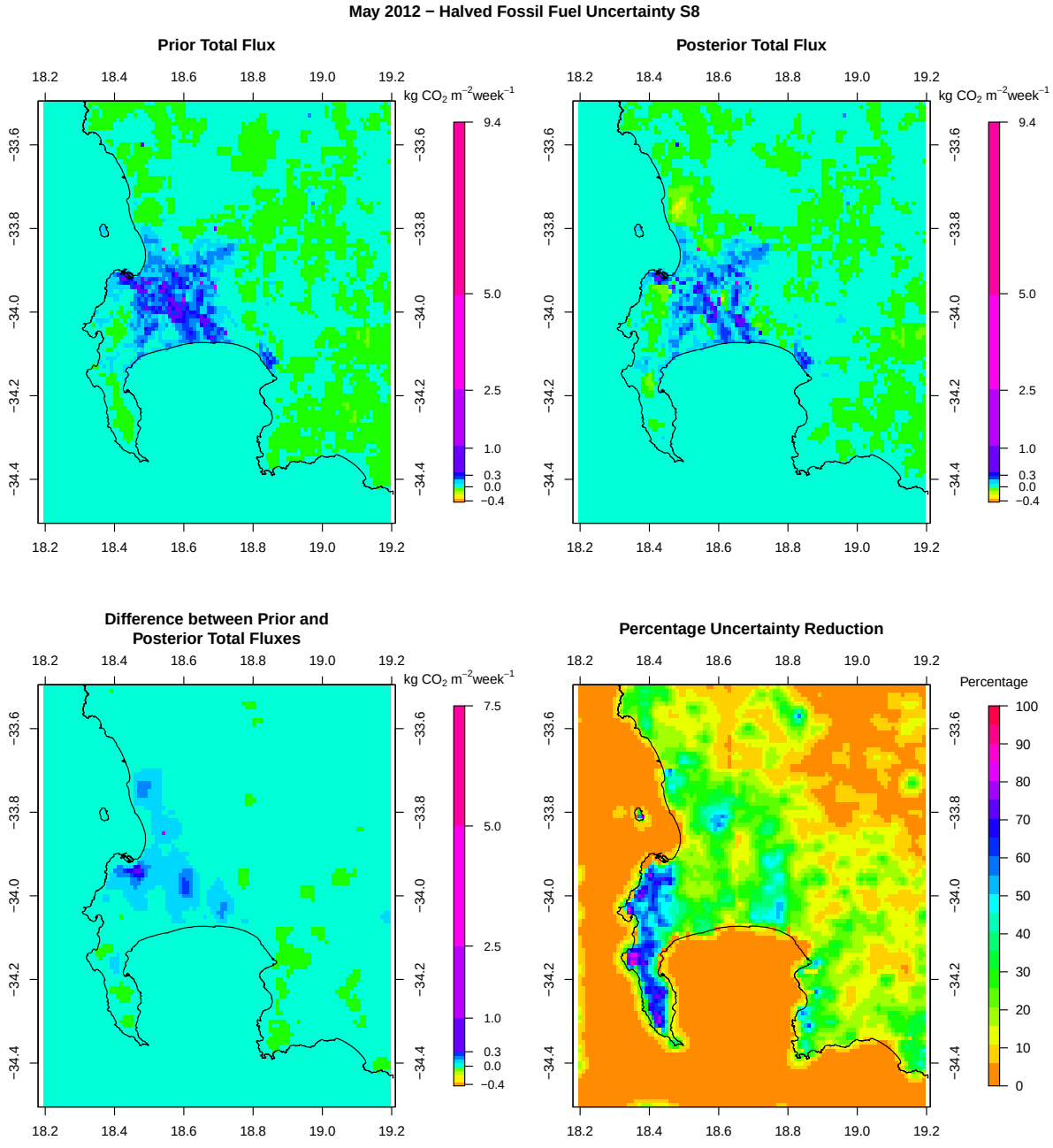

Figure S70. Spatial distribution of the pixel-level prior and posterior CO_2 fluxes of the inversion with halved fossil fuel flux uncertainties S8, the difference between prior and posterior flux estimates, and the uncertainty reduction relative to the prior uncertainty for May 2012.

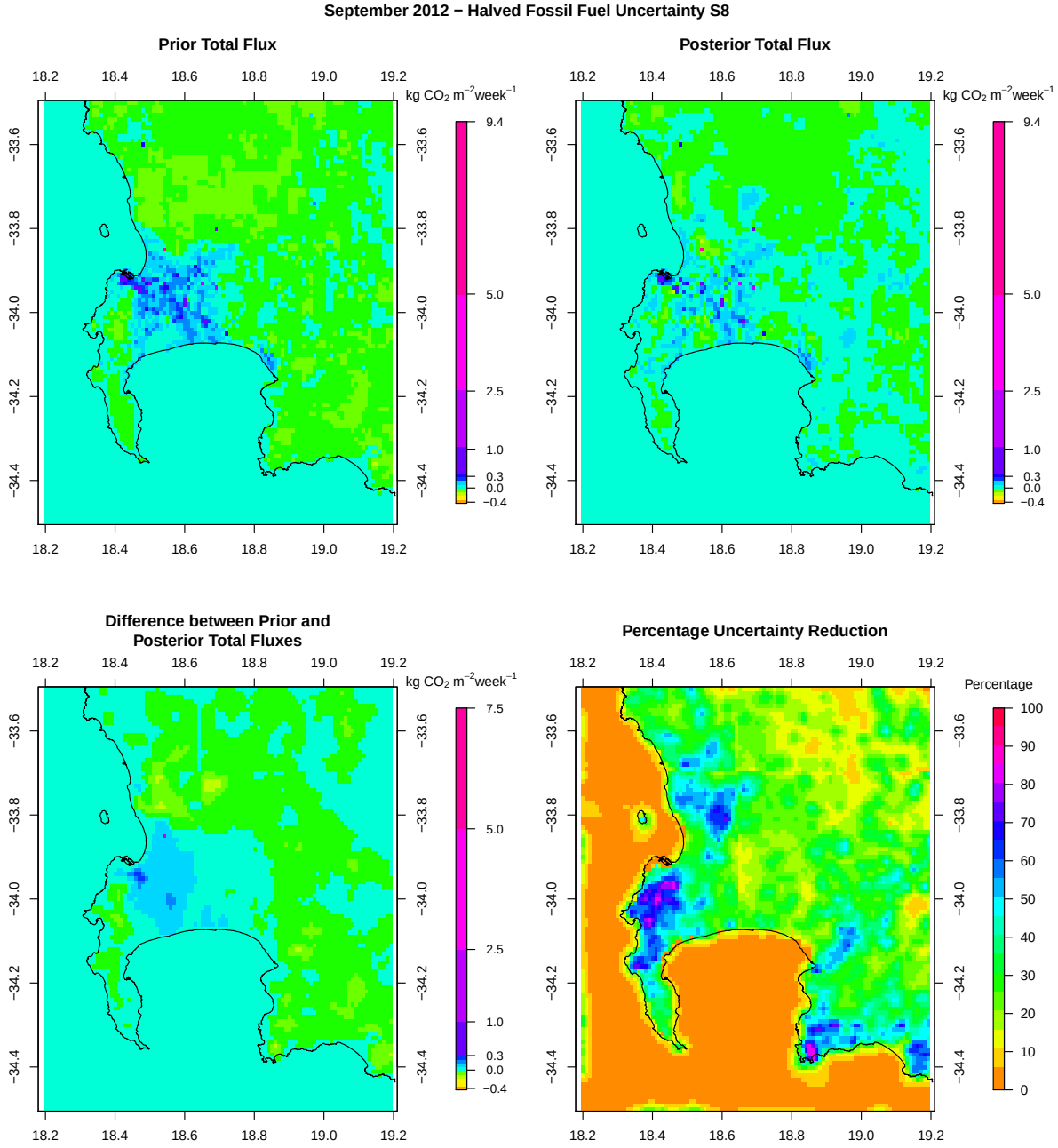

Figure S71. Spatial distribution of the pixel-level prior and posterior CO_2 fluxes of the inversion with halved fossil fuel flux uncertainties S8, the difference between prior and posterior flux estimates, and the uncertainty reduction relative to the prior uncertainty for September 2012.

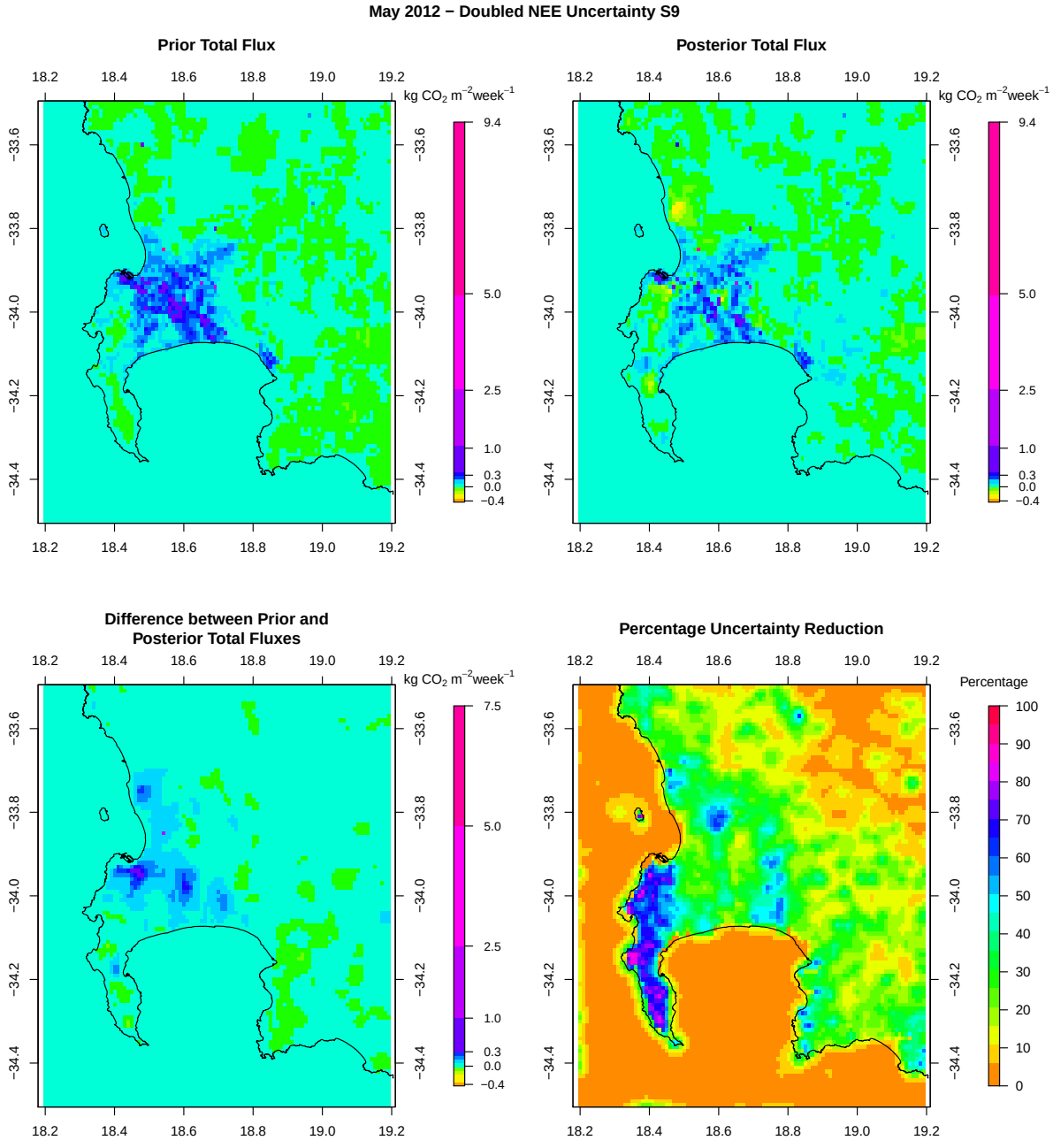

Figure S72. Spatial distribution of the pixel-level prior and posterior CO_2 fluxes of the inversion with doubled NEE flux uncertainties S9, the difference between prior and posterior flux estimates, and the uncertainty reduction relative to the prior uncertainty for May 2012.

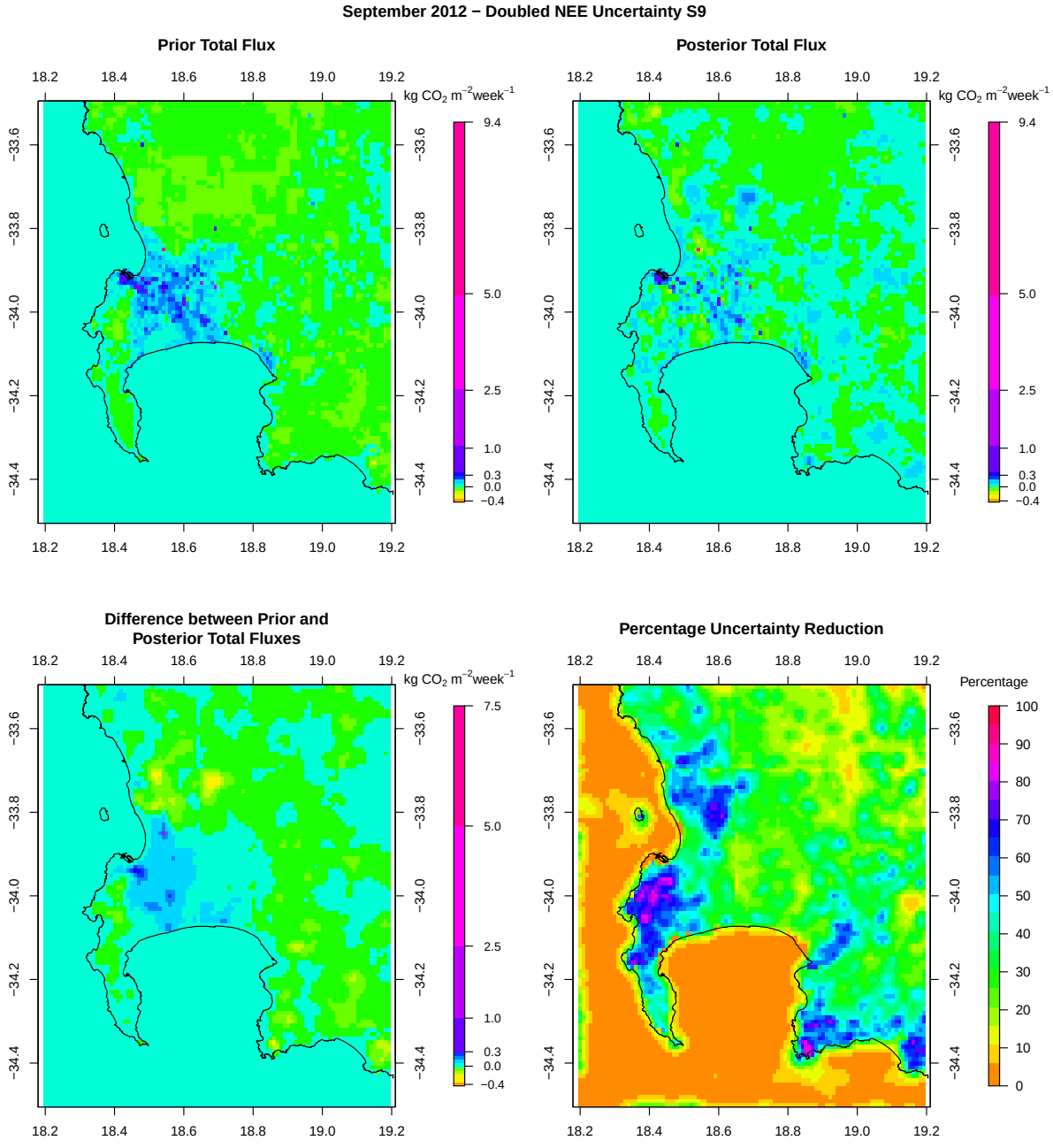

Figure S73. Spatial distribution of the pixel-level prior and posterior CO_2 fluxes of the inversion with doubled NEE flux uncertainties S9, the difference between prior and posterior flux estimates, and the uncertainty reduction relative to the prior uncertainty for September 2012.

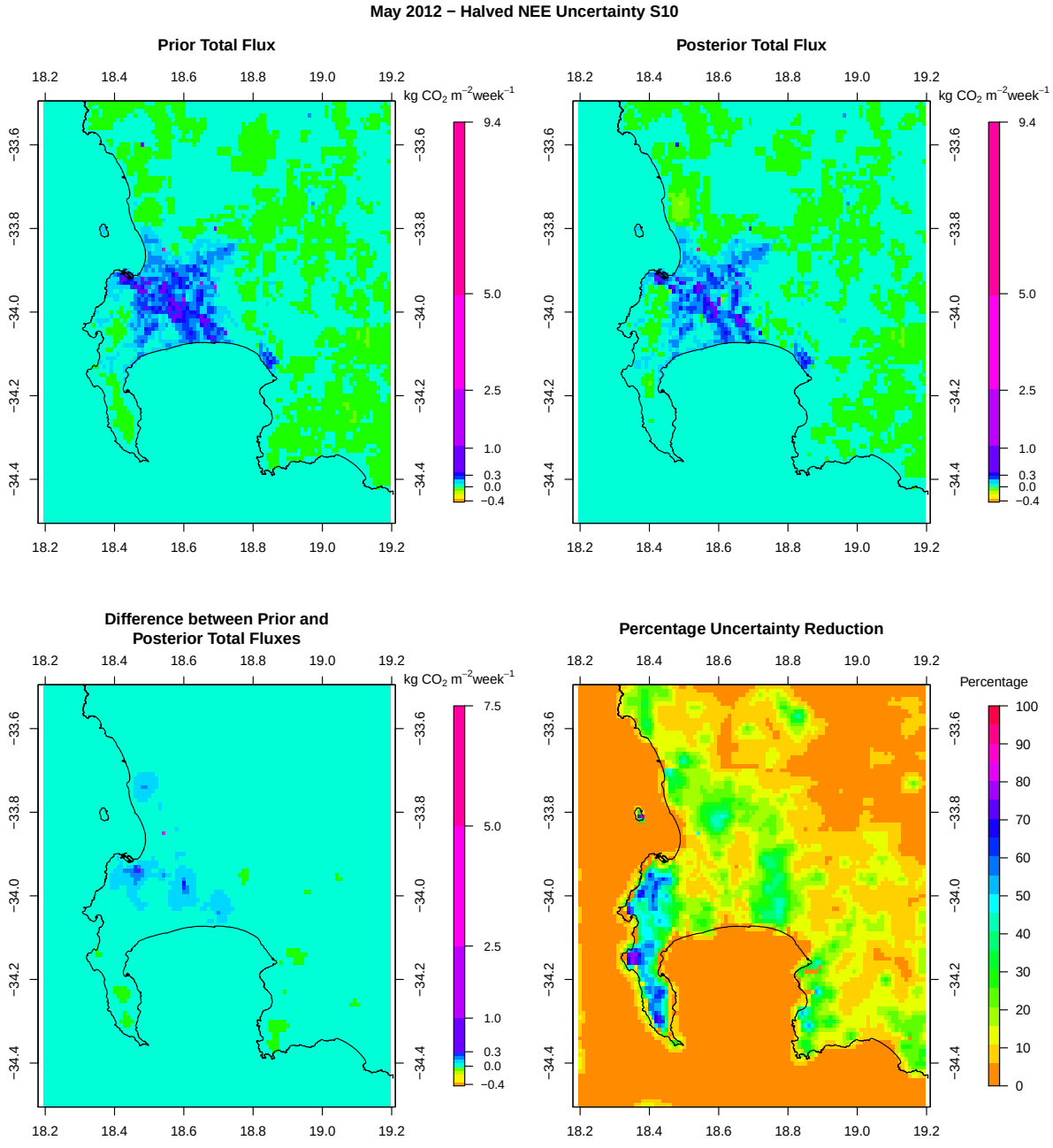

Figure S74. Spatial distribution of the pixel-level prior and posterior CO_2 fluxes of the inversion with halved NEE flux uncertainties S10, the difference between prior and posterior flux estimates, and the uncertainty reduction relative to the prior uncertainty for May 2012.

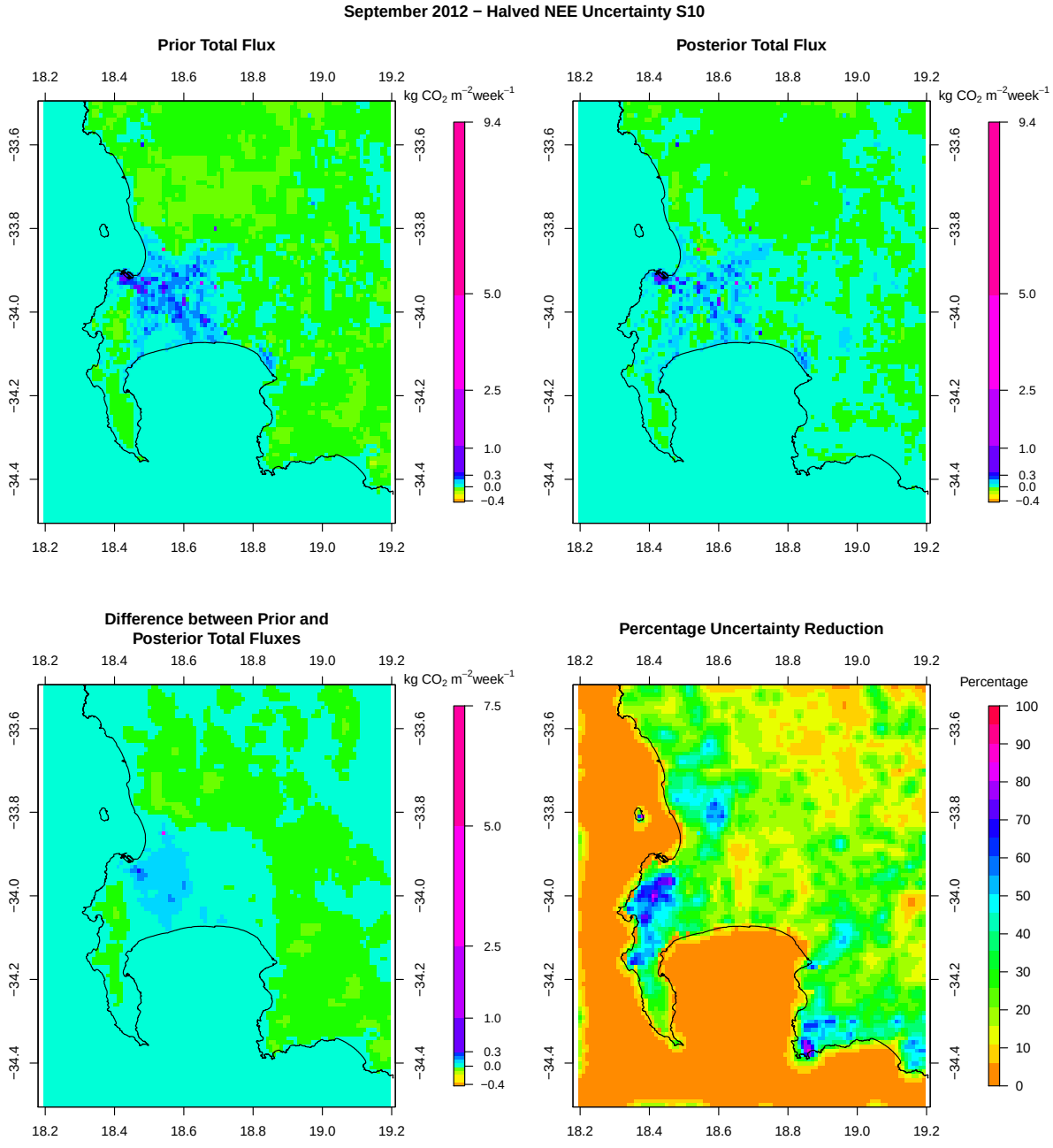

Figure S75. Spatial distribution of the pixel-level prior and posterior CO_2 fluxes of the inversion with halved NEE flux uncertainties S10, the difference between prior and posterior flux estimates, and the uncertainty reduction relative to the prior uncertainty for September 2012.

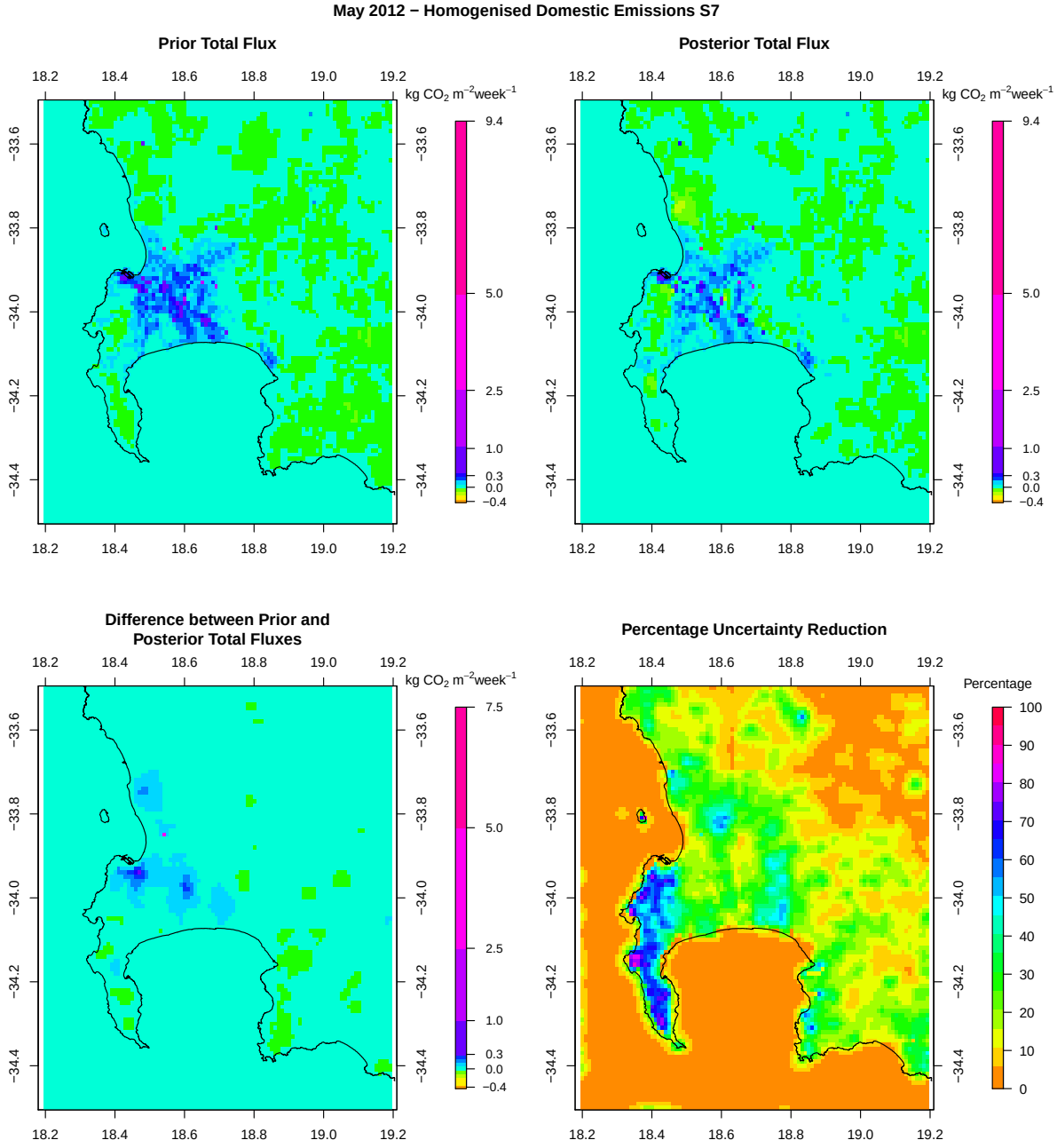

Figure S76. Spatial distribution of the pixel-level prior and posterior CO_2 fluxes of the inversion with temporally homogenised domestic fossil fuel prior fluxes S11, the difference between prior and posterior flux estimates, and the uncertainty reduction relative to the prior uncertainty for May 2012.

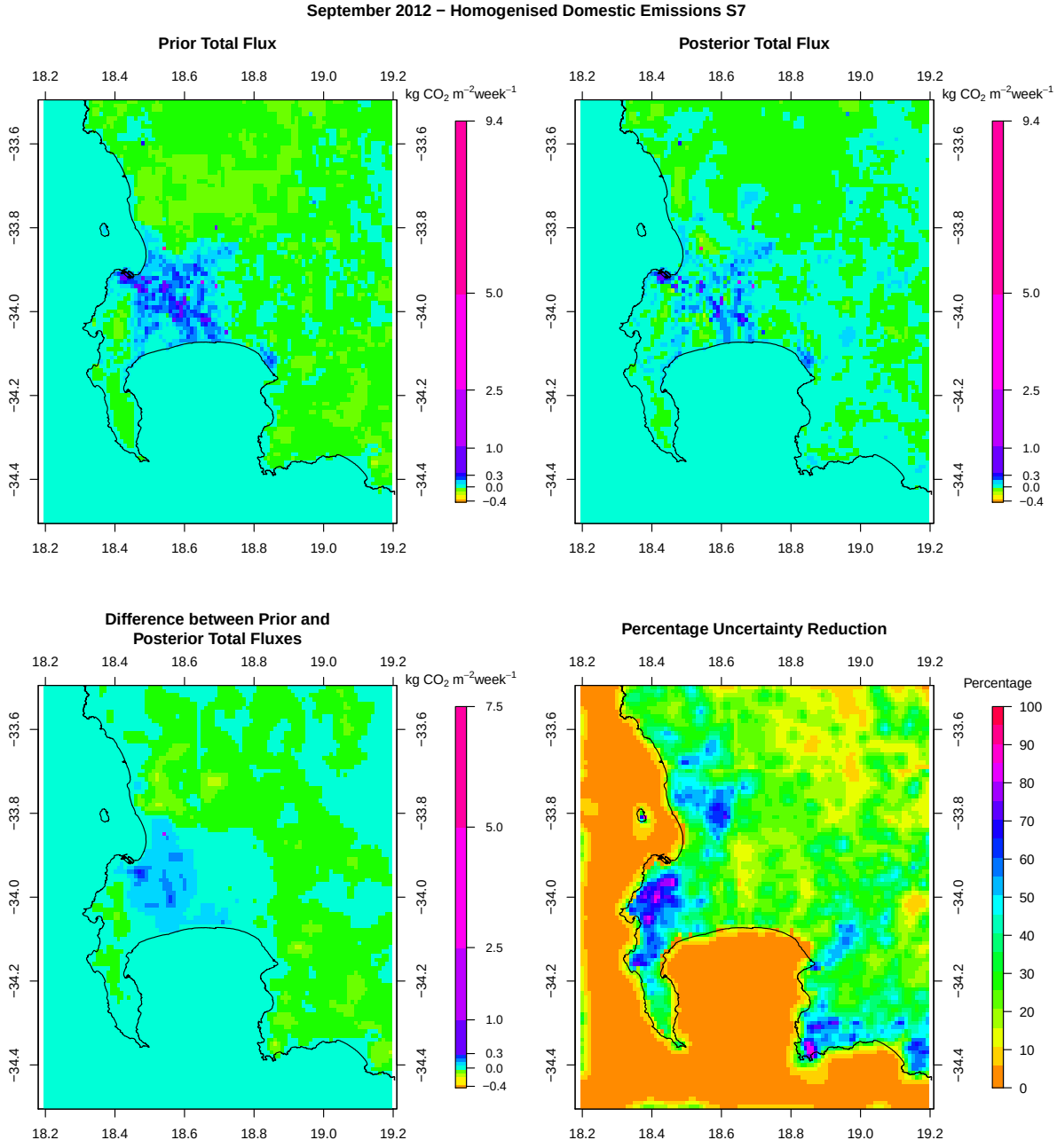

Figure S77. Spatial distribution of the pixel-level prior and posterior CO_2 fluxes of the inversion with temporally homogenised domestic fossil fuel prior fluxes S11, the difference between prior and posterior flux estimates, and the uncertainty reduction relative to the prior uncertainty for September 2012.

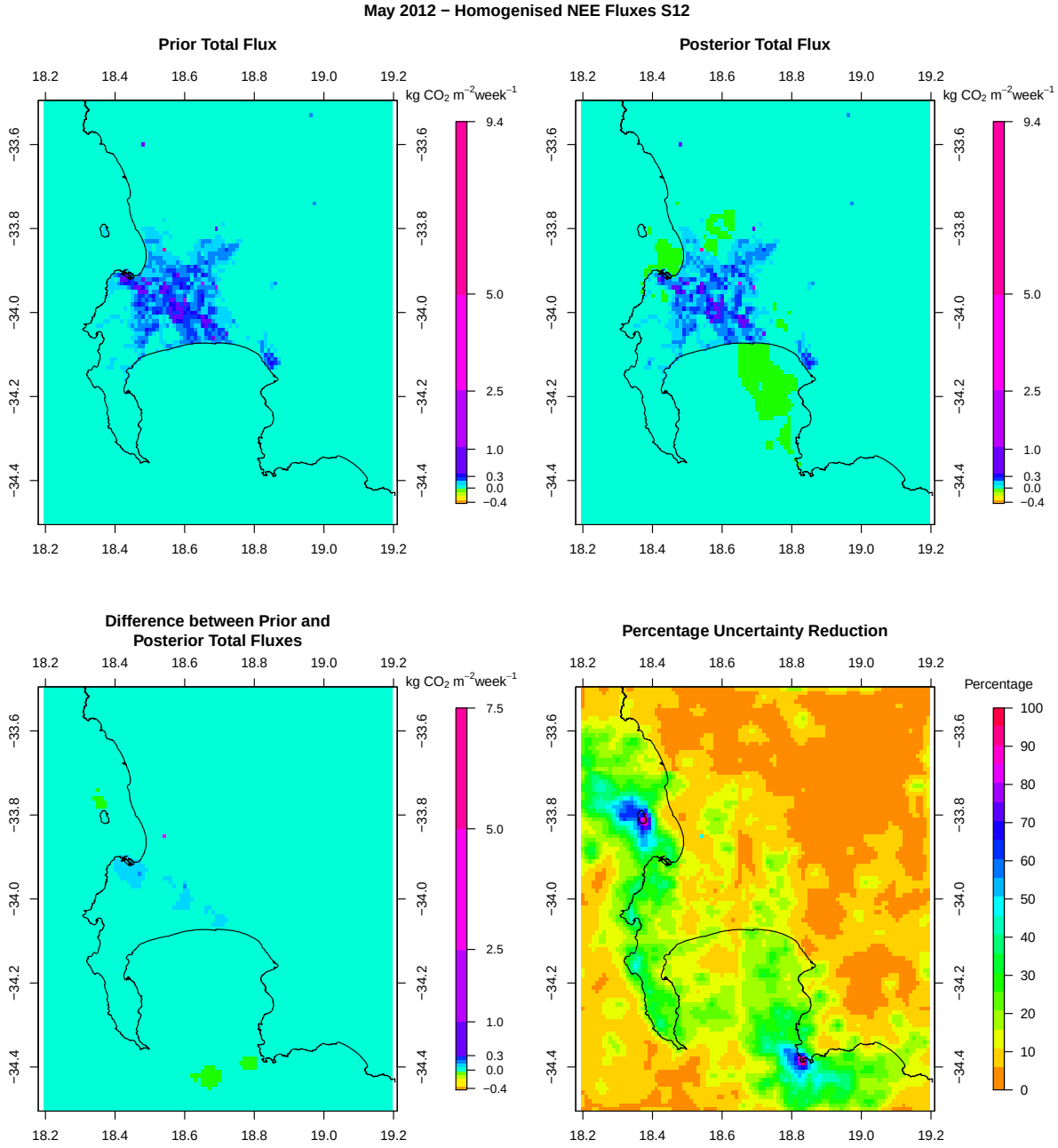

Figure S78. Spatial distribution of the pixel-level prior and posterior CO_2 fluxes of the inversion with spatially homogenised NEE prior fluxes S12, the difference between prior and posterior flux estimates, and the uncertainty reduction relative to the prior uncertainty for May 2012.

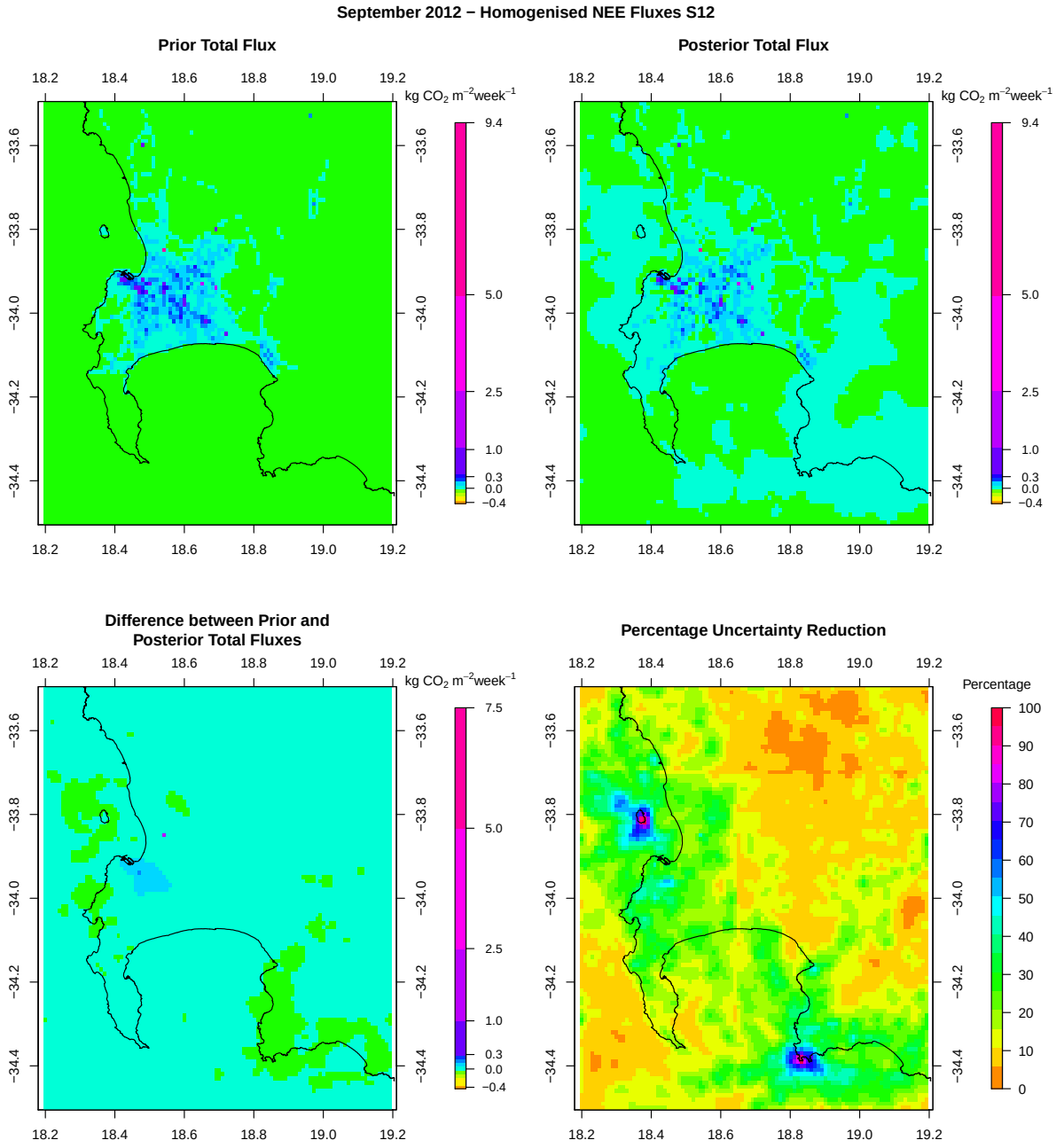

Figure S79. Spatial distribution of the pixel-level prior and posterior CO_2 fluxes of the inversion with spatially homogenised NEE prior fluxes S12, the difference between prior and posterior flux estimates, and the uncertainty reduction relative to the prior uncertainty for September 2012.

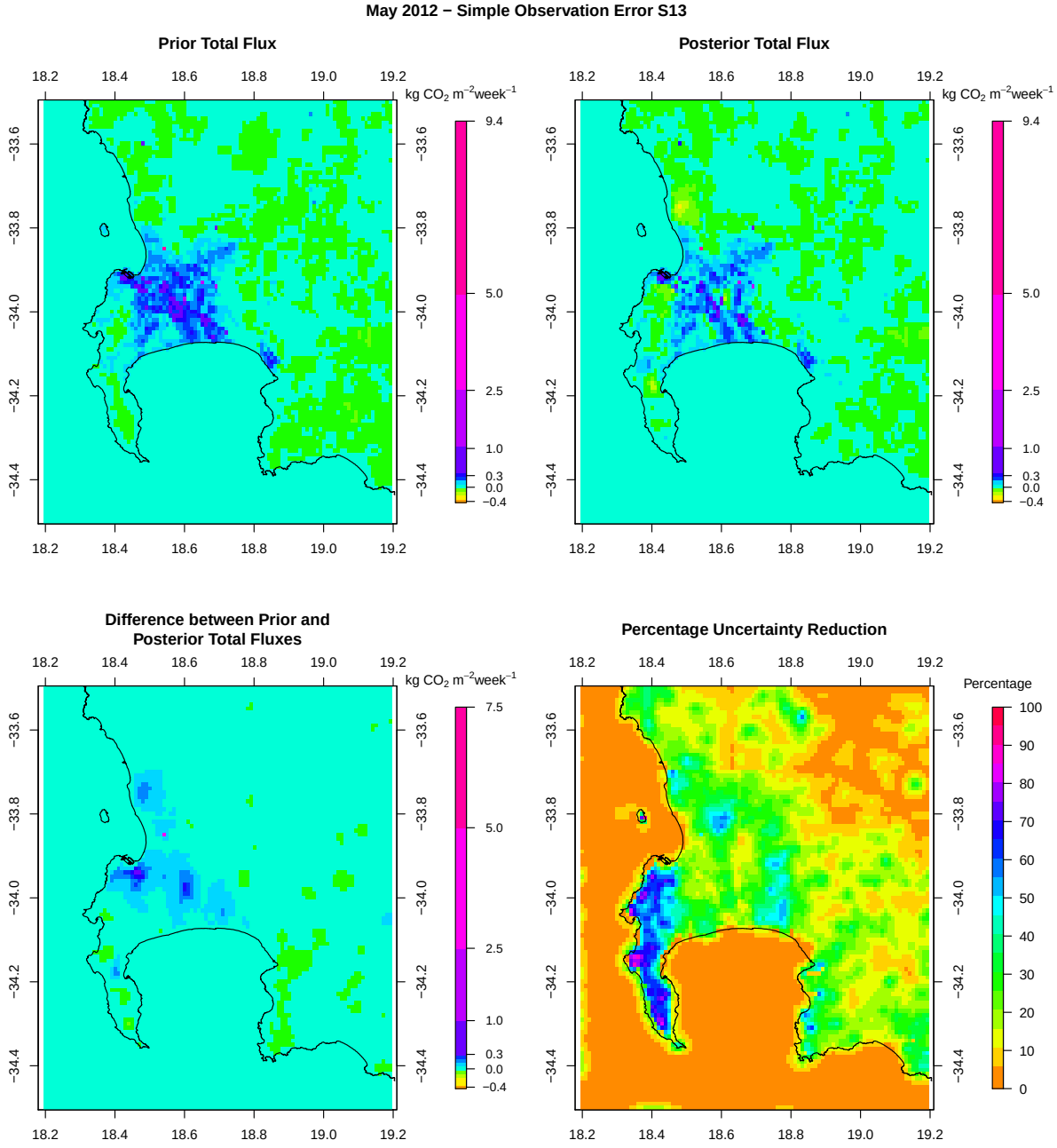

Figure S80. Spatial distribution of the pixel-level prior and posterior CO_2 fluxes of the inversion specifying uncertainties of 2 ppm and 4 ppm for the day and night-time observation errors S13, the difference between prior and posterior flux estimates, and the uncertainty reduction relative to the prior uncertainty for May 2012.

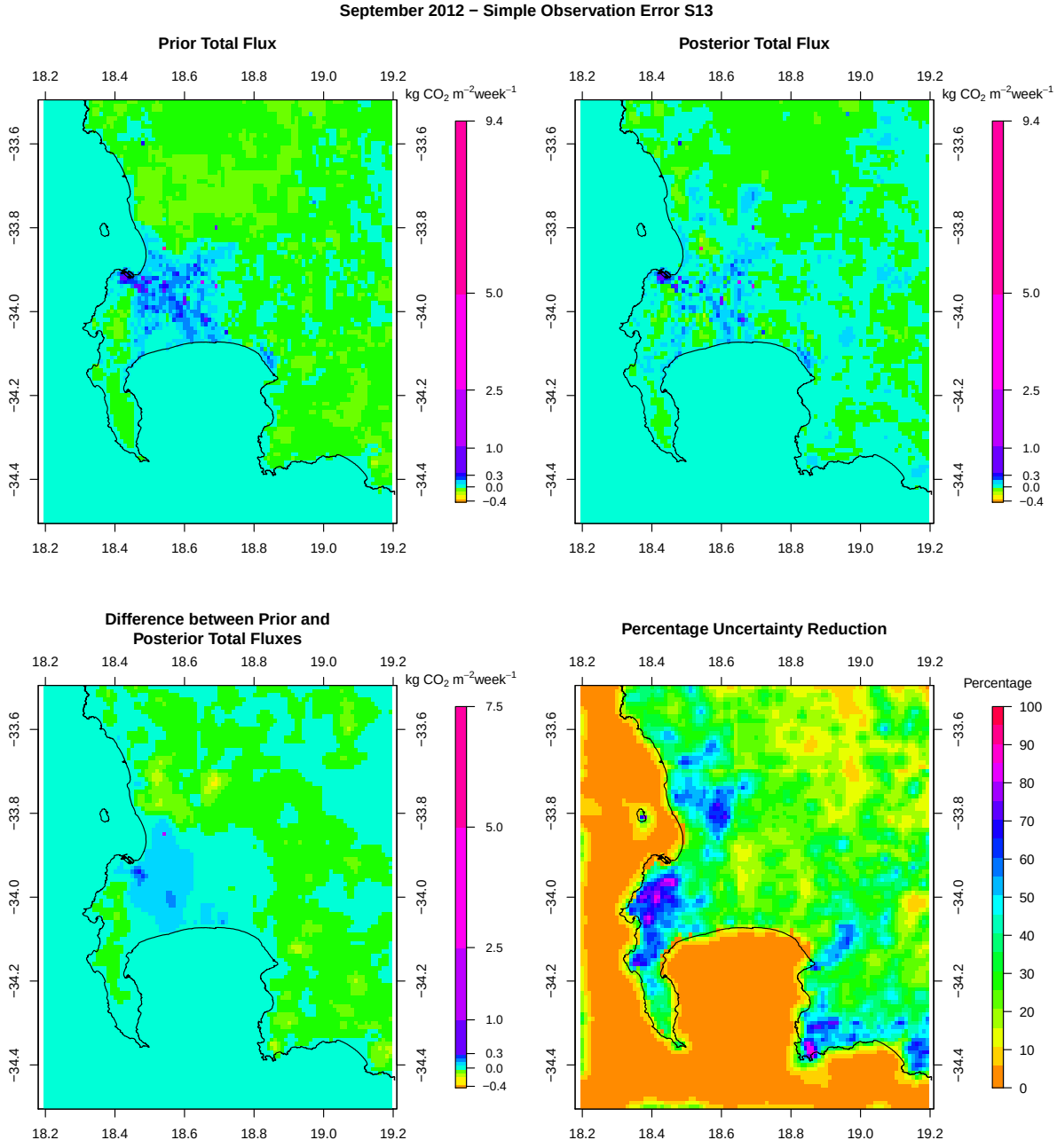

Figure S81. Spatial distribution of the pixel-level prior and posterior CO_2 fluxes of the inversion specifying uncertainties of 2 ppm and 4 ppm for the day and night-time observation errors S13, the difference between prior and posterior flux estimates, and the uncertainty reduction relative to the prior uncertainty for September 2012.

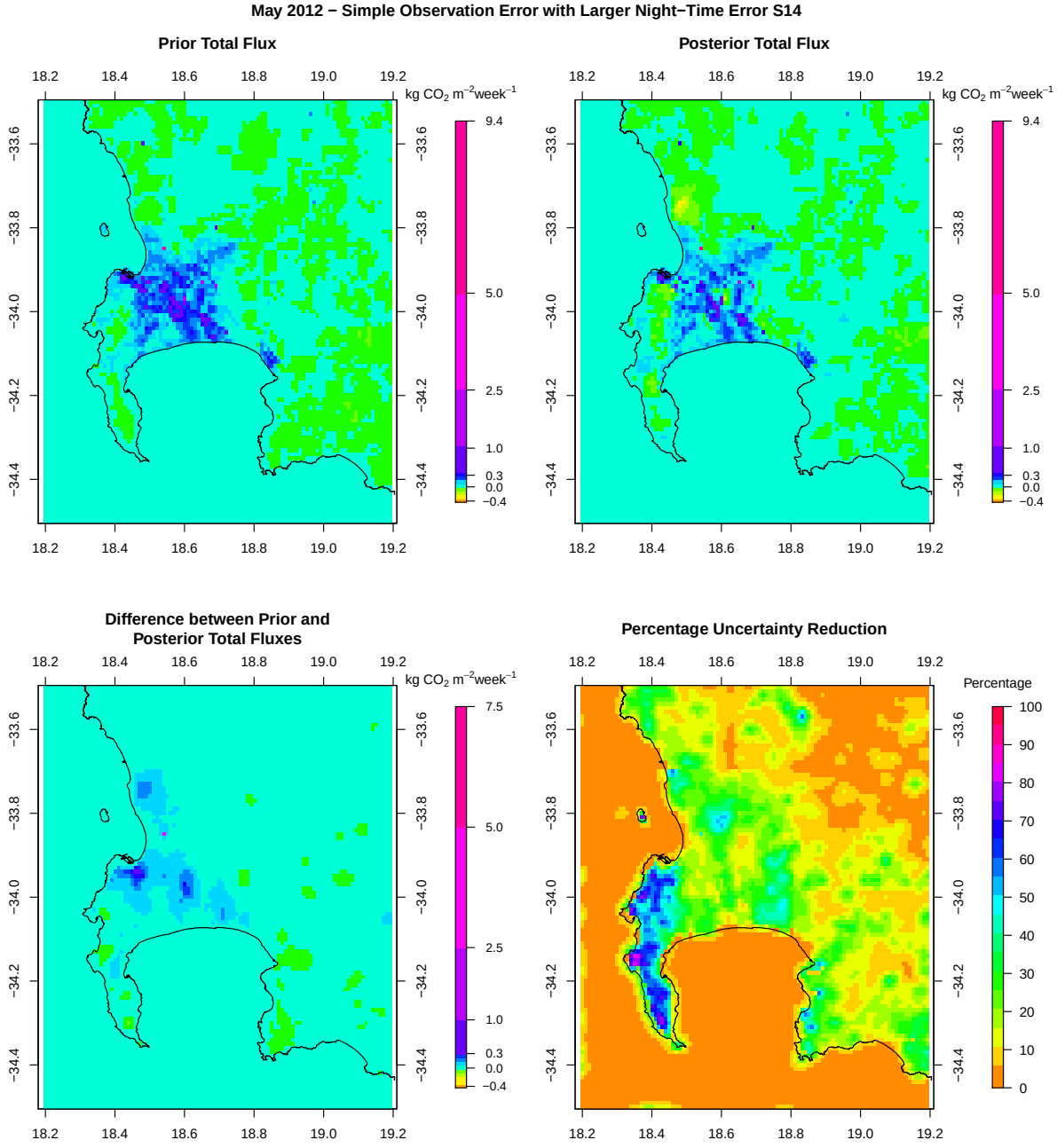

Figure S82. Spatial distribution of the pixel-level prior and posterior CO_2 fluxes of the inversion specifying uncertainties of 2 ppm and 10 ppm for the day and night-time observation errors S14, the difference between prior and posterior flux estimates, and the uncertainty reduction relative to the prior uncertainty for May 2012.

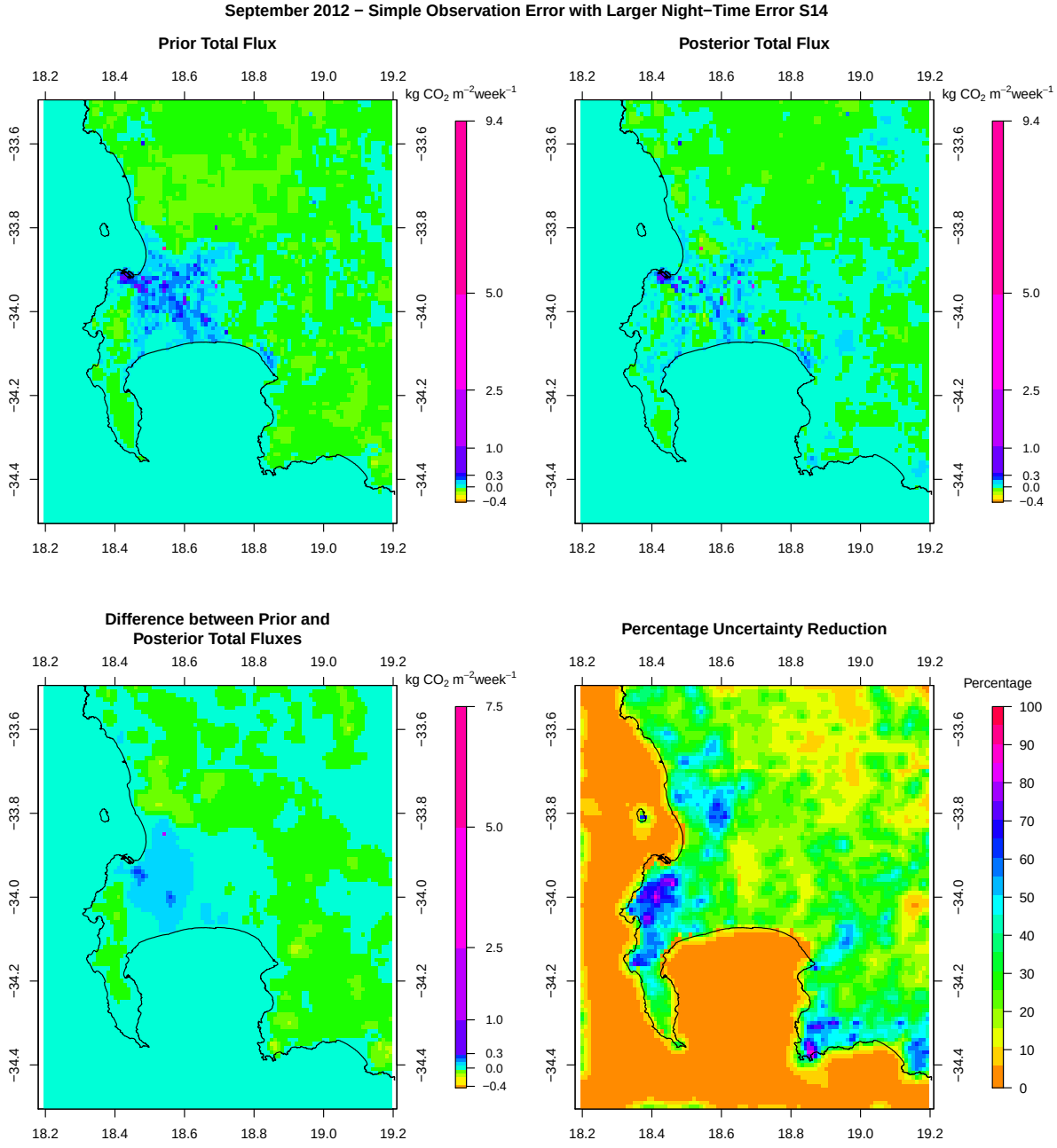

Figure S83. Spatial distribution of the pixel-level prior and posterior CO_2 fluxes of the inversion specifying uncertainties of 2 ppm and 10 ppm for the day and night-time observation errors S14, the difference between prior and posterior flux estimates, and the uncertainty reduction relative to the prior uncertainty for September 2012.

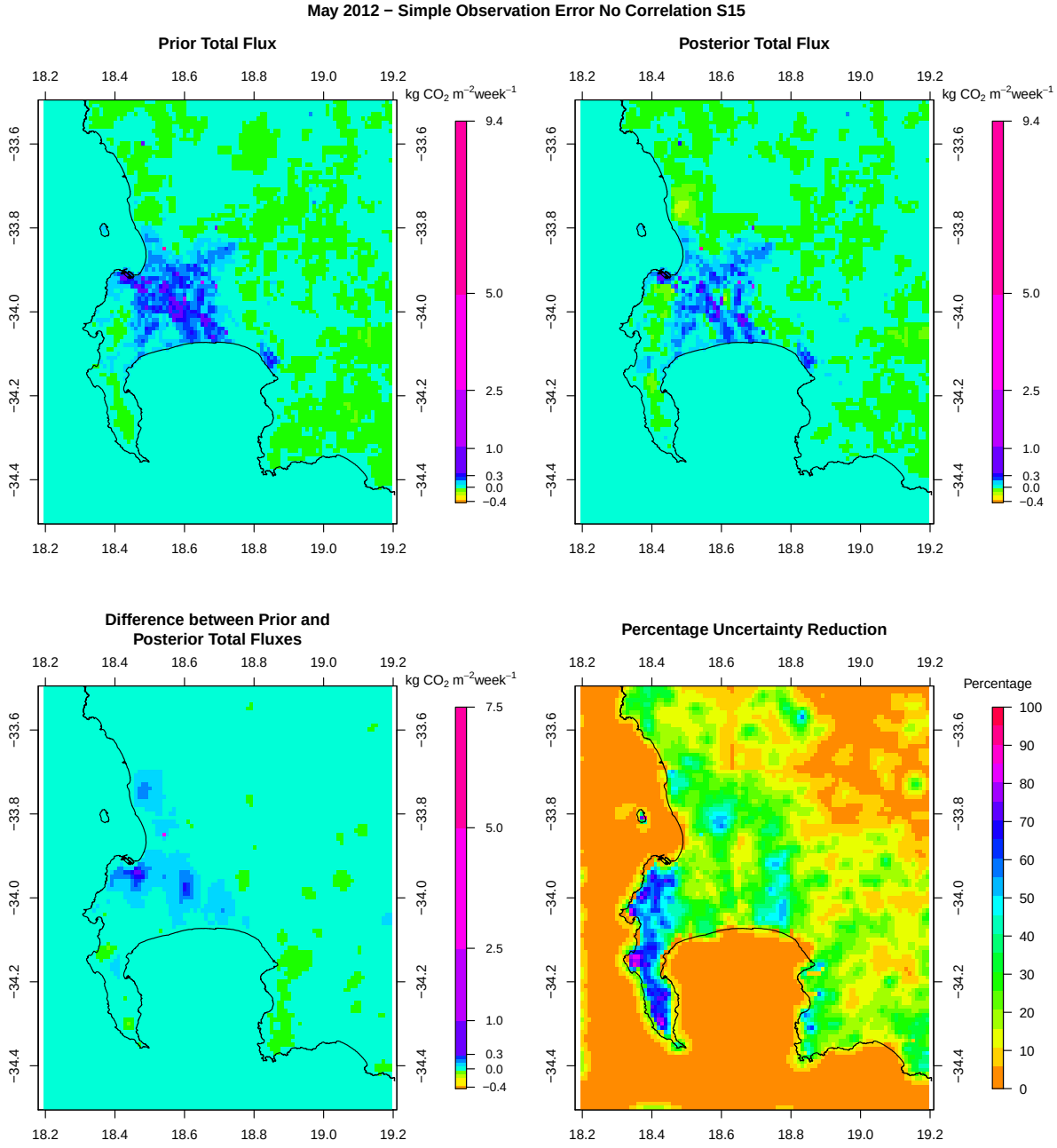

Figure S84. Spatial distribution of the pixel-level prior and posterior CO_2 fluxes of the inversion specifying uncertainties of 2 ppm and 4 ppm for the day and night-time observation errors with no correlation S15, the difference between prior and posterior flux estimates, and the uncertainty reduction relative to the prior uncertainty for May 2012.

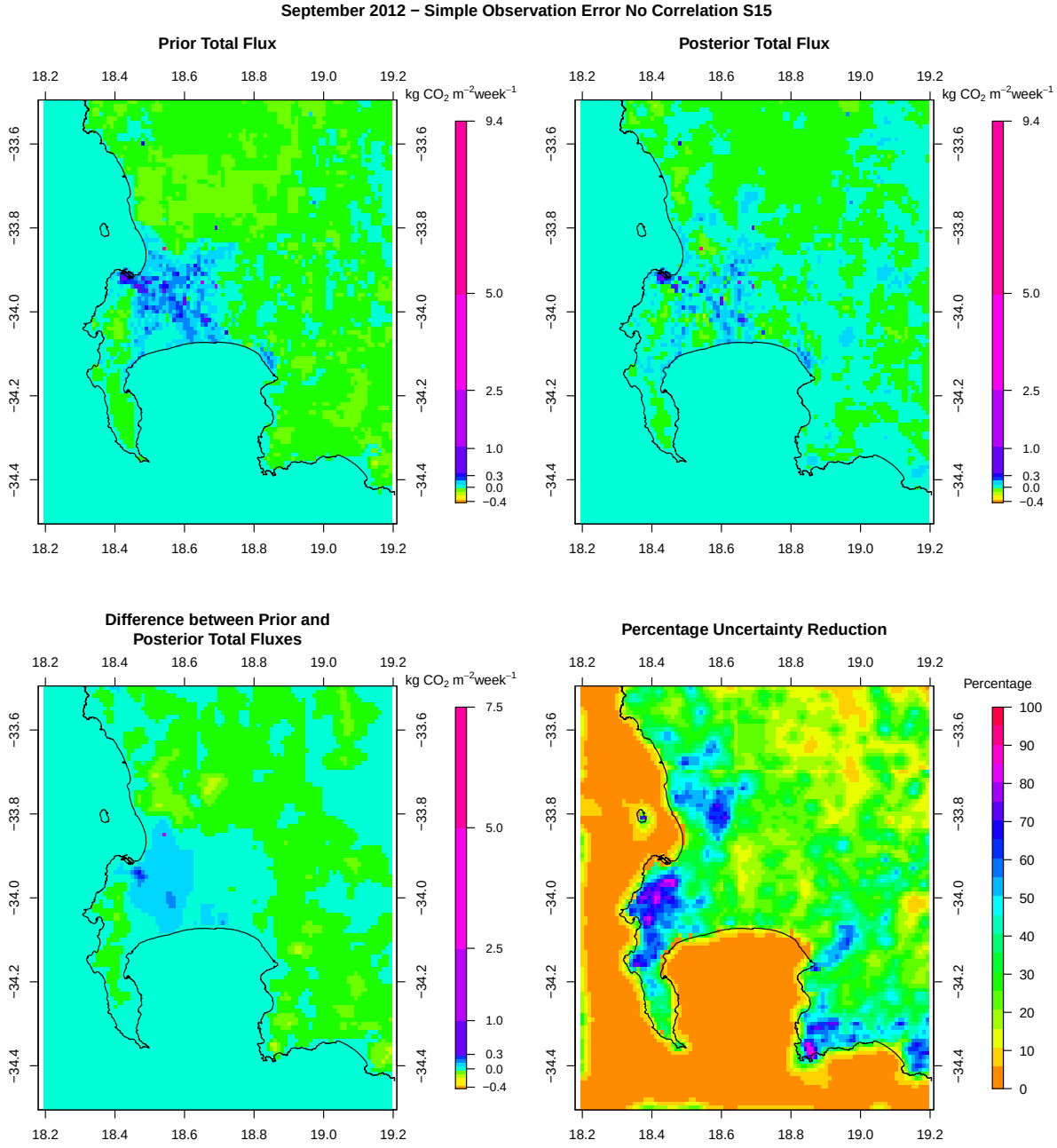

Figure S85. Spatial distribution of the pixel-level prior and posterior CO_2 fluxes of the inversion specifying uncertainties of 2 ppm and 4 ppm for the day and night-time observation errors with no correlation S15, the difference between prior and posterior flux estimates, and the uncertainty reduction relative to the prior uncertainty for September 2012.

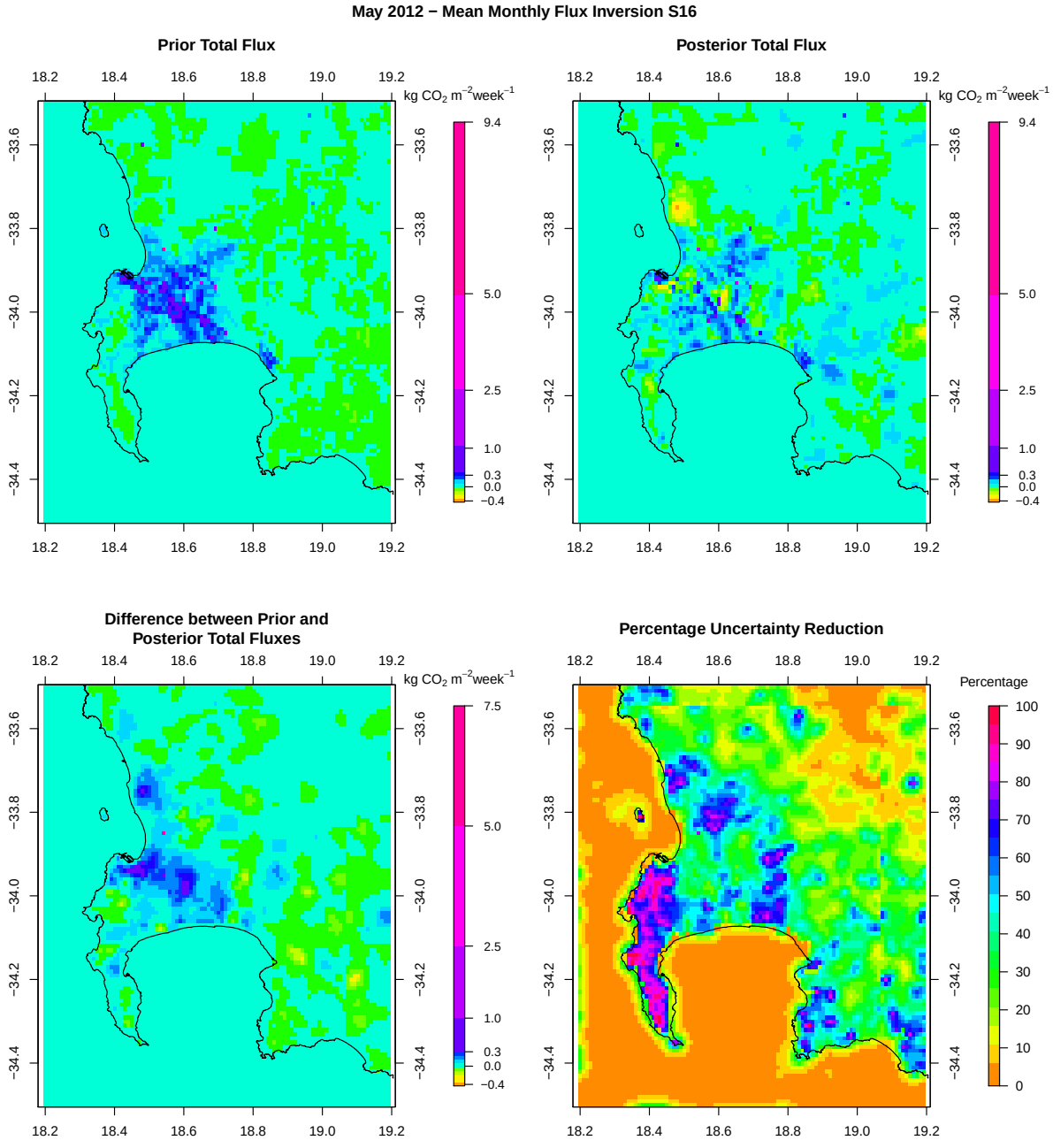

Figure S86. Spatial distribution of the pixel-level prior and posterior CO_2 fluxes of the inversion solving for the mean weekly flux S16, the difference between prior and posterior flux estimates, and the uncertainty reduction relative to the prior uncertainty for May 2012.

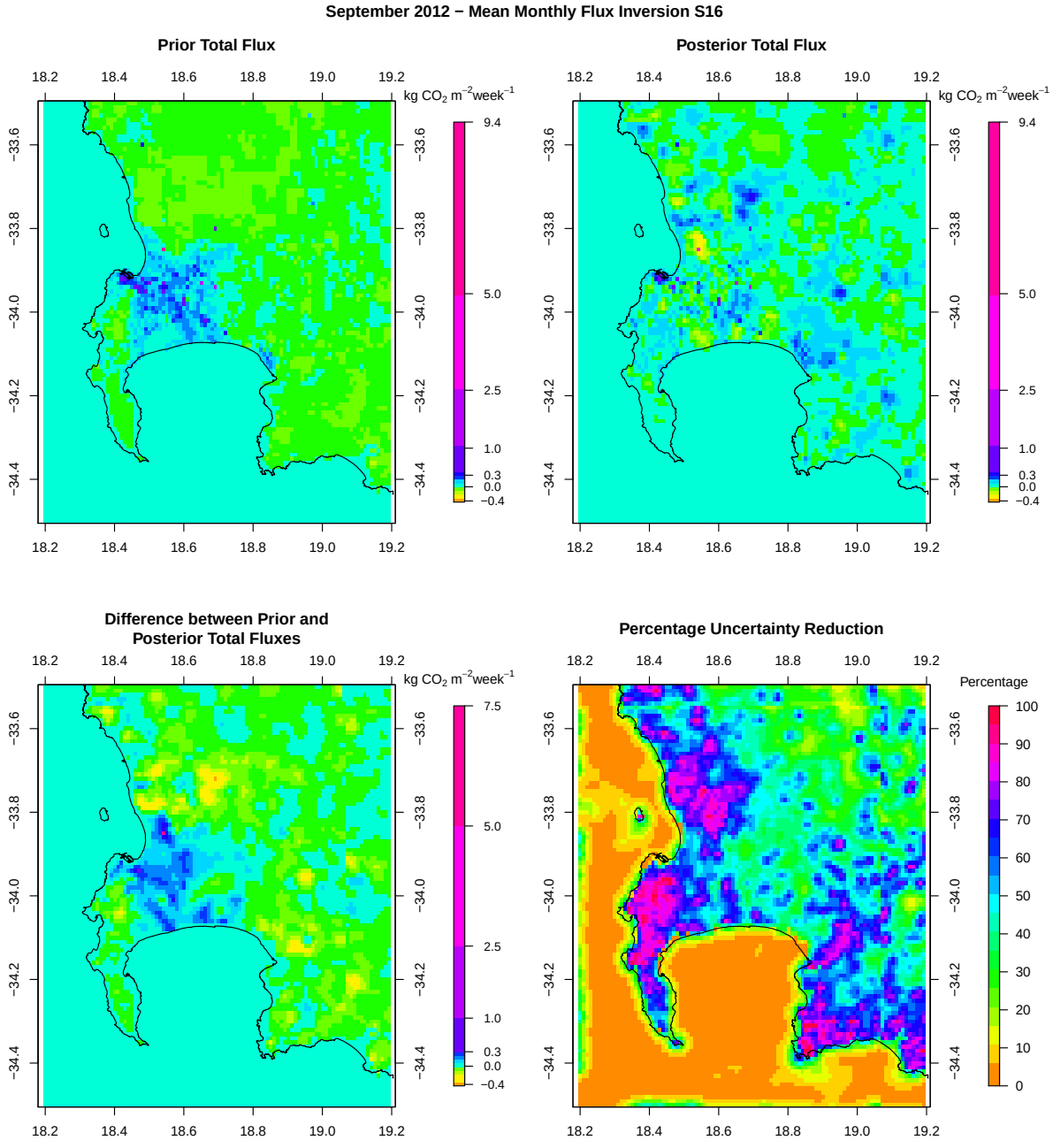

Figure S87. Spatial distribution of the pixel-level prior and posterior CO_2 fluxes of the inversion solving for the mean weekly flux S16, the difference between prior and posterior flux estimates, and the uncertainty reduction relative to the prior uncertainty for September 2012.

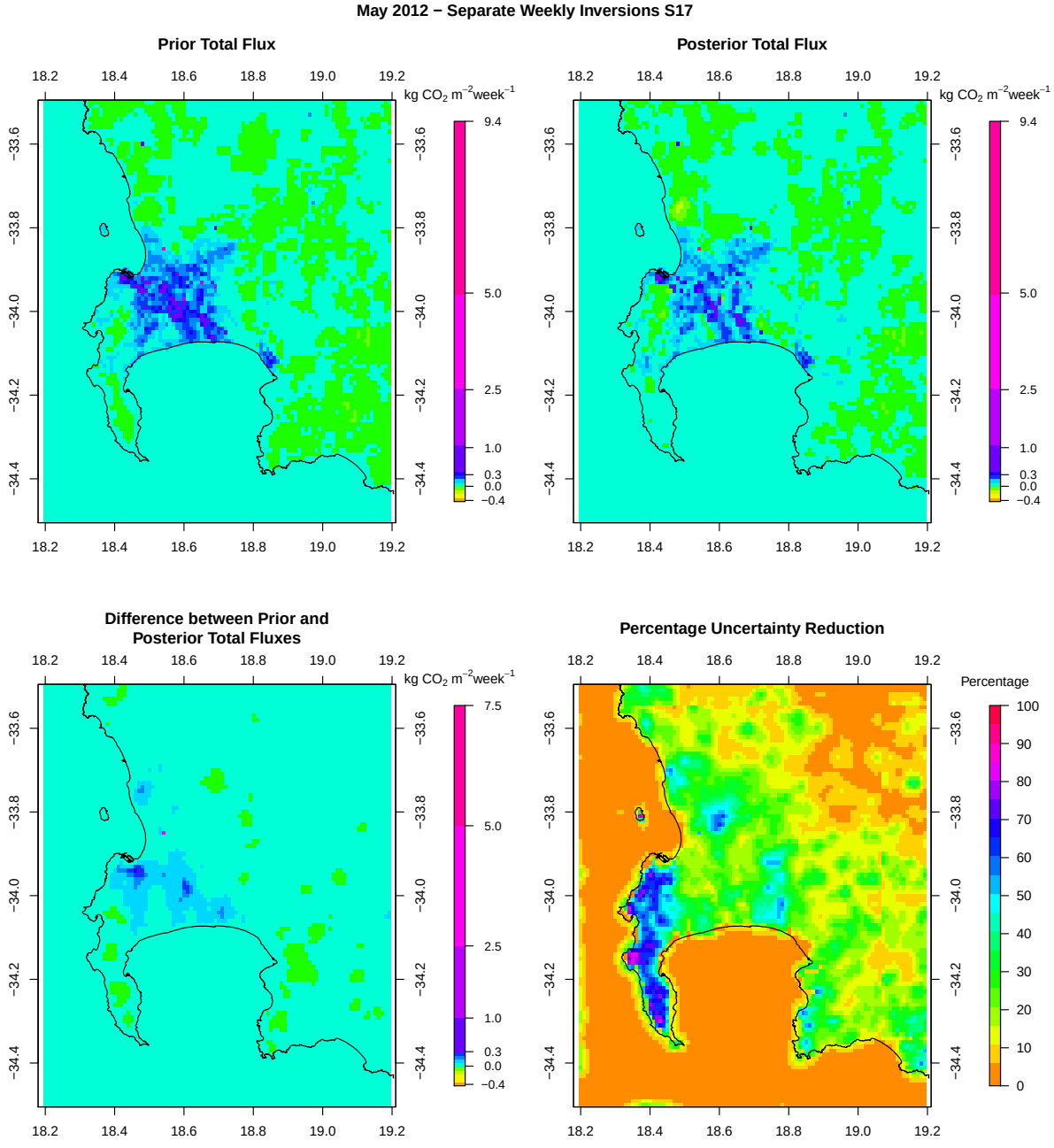

Figure S88. Spatial distribution of the pixel-level prior and posterior CO_2 fluxes of the separate weekly inversions S17, the difference between prior and posterior flux estimates, and the uncertainty reduction relative to the prior uncertainty for May 2012.

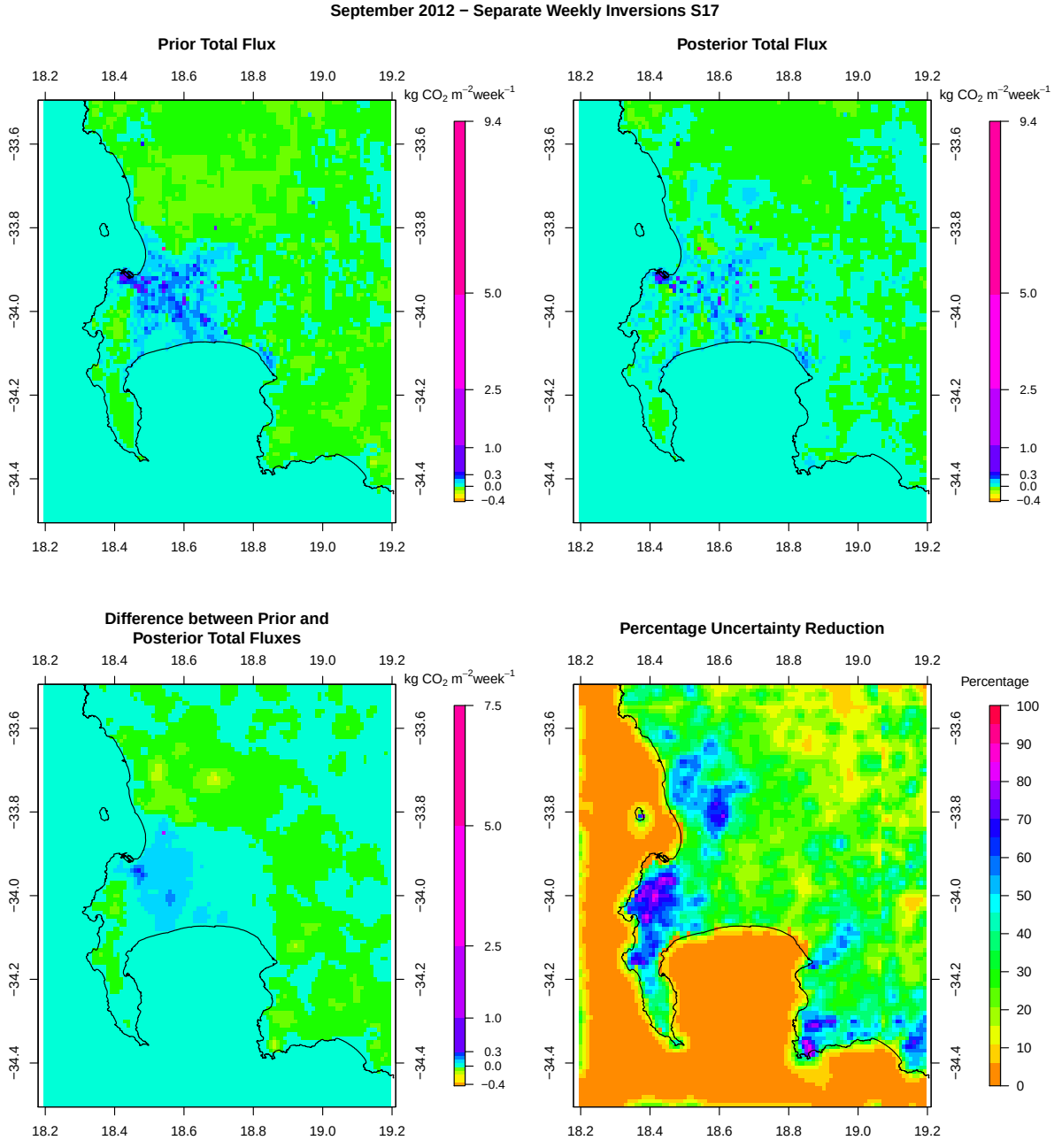

Figure S89. Spatial distribution of the pixel-level prior and posterior CO_2 fluxes of the separate weekly inversions S17, the difference between prior and posterior flux estimates, and the uncertainty reduction relative to the prior uncertainty for September 2012.

1.7 Toy Inversion

Here we consider a toy inversion problem introduced in Nickless et al. (2018). Let us consider an hourly measurement at a single site, with a fossil fuel flux daytime source, a fossil fuel flux night-time source, an NEE flux from the same location, and an NEE flux from a neighbouring pixel. We wish to solve for these four fluxes and the covariance matrix of the uncertainties in these fluxes. Selecting some of the most extreme values for the uncertainties and for the sensitivities for the current inversion framework we could get the following:

$$\mathbf{H} = \quad (0.0, 0.0126, 0.00902, 0.0032); \quad \mathbf{C}_{\boldsymbol{s}_0} = \begin{pmatrix} 233 & 0 & 0 & 0 \\ 0 & 78 & 0 & 0 \\ 0 & 0 & 1578 & 1220 \\ 0 & 0 & 1220 & 1578 \end{pmatrix}; \quad \mathbf{C}_{\boldsymbol{c}} = 4$$

If we solve for the posterior uncertainty covariance matrix for a reference inversion we use:

$$\begin{aligned} \mathbf{C}_{\boldsymbol{s}} &= \left(\mathbf{H}^T \mathbf{C}_{\boldsymbol{c}}^{-1} \mathbf{H} + \mathbf{C}_{\boldsymbol{s}_0}^{-1}\right)^{-1} && (2) \\ &= \mathbf{C}_{\boldsymbol{s}_0} - \mathbf{C}_{\boldsymbol{s}_0} \mathbf{H}^T \left(\mathbf{H} \mathbf{C}_{\boldsymbol{s}_0} \mathbf{H}^T + \mathbf{C}_{\boldsymbol{c}}\right)^{-1} \mathbf{H} \mathbf{C}_{\boldsymbol{s}_0}. && (3) \end{aligned}$$

For this reference problem the solution is:

$$\mathbf{C}_{\boldsymbol{s}} = \begin{pmatrix} 233 & 0 & 0 & 0 \\ 0 & 77.8 & -4.2 & -3.7 \\ 0 & -4.2 & 1500.2 & 1151.1 \\ 0 & -3.7 & 1151.1 & 1517.0 \end{pmatrix}$$

If we multiply the prior uncertainty covariance matrix by a constant, so that all the elements in the covariance matrix are multiplied by this factor, we can show that if there is no measurement error, i.e. $\mathbf{C}_{\boldsymbol{c}} = \mathbf{0}$, the posterior uncertainty covariance matrix can be obtained by multiplying the solution for the posterior uncertainty covariance matrix of the reference problem by this factor.

$$\begin{aligned} \mathbf{C}_{\boldsymbol{s}_{mod}} &= \left(\mathbf{H}^T \mathbf{C}_{\boldsymbol{c}}^{-1} \mathbf{H} + (a\mathbf{C}_{\boldsymbol{s}_0})^{-1}\right)^{-1} && (4) \\ &= a\mathbf{C}_{\boldsymbol{s}_0} - a\mathbf{C}_{\boldsymbol{s}_0} \mathbf{H}^T \left(\mathbf{H} a \mathbf{C}_{\boldsymbol{s}_0} \mathbf{H}^T + \mathbf{C}_{\boldsymbol{c}}\right)^{-1} \mathbf{H} a \mathbf{C}_{\boldsymbol{s}_0} && (5) \\ &= a(\mathbf{C}_{\boldsymbol{s}_0} - \mathbf{C}_{\boldsymbol{s}_0} \mathbf{H}^T \left(\mathbf{H} a \mathbf{C}_{\boldsymbol{s}_0} \mathbf{H}^T + \mathbf{C}_{\boldsymbol{c}}\right)^{-1} \mathbf{H} a \mathbf{C}_{\boldsymbol{s}_0}) && (6) \end{aligned}$$

Now make $\mathbf{C}_{\boldsymbol{c}} = \mathbf{0}$

$$\begin{aligned} \mathbf{C}_{\boldsymbol{s}_{mod}} &= a(\mathbf{C}_{\boldsymbol{s}_0} - \mathbf{C}_{\boldsymbol{s}_0} \mathbf{H}^T \frac{1}{a} \left(\mathbf{H} \mathbf{C}_{\boldsymbol{s}_0} \mathbf{H}^T + \mathbf{C}_{\boldsymbol{c}}\right)^{-1} \mathbf{H} a \mathbf{C}_{\boldsymbol{s}_0}) && (7) \\ &= a(\mathbf{C}_{\boldsymbol{s}_0} - \mathbf{C}_{\boldsymbol{s}_0} \mathbf{H}^T \left(\mathbf{H} \mathbf{C}_{\boldsymbol{s}_0} \mathbf{H}^T + \mathbf{C}_{\boldsymbol{c}}\right)^{-1} \mathbf{H} \mathbf{C}_{\boldsymbol{s}_0}) && (8) \\ &= a\mathbf{C}_{\boldsymbol{s}} && (9) \end{aligned}$$

We can demonstrate this in our toy example. If we make $\mathbf{C}_{\boldsymbol{c}} = 0$ the solution is

$$\mathbf{C}_{\boldsymbol{s}} = \begin{pmatrix} 233 & 0 & 0 & 0 \\ 0 & 73.8 & -78.4 & -69.4 \\ 0 & -78.4 & 131.1 & -60.8 \\ 0 & -69.4 & -60.8 & 444.4 \end{pmatrix}$$

and if we multiply $\mathbf{C}_{\boldsymbol{s}_0}$ by 2 then the solution is

$$\mathbf{C}_{\boldsymbol{s}_{mod}} = \begin{pmatrix} 466 & 0 & 0 & 0 \\ 0 & 147.5 & -156.8 & -138.8 \\ 0 & -156.8 & 262.1 & -121.4 \\ 0 & -138.8 & -121.4 & 888.8 \end{pmatrix}; \quad \mathbf{C}_{\boldsymbol{s}_{mod}} = 2\mathbf{C}_{\boldsymbol{s}}$$

For our original problem where $\mathbf{C}_{\boldsymbol{c}} = 4$, if we multiply $\mathbf{C}_{\boldsymbol{s}_0}$ by 2 the solution is

$$\mathbf{C}_{\boldsymbol{s}_{mod}} = \begin{pmatrix} 466 & 0 & 0 & 0 \\ 0 & 155.1 & -16.0 & -14.2 \\ 0 & -16.0 & 2860.6 & 2178.5 \\ 0 & -14.2 & 2178.5 & 2924.6 \end{pmatrix};$$

Compared to:

$$\mathbf{C}_{\boldsymbol{s}} = \begin{pmatrix} 233 & 0 & 0 & 0 \\ 0 & 77.8 & -4.2 & -3.7 \\ 0 & -4.2 & 1500.2 & 1151.1 \\ 0 & -3.7 & 1151.1 & 1517.0 \end{pmatrix}; 2\mathbf{C}_{\boldsymbol{s}} = \begin{pmatrix} 466 & 0 & 0 & 0 \\ 0 & 155.5 & -8.4 & -7.5 \\ 0 & -8.4 & 3000.4 & 2302.2 \\ 0 & -7.5 & 2302.2 & 3034.1 \end{pmatrix}$$

For those sources where sensitivities were zero, the uncertainty covariance $C_{s_{mod}}$ is equal to exactly $2 \times C_s$. Diagonal elements of $\mathbf{C}_{\boldsymbol{s}_{mod}}$ were approximately equal to the diagonal elements of $2\mathbf{C}_{\boldsymbol{s}}$, but non-zero off-diagonal elements were greater in size than non-zero off-diagonal elements $2\mathbf{C}_{\boldsymbol{s}}$.

References

Nickless, A., Rayner, P. J., Engelbrecht, F., Brunke, E.-G., Erni, B., and Scholes, R. J.: Estimates of CO_2 fluxes over the city of Cape Town, South Africa, through Bayesian inverse modelling, Atmos. Chem. Phys., 18, 4765-4801, doi: 10.5194/acp-18-4765-2018, 2018.

Rodgers, C. D.: Inverse methods for atmospheric sounding : theory and practice, World Scientific Publishing, Singapore, 2000.